



Review

# A Critical Review of Radiolysis Issues in Water-Cooled Fission and Fusion Reactors: Part II, Prediction of Corrosion Damage in Operating Reactors

Digby D. Macdonald<sup>1,\*</sup> and George R. Engelhardt<sup>2</sup>

<sup>1</sup> Department of Nuclear Engineering, University of California at Berkeley, Berkeley, CA 94720, USA

<sup>2</sup> OLI Systems, Inc., 2 Gatehall Drive, Parsippany, NJ 07054, USA

\* Correspondence: macdonald@berkeley.edu

**Abstract:** The radiolysis of water is a significant cause of corrosion damage in the primary heat transport systems (PHTSs) of water-cooled, fission nuclear power reactors (BWRs, PWRs, and CANDUs) and is projected to be a significant factor in the evolution of corrosion damage in future fusion reactors (e.g., the ITER that is currently under development). In Part I of this two-part series, we reviewed the proposed mechanisms for the radiolysis of water and demonstrate that radiolysis leads to the formation of a myriad of oxidizing and reducing species. In this Part II, we review the role that the radiolysis species play in establishing the electrochemical corrosion potential (ECP) and the development of corrosion damage due to intergranular stress corrosion cracking (IGSCC) in reactor PHTSs. We demonstrate, that the radiolytic oxidizing radiolysis products, such as O<sub>2</sub>, H<sub>2</sub>O<sub>2</sub>, HO<sub>2</sub><sup>-</sup>, and OH, when in molar excess over reducing species (H<sub>2</sub>, H, and O<sub>2</sub><sup>2-</sup>), some of which (H<sub>2</sub>) are preferentially stripped from the coolant upon boiling in a BWR PHTS, for example, renders the coolant in many BWRs oxidizing, thereby shifting the ECP in the positive direction to a value that is more positive than the critical potential ( $E_{crit} = -0.23 V_{she}$  at 288 °C) for IGSCC in sensitized austenitic stainless steel (e.g., Type 304 SS). This has led to many IGSCC incidents in operating BWRs over the past five decades that has exacted a great cost on the plant operators and electricity consumers, alike. In the case of PWRs, the primary circuits are pressurized with hydrogen to give a hydrogen concentration of 10 to 50 cm<sup>3</sup>/kgH<sub>2</sub>O (0.89 to 4.46 ppm), such that no sustained boiling occurs, and the hydrogen suppresses the radiolysis of water, thereby inhibiting the formation of oxidizing radiolysis products from water. Thus, the ECP is dominated by the hydrogen electrode reaction (HER), although important deviations from the HER equilibrium potential may occur, particularly at low [H<sub>2</sub>]. In any event, the ECP is displaced to approximately  $-0.85 V_{she}$ , which is below the critical potential for IGSCC in sensitized stainless steels but is also more negative than the critical potential for the hydrogen-induced cracking (HIC) of mill-annealed Alloy 600. This has led to extensive cracking of steam generator tubing and other components (e.g., control rod drive tubes, pressurizer components) in PWRs that has also exacted a high cost on operators and power consumers. Although the ITER has yet to operate, the proposed chemistry protocol for the coolant places it close to a BWR operating on Normal Water Chemistry (NWC) without boiling or, if hydrogen is added to the IBED-PHTS, close to a BWR on Hydrogen Water Chemistry (HWC). In the current ITER technology, the concentration of H<sub>2</sub> in the IBED-PHTS is specified to be 80 ppb, which is the concentration that will be experienced in both the Plasma Flux Area (PFA) and in the Out of Plasma Flux Area (OPFA). That corresponds to 0.90 cc(STP) H<sub>2</sub>/KgH<sub>2</sub>O, compared with 20–50 cc(STP) H<sub>2</sub>/KgH<sub>2</sub>O employed in a PWR primary coolant circuit and 5.5 to 22 cc(STP) H<sub>2</sub>/KgH<sub>2</sub>O in a BWR on hydrogen water chemistry (HWC). We predict that a hydrogen concentration of 80 ppb is sufficient to reduce the ECP in the OPFA to a level ( $-0.324 V_{she}$ ) that is sufficient to suppress the crack growth rate (CGR) below the practical, maximum level of 10<sup>-9</sup> cm/s (0.315 mm/a) at which SCC is considered not to be a problem in a coolant circuit but, in the PFA, the ECP is predicted to be 0.380 V<sub>she</sub>, which gives a calculated standard CGR of 2.7 × 10<sup>-6</sup> cm/s. This is more than three orders in magnitude greater than the desired maximum value of 10<sup>-9</sup> cm/s. We recommend that the HWC issue in ITER be revisited to develop a protocol that is effective in suppressing both the ECP and the CGR in the



**Citation:** Macdonald, D.D.; Engelhardt, G.R. A Critical Review of Radiolysis Issues in Water-Cooled Fission and Fusion Reactors: Part II, Prediction of Corrosion Damage in Operating Reactors. *Corros. Mater. Degrad.* **2022**, *3*, 694–758. <https://doi.org/10.3390/cmd3040038>

Academic Editors: Väino Sammelselg and Bernard Normand

Received: 8 June 2021

Accepted: 23 November 2022

Published: 30 November 2022

**Publisher's Note:** MDPI stays neutral with regard to jurisdictional claims in published maps and institutional affiliations.



**Copyright:** © 2022 by the authors. Licensee MDPI, Basel, Switzerland. This article is an open access article distributed under the terms and conditions of the Creative Commons Attribution (CC BY) license (<https://creativecommons.org/licenses/by/4.0/>).

PFA to levels that permit the operation of the IBED-PHTS in accordance with the experience gained in fission reactor technology.

**Keywords:** nuclear reactors; water-cooled; corrosion potential; crack growth rate; stress corrosion cracking

## 1. Introduction

An important goal of modeling the radiolysis of water in Boiling Water Reactor (BWR), Pressurized Water Reactor (PWR) and the ITER (International Thermonuclear Experimental Reactor) Primary Heat Transport System (PHTS), as described in Part I [1] and by Petrov et al. [2] is to predict the impact of radiolysis on the corrosion of structural materials. The most important parameter in defining the evolution of corrosion damage is the electrochemical corrosion potential (ECP) [1]. Many deleterious corrosion phenomena, including general corrosion (GC), pitting corrosion (PC), stress corrosion cracking (SCC), corrosion fatigue (CF), and hydrogen induced cracking (HIC) occur above (PC, SCC, GC, and CF) or below (HIC) critical potentials ( $E_{crit}$ ) and management of coolant radiolysis and chemistry to ensure a ECP that does not lie within a susceptible region is critical to controlling or avoiding corrosion damage in a reactor PHTS. This is the lesson that has been learned in the fission reactor community over the past five decades and it needs to be critically examined by the fusion community, to avoid repeating the same lessons at great cost to the operators and consumers alike.

In Part I [1] and in [2], it is shown that the absorption of ionizing radiation (neutrons,  $\gamma$ -photons, and  $\alpha$  particles), generates a variety of radiolysis products, including  $e_{aq}^-$ , H, OH,  $H_2O_2$ ,  $HO_2$ ,  $HO_2^-$ ,  $O_2$ ,  $O_2^-$ ,  $O_2^{2-}$ ,  $O^-$ , O,  $H_2$ ,  $OH^-$ ,  $H^+$ , and possibly others. These species are either oxidizing agents (e.g.,  $O_2$ ,  $H_2O_2$ , OH, O,  $O^-$ ) or reducing agents ( $H_2$ , H,  $e_{aq}^-$ ,  $O_2^{2-}$ ,  $O_2^-$ ,  $O_2$ ) some of them being thermodynamically quite powerful, as measured by the standard reduction potential (Table 1 [3]). Included in this table are data for nitrogen species because nitrogen is formed by the  $^{16}O_8(^1n_0, ^1p_1)^{16}N_7$  nuclear reaction and from any  $^{14}N_7$  (as dissolved  $N_2$  gas) that might be present in the system. Couples having very negative  $E^0$  values are strong reducing species while those having very positive values are strong oxidizing species.

**Table 1.** Selected standard redox potentials for selected radicals [3].

Redox Couple	$E^0/V_{she}$	Redox Couple	$E^0/V_{she}$	Redox Couple	$E^0/V_{she}$
$e_{aq}^-$	-2.87	OH/ $H_2O$	2.72	$H_2O_2/H_2O$	1.77
H/ $H^+$	-2.31	$H_2/H^+$	0	$O^-/H_2O$	1.77
H/ $H^-$	0.05	$O_2/H_2O_2$	1.23	$O_2/O_2^-$	-0.16
( $O_2, H^+$ )/ $HO_2$	0.12	$O_3/O_3^-$	0.83	$O_2^+/O_2$	3.2
$NH_3^+/NH_3$	2.13	$NH_2/NH_2^-$	0.7	$NH_2OH^+/NH_2OH$	$\leq 1.26$
$NO^+/NO$	1.21	$NO_2/NO_2^-$	1.04	$NO_2^+/NO_2$	1.51
$NO_3^-/NO_3^{2-}$	$< -0.40$	$NO_3/NO_3^-$	2.5	$N_2H_4^+/N_2H_4$	0.01
$N_3/N_3^-$	1.33				

Figure 1 shows a collection of experimental corrosion potential data for stainless steels measured at high temperatures, corresponding roughly to PWR core conditions at the upper temperature extreme. These data illustrate the strong effect that as little as 20 ppb of oxygen contamination in the feedwater can have on the ECP. The figure also shows that with no oxygen present in the hydrogenated feedwater, the measured ECP is more negative than  $-800 \text{ mV}_{she}$  at the highest temperature, depending on the hydrogen concentration, which is slightly more negative than the hydrogen equilibrium electrode potential. This is so, because the ECP is a mixed potential from a corrosion process comprising a partial anodic process (PAP) and a partial cathodic process (PCP, the HER), with the equilibrium potential for the PAP being more negative than the PCP (HER) equilibrium potential. The mixed potential falls between the equilibrium potentials for the two partial processes but is

closest to the equilibrium potential for the partial process that has the greatest exchange current density (in this case, the HER). Accordingly, in a PWR PHTS, the ECP closely follows the HER equilibrium potential, provided that  $[H_2]$  is sufficiently high.

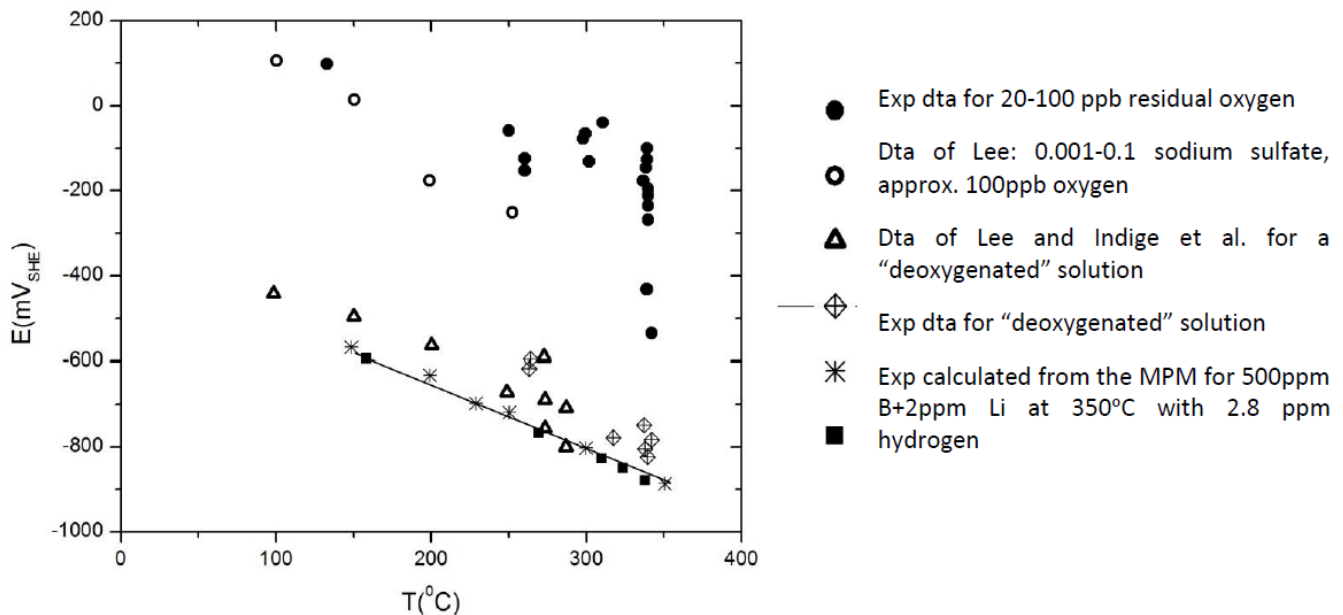


**Figure 1.** Comparison of calculated electrochemical potentials for Type 304 and 316 SS with experimental data obtained in hydrogenated solutions and deoxygenated solutions [4].

Thus, we can expect that, during normal operation of a reactor with HWC at sufficiently high  $[H_2]$ , the ECP in the PHTS will closely follow that of the hydrogen electrode, if radiolysis is completely suppressed. This condition is achieved in the primary circuit of a PWR by operating with  $[H_2] > 25 \text{ cc(STP)}H_2/\text{kg}H_2O$  (2.23 ppm) but is not achieved in a BWR operating under a normal HWC regime ( $[H_2]$  of  $< 1.2$  ppm). Part of the problem in BWRs is that boiling in the core strips hydrogen from the coolant, so that much of the added hydrogen is lost to the steam phase and is not present in the liquid water phase to impact the ECP. In the case of the ITER, which is expected to have a water chemistry not unlike that of a BWR but without boiling, it is specified that 80 ppb [ $0.89 \text{ cc(STP)}H_2/\text{Kg}H_2O$ ] of hydrogen will be added to the PHTS feedwater, which may be compared with about 0.5 ppm [ $5.5 \text{ cc(STP)}H_2/\text{Kg}H_2O$ ] to 2 ppm [ $22.2 \text{ cc(STP)}H_2/\text{Kg}H_2O$ ] employed in BWRs operating under hydrogen water chemistry (HWC), with the upper end of this range corresponding to severe HWC conditions. The impact that these hydrogen levels have on the electrochemical and corrosion properties of water-cooled reactors, including ITER, is discussed in detail later in this paper but the above establishes the relative hydrogen concentrations employed in the three reactor technologies (PWRs, BWRs, and ITER) of interest. If the hydrogen concentration is lowered, particularly during the irradiation the suppression of radiolysis is incomplete, the ECP in the radiation zone will rise (i.e., become more positive) due to the generation of small amounts of oxidizing species, such as  $O_2$  and  $H_2O_2$ . The question, then, is how positive is the ECP likely to become compared with  $E_{crit}$  for various forms of localized corrosion damage [note that both  $E_{crit}$  and ECP are also (different) functions of temperature] recognizing also that the rate of propagation of various forms of localized corrosion (PC, SCC, IGSCC, CF) vary with  $\exp(ECP - E_{crit})$ , so that the rate is very sensitive to the over potential of  $ECP - E_{crit}$ .

Oxygen and hydrogen peroxide generally have very corrosive effects on a reactor coolant system because they shift the ECP in the positive direction, thereby increasing the driving force for general and localized corrosion processes and in many cases making localized corrosion processes possible by shifting the potential above a critical value,  $E_{crit}$ . Thus, if the ECP is shifted above the critical pitting potential ( $V_c$ ), pitting will occur, and

the resulting pits may act as stress risers for the nucleation of SCC and CF. For this reason,  $V_c$  is often taken as  $E_{crit}$  for IGSCC, as discussed below. The critical pitting potential is a sensitive function of chloride concentration, temperature, and pH, such that increasing  $[Cl^-]$  and temperature displace  $V_c$  in the negative direction while increasing pH displaces  $V_c$  in the positive direction. It is also well known from studies on intergranular stress corrosion cracking (IGSCC) in sensitized Type 304 SS in BWR primary coolant circuits, that cracks will propagate only if the ECP exceeds a critical value ( $E_{IGSCC}$ ) that has been set by the US Nuclear Regulatory Commission (NRC) to be  $-0.23 V_{she}$  at 288 °C, as discussed later in this review. However, the critical potential shifts in the positive direction with decreasing temperature but so does the ECP, but at a different rate. While this may seem to be advantageous for the ITER operating at  $T < 150$  °C, it is the relative value of the ECP and  $E_{crit}$  that is important, and this relationship has yet to be determined for the ITER. However, if the potential is displaced too far in the negative direction, HIC may occur in some nickel-based alloys (e.g., Alloy 600 [5]) and in some stainless steels (e.g., sensitized Type 304 SS in acidic solutions [6]), as noted above. The important point is that these potentially catastrophic failure processes may be avoided by the careful control of the ECP, which is an important lesson learned in the fission reactor community that must be heeded by the fusion reactor community. Thus, experiences with the impact of radiolysis on the electrochemical and corrosion behavior in water-cooled fission reactors, as discussed briefly above, provide important lessons with respect to the operation of the coolant system proposed for ITER. These issues are discussed in greater length later in this review.

A simulation of the radiolysis of PWR coolant (1500 ppm B as  $H_3BO_3$  + 1.5 ppm Li as LiOH, + 25 cc/kg $H_2O$ ) is shown in Figure 2 [7]. The simulation predicts that the system comes to a steady state within about 1 ms after initiation of irradiation with neutrons and  $\gamma$ -photons. The reader will note that the most dominant species in the system is  $H_2$  that was added to the coolant (although a small fraction is generated by radiolysis), followed by  $e_{aq}^-$ , OH, and H. As we show later, only the species of highest concentration determine the ECP; these being  $H_2$  and possibly  $e_{aq}^-$  and OH, even though the concentrations of the latter two are much lower than that of  $H_2$  by factors of about 200 and 1000, respectively. However, as shown in Figure 1, even small concentrations of oxidizing species can have a significant impact on the potential, so that this “dominant species” rule must be applied with some caution.

Accordingly, when the ECP is calculated around the primary reactor coolant loop of a PWR, it is expected that the ECP will be displaced towards larger (i.e., more positive) values when the feedwater is contaminated with oxidizing species, such as the radiolysis products  $O_2$ ,  $H_2O_2$ , OH, and  $HO_2$  (cf, Figure 1). However, as noted above, the Mixed Potential Model (MPM) predicts that the contribution that any given species makes to establishing the ECP is roughly proportional to its concentration (see later for a discussion of this topic). Upon this basis, the most important species are  $O_2$ ,  $H_2O_2$ , and  $H_2$  in the case of a BWR but are  $H_2$ ,  $e^-$ , H,  $H_2O_2$ , and OH, in that decreasing order, in the case of a PWR. Furthermore, because H and  $e_{aq}^-$  are overwhelmed by molecular hydrogen at the concentration typically present in a PWR primary coolant, as shown in Figure 2, they, too, may be ignored to a first approximation, or more appropriately combined with  $H_2$  to form a new “hydrogen species” whose concentration is  $[H_2^*] = [H_2] + 0.5[H] + 0.5[e_{aq}^-]$ , as noted in Part I [1]. Likewise, a new hydrogen peroxide species may be defined as  $[H_2O_2^*] = [H_2O_2] + 0.5[OH]$  and a new oxygen concentration as  $[O_2^*] = [O_2] + 0.5[O]$ . These redefined concentrations result in better estimates of the ECP and crack growth rate (CGR). Thus, it was learned many decades ago in the field of fission reactor technology that, while the formation of  $O_2$  and  $H_2O_2$  could be effectively suppressed by the addition of hydrogen to the primary coolant circuit of a PWR, it is also necessary, from an electrochemical viewpoint, that the other radiolysis products be incorporated into the MPM as indicated above, particularly at low added  $[H_2]$ . The defining of new species as described above was necessitated by the lack of kinetic information on the more active radiolysis species, although the standard reduction potentials for some of the species have been estimated [3],

as listed in Table 1. However, because the concentrations of  $e^-$ , H,  $H_2O_2$ , and OH are so small, their redox currents are mass transfer controlled and hence are insensitive to the kinetic parameters (exchange current density, Tafel constants).

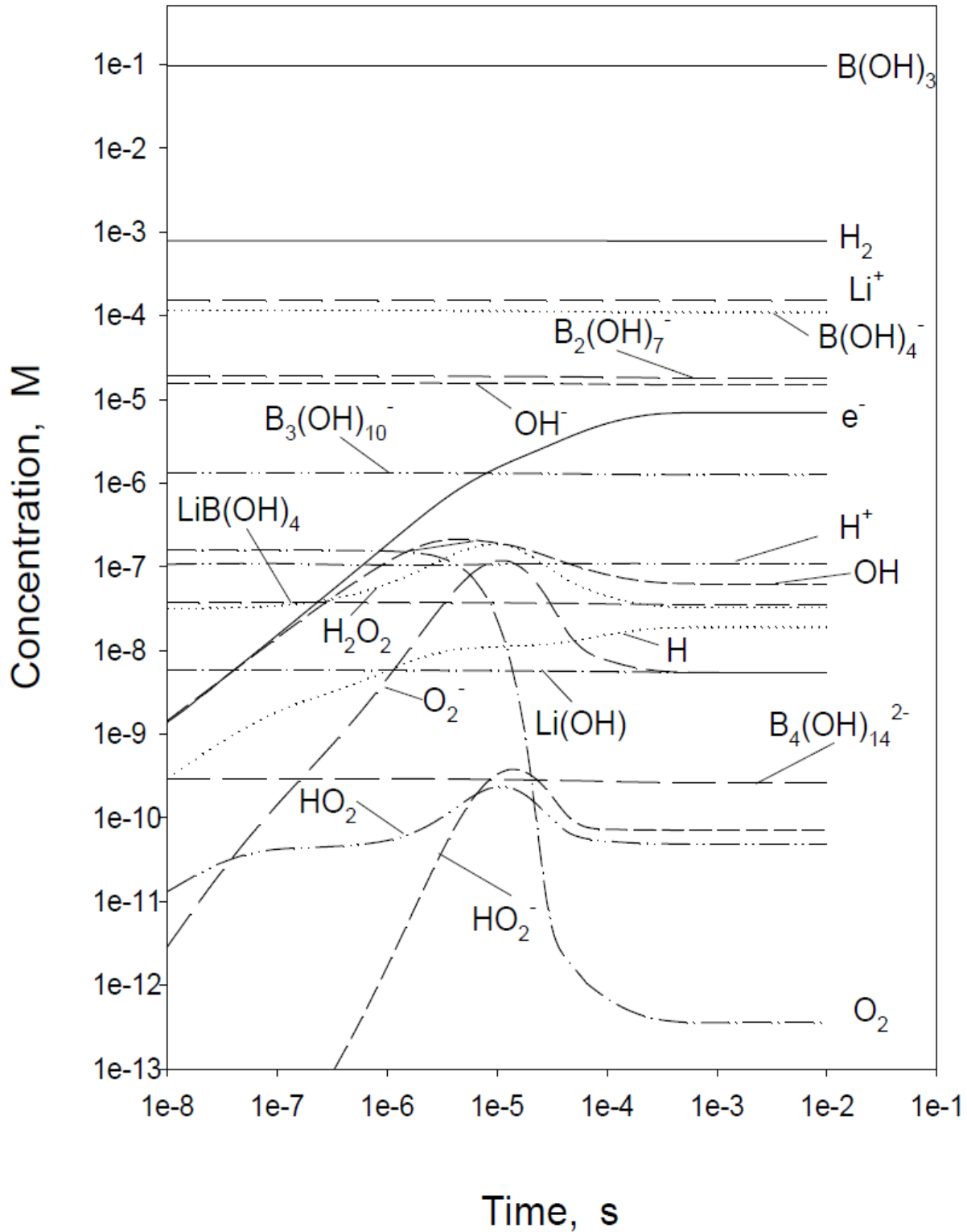


**Figure 2.** Predicted concentrations of radiolysis and pH control species in the primary coolant of a PWR as a function of time towards achieving a local steady state for  $C_{B,T} = 1500$  ppm,  $C_{Li,T} = 1.5$  ppm,  $T = 300$  °C,  $[H_2] = 25$  cm<sup>3</sup>/kg STP,  $\Gamma_n = 1 \times 10^{20}$  eV/cm<sup>3</sup>s, and  $\Gamma_\gamma = 3 \times 10^{21}$  eV/cm<sup>3</sup>s [7].

Compared with the work reported on modeling BWR primary coolant circuits [1], much less work has been reported on assessing electrochemical effects in PWR primary circuits [1], and even less has been reported specifically about the ITER. This state of affairs reflects the fact that cracking has not been as great a problem in PWR primary coolant circuits as it has been in BWR primary coolant circuits. However, although the primary water stress corrosion cracking (PWSCC) of mill-annealed Alloy 600 steam generator tubes, pressurizer components, control rod drive tubes, and baffle bolts (highly cold-worked Type 316 SS) have been serious, recurring issues in PWR operation, for example, and because the ITER has yet to operate the issue of what may happen in a fusion reactor (e.g., ITER) is perhaps moot. Because of the high hydrogen concentration [typically 25 cc(STP)/kg(H<sub>2</sub>O)–50 cc(STP)/kg(H<sub>2</sub>O) corresponding to  $1.12 \times 10^{-3}$  m to  $2.24 \times 10^{-3}$  m or 2.23 to 4.46 ppm] employed in a PWR primary circuit to “suppress radiolysis,” and in view of the lack of sustained boiling, it was generally believed that the ECP is dominated by the hydrogen equilibrium potential and hence that the coolant circuit acts as a “giant hydrogen electrode”, as noted above. If so, an approximate value of the ECP is readily calculated from the known pH, which, in turn, is easily estimated from the boron and lithium contents of the primary coolant, and the known hydrogen concentration using the Nernst equation. Considering subsequent modeling, this picture is not entirely accurate; more importantly, though, PWRs are not free from cracking in their primary circuits, and the cracking that is observed is very potential dependent. For example, Primary Water Stress Corrosion Cracking (PWSCC) of Alloy 600 steam generator tubes has plagued operators for many years, as noted above, and cracking of core barrel bolts (highly cold-worked Type 316 SS) has also been a recurring problem. While there are significant materials differences between BWR and PWR primary circuits, in both cases it has gradually become evident that the electrochemistry of the coolant is a prime factor in the nucleation and propagation of corrosion damage [8]. A discussion of the chemistry of the primary coolant circuits of both BWRs and PWRs, and of the proposed chemistry of the ITER coolant, is relevant, because in many respects the envisioned chemistry of the ITER PHTS blends the chemistries of both of those fission reactors, and because there are many lessons that were learned from experiences within the fission reactor community that appear not to have been heeded in ITER. This parallels the situation that existed in the dawn of the fission reactor age, when it was regarded that a fission reactor was like a conventional thermal (fossil fueled) plant “with a different heat source”. This led to many of the corrosion problems that have plagued fission plants over the past fifty years.

## 2. The Electrochemical Corrosion Potential (ECP)

As noted above, the ECP is the single most important parameter in assessing whether and what type of corrosion can be expected to occur in the PHTS of a nuclear reactor [8]. This is because corrosion processes tend to occur above or below critical values of the ECP,  $E_{crit}$ . Numerous attempts have been made to measure the ECP in various locations in both BWRs and PWRs by devising reference electrodes that can operate under the harsh thermal/radiolytic conditions that exist within the PHTS of a reactor. The most successful reference electrode to date is the Ag/AgCl, KCl that was used by Indig and Nelson [9] to measure ECP in the core of an operating BWR. As noted above, there has been a trend to use a platinum electrode as a reference in reactor PHTSs, but this is problematic from an electrochemical viewpoint for the following reasons. First, a noble metal like Pt is an indicator electrode whose potential responds to changes in the very redox conditions that determine the ECP. Since only differences in potential can be measured (a voltmeter is a two-port device), a Pt electrode cannot yield a reliable measure of the ECP, which ideally is expressed on the universally accepted, absolute scale of the standard hydrogen electrode (SHE). The only exception is in an environment in which the hydrogen fugacity is so high, and the concentrations of all oxidizing species are so low that the reference potential of the Pt is governed entirely by the hydrogen electrode reaction. In this case, the reference electrode potential is readily corrected to the SHE scale. However, under

these circumstances, the indicator electrode potential (i.e., the potential of the component being measured) is also governed by the same factors and hence any measurement is of questionable validity. Importantly, the potential may be calculated thereby negating the need for measurement.

Experience has shown that in-plant ECP measurements are intrusive and can only be made in a few areas of a reactor PHTS. Fortunately, the ECP can be calculated with acceptable accuracy using a Mixed Potential Model (MPM) [10], so that a strategy that has evolved is to calibrate (if necessary) the MPM on the available, measured ECP data and then use the model to calculate the ECP at closely spaced points around the primary coolant circuit using the concentrations of radiolytically generated species using a water radiolysis code [1]. Other electrodes that have displayed acceptable service in high temperature aqueous environments like reactor coolants are the YSZ(M/MO<sub>2</sub>), M = Hg, Ni, Cu), where YSZ = Yttria Stabilized Zirconia [11] and W/WO<sub>3</sub> [12], albeit both being more complex than a simple Pt wire. Importantly, the potentials of these electrodes may be placed on the SHE scale via chemical thermodynamic calculation and they are insensitive to redox potential but are sensitive to pH. However, the pH may be accurately calculated using appropriate chemical models and hence the potential may be corrected for changes in pH.

The MPM [10] is based upon the fact that charge conservation must be obeyed in a physico-electrochemical system. Noting that rate of an electrochemical reaction at a metal/solution interface is measured by the partial current density, the conservation of charge constraint requires that the sum of all partial current densities at the interface must be zero.

$$\sum_{j=1}^n i_{R/O,j}(E) + i_{corr}(E) = 0 \quad (1)$$

where  $i_{R/O,j}$  is the partial current density due to the  $j$ -th redox couple in the system and  $i_{corr}$  is the metal electro-dissolution (corrosion) current density. These partial currents depend on the potential drop across the metal/solution interface (or, practically, the potential difference between the metal and a suitable reference electrode). In the original version of the MPM [10], as developed for modeling the ECP of Type 304 SS in BWR primary circuits, the steel electro-dissolution current density,  $i_{corr}$ , is described by the empirical function of voltage, based on the data of Lee [10],

$$i_{corr} = \frac{e^{(E-E_0)/b_f} - e^{-(E-E_0)/b_r}}{384.62e^{4416/T} + X} \quad (2)$$

where

$$X = \frac{e^{(E-E_0)/b_f}}{2.61 \times 10^{-3}e^{-4416/T+0.523(E-E_0)^{0.5}}} \quad (3)$$

and

$$E_0 = 0.122 - 1.5286 \times 10^{-3}T \quad (4)$$

The quantities,  $b_f$  and  $b_r$  are the forward and reverse Tafel constants, respectively, for the metal dissolution reaction, with values of 0.06 V being adopted for both. In fact, they are empirical constants that were assumed a priori in fitting Equation (2) to the current/voltage data of Lee [10]. Note that Equation (2) applies strictly to Type 304 SS in near neutral solutions and, accordingly, it may not be valid for stainless steels in PWR primary circuits, for example. More recently, the Point Defect Model [13] has been developed for describing the electro-oxidation of a passive metal. This model yields the passive current density in the form

$$i_{corr} = a * \exp(bE) + c \quad (5)$$

where the parameters  $a$ ,  $b$ , and  $c$  are defined in terms of fundamental parameters [13]. The first term on the right side of Equation (5) arises from the transmission of cations via cation vacancies across the passive film from the metal/barrier layer (m/bl) interface to the barrier

layer/solution (bl/s) interface, while the second term reflects the transmission of oxygen ions via oxygen vacancies and/or metal interstitials in the reverse direction. The values of  $a$ ,  $b$ , and  $c$  are determined by optimizing the PDM on wide-band, electrochemical impedance spectroscopic (EIS) data measured on the material under the appropriate conditions [14]. The resulting MPM yields ECP values that are only marginally different (within a few mV) from those calculated using Equation (2).

The current density ( $i_{R/O}$ ) for a redox couple (e.g.,  $O_2/H_2O$ ,  $H^+/H_2$ ,  $H_2O_2/H_2O$ ),  $R \Leftrightarrow O + ne$ , where  $R$  is the reduced species and  $O$  is the oxidized species, can be expressed in terms of a generalized Butler-Volmer equation as [10]:

$$i_{R/O} = \frac{e^{(E-E_{R/O}^e)/b_a} - e^{-(E-E_{R/O}^e)/b_c}}{\frac{1}{i_{0,R/O}} + \frac{1}{i_{l,f}} e^{(E-E_{R/O}^e)/b_a} - \frac{1}{i_{l,r}} e^{-(E-E_{R/O}^e)/b_c}} \quad (6)$$

where  $i_{R/O}$  is the exchange current density,  $i_{l,f}$  and  $i_{l,r}$  are the mass-transfer limited currents for the forward and reverse directions of the redox reaction, respectively, and  $b_a$  and  $b_c$  are the anodic and cathodic Tafel constants. The parameter  $E_{R/O}^e$  is the equilibrium potential for this reaction as computed from the Nernst equation:

$$E_{O/R}^e = E_{O/R}^0 - \frac{2.303RT}{nF} \log\left(\frac{a_R}{a_O}\right) \quad (7)$$

where  $a_R$  and  $a_O$  are the thermodynamic activities of  $R$  and  $O$ , respectively, and  $E_{R/O}^0$  is the standard potential, which may be calculated as a function of temperature from electrochemical thermodynamics. Limiting currents are calculated using the dimensionless mass transfer correlation equation for flow through a pipe as [10]:

$$i_{l,O/R} = \pm 0.0165nFD C_{O/R}^b Re^{0.86} Sc^{0.33} / d \quad (8)$$

where the sign depends on whether the reaction is in the forward (+) or reverse (-) direction,  $F$  is Faraday's number,  $D$  is the diffusivity of the redox species,  $C_{O/R}^b$  is the bulk concentration of  $O$  or  $R$ , as appropriate,  $Re$  is the Reynolds number ( $Re=Vd/\eta$ ),  $Sc$  is the Schmidt number ( $Sc = \eta/D$ ),  $d$  is the channel diameter,  $V$  is the flow velocity, and  $\eta$  is the kinematic viscosity [10].

In a recent innovation to the MPM [15,16], a quantum mechanical correction to the exchange current density ( $i_{0,O/R}$  for the presence of the barrier oxide layer of the passive film has been applied to more accurately describe the kinetics of redox reactions on passive metals where the thickness of the barrier oxide layer, through which the charge carriers ( $e^-$ ,  $h^+$ ) must tunnel from the metal Fermi level to an empty acceptor state at the same energy for the oxidized species  $O$  at the barrier layer/solution interface. Thus, the barrier layer represents a tunnel barrier to the transfer of electron charge carriers (electrons and electron holes) and, from quantum mechanical tunneling (QMT) theory [17], the exchange current density can be expressed as:

$$i_{0,O/R} = \hat{i}_{0,O/R} \exp(-\hat{\beta} L_{ss}^e) \quad (9)$$

where  $\hat{\beta}$  is the tunneling constant ( $\approx 0.6 \times 10^8 \text{ cm}^{-1}$  [17]),  $L_{ss}^e$  is the steady-state thickness of the barrier layer at the HER equilibrium potential, and  $\hat{i}_{0,O/R}$  is the (hypothetical) exchange current density of  $O/R$  on the film-free surface. From the PDM, the thickness of the barrier layer under the HER equilibrium potential is given as:

$$L_{ss}^e = \frac{1-\alpha}{\epsilon} E_{HER}^e + G \quad (10)$$

where  $\alpha$  is the polarizability of the bl/ol interface,  $\varepsilon$  is the electric field strength, and

$$G = \left( \frac{c_7 - c_3}{b_3} \right) pH + \frac{1}{b_3} \ln \left[ \frac{k_7^0}{k_3^0} \left( C_H / C_{H^+}^0 \right)^n \right] \quad (11)$$

The parameters in G are defined elsewhere [17] but are readily obtained by optimizing the PDM on EIS data [14]. Substitution of Equation (10) into Equation (6) yields:

$$i_{HER} = \frac{e^{\eta/b_a} - e^{-\eta/b_c}}{\frac{e^{[\hat{\beta}(1-\alpha)E/\varepsilon]e^{(\hat{\beta}G)}}}{i_0} + \frac{e^{\eta/b_a}}{i_{i,f}}} \quad (12)$$

The bare surface exchange current density is termed “hypothetical” because such a surface cannot be realized in practice on alloys that are of interest in reactor PHTSs (Fe-Ni-Cr alloys) within the kinetic stability range of water since the barrier oxide (typically  $\text{Cr}_2\text{O}_3$ ) forms at a potential that is much more negative than the equilibrium potential of the HER. Any attempt to displace the potential to a sufficiently negative voltage to reduce  $\text{Cr}_2\text{O}_3$  results in massive hydrogen evolution that renders such experiments impractical. However, the great advantage of this formulation of electrochemical kinetics of redox reactions on passive surfaces is that a great body of data exists for exchange current densities on the noble metals, such as Pt and Au and, because modern computational methods, especially Density Functional Theory, there is promise for being able to estimate exchange current densities of redox reactions on bare metal surfaces at some time in the future. This may be a route for obtaining values in the future for the kinetic parameters for the highly reactive redox couples listed in Table 1. The thickness,  $L_{ss}^e$ , is found to range from about 0.1 nm to 1.0 nm within the range of variance of  $E_{HER}^e$ , depending upon the potential [see Equation (10)] so that the maximum value of  $i_{0,O/R} / \hat{i}_{0,O/R} = 2.5 \times 10^{-3}$ . Thus, the QMT correction is significant and should be made where possible.

Because electrochemical kinetic data are available only for the hydrogen electrode reaction (HER,  $\text{H}_2/\text{H}^+$ ), the oxygen electrode reaction (OER,  $\text{O}_2/\text{H}_2\text{O}$ ), and the hydrogen peroxide electrode reaction (HPER,  $\text{H}_2\text{O}_2/\text{H}_2\text{O}$ ) by the assuming the same data as for the OER but with a different standard potential (1.77  $V_{\text{she}}$  vs. 1.23  $V_{\text{she}}$  at 25 °C, only  $\text{H}_2$ ,  $\text{O}_2$ , and  $\text{H}_2\text{O}_2$  can be considered as the redox species in the MPM. Furthermore, we currently have electrochemical kinetic data for these species only on Type 304 SS, Type 316 SS, Alloy 600, and Alloy 690 over the range of conditions that are of interest in nuclear power reactor technology [14], so that only these substrates can be modeled accurately at this time. However, significant evidence exists that Types 304 SS and 316 and Alloy 600 and 690 serve as good analogs for other stainless steels and nickel-base alloys. This is based on the observation that all these chromium-containing alloys form barrier layers of passive films that are essentially substituted, defective  $\text{Cr}_2\text{O}_3$  and that have the same thickness at any given potential. Because the exchange current density of a redox species is determined by resonant quantum mechanical tunneling (RQMT) of charge carriers across the barrier layer of the passive film, the tunneling probability and hence the current is independent of the phase identity of the barrier layer provided that the barrier height is reasonably constant. Accordingly, the exchange current densities for any given redox reaction on a wide variety of Fe-Cr-Ni alloys are expected to be similar and not to depend on the chemical identity of the barrier layer phase, because QMT is independent of the phase through which tunneling occurs. This is, indeed, observed. Furthermore, the electro-oxidation current densities for various Fe-Cr-Ni alloys in the same solutions and under the same conditions are also similar, again reflecting the essentially similar thicknesses of the passive films [14]. Accordingly, the ECP, which reflects a balance between the partial currents for the anodic reactions (substrate oxidation and hydrogen oxidation) and the cathodic reactions (reduction of oxygen and hydrogen peroxide) that occur on the substrate surface, should be similar. No electrochemical data are available for Zircaloy, so that the

ECP of this substrate cannot be currently modeled. However, the code has been written so that appropriate values are readily inserted when they become available.

As noted above, the redox reactions of interest in this study are:



as was found in the modeling of ECP in BWRs [10]. Note that the reactant concentrations are redefined, as noted above, as:  $[\text{H}_2^*] = [\text{H}_2] + 0.5[\text{H}] + 0.5[e_{\text{aq}}^-]$ ,  $[\text{H}_2\text{O}_2^*] = [\text{H}_2\text{O}_2] + 0.5[\text{OH}]$  and  $[\text{O}_2^*] = [\text{O}_2] + 0.5[\text{O}]$ . For simplicity, we drop the asterisk from hereon. Using the data available from the published literature for the constants and the coefficients [10,13], the ECP can be calculated by solving Equation (1).

An important point that needs to be emphasized again is that the maximum contribution that any given radiolytic species can make to the ECP is roughly proportional to its concentration. Thus, in BWR simulations, the concentrations of  $\text{H}_2$ ,  $\text{O}_2$ , and  $\text{H}_2\text{O}_2$  are calculated to be orders of magnitude greater than any other radiolytic species, corresponding to the modified Burns and Moore [18] reaction set adopted for the modeling [1,8,19], and hence only these three need to be considered. In the case of PWR primary HTCs, our previous modeling [1,8,19] suggests that aquated electrons, H atoms, and OH radicals may be the most significant radiolytic species in regions of very high-energy dose rate (e.g., near the fuel). However, no electrochemical kinetic data exist for these species and hence they cannot be directly incorporated at this time, but they are indirectly incorporated by redefining the concentrations, as noted above.

Some example calculations of the ECP for Type 304 SS in a PWR primary coolant are shown in Figure 3 for the conditions stated in the caption. The ECP is seen to vary sigmoidally with increasing oxidant concentration and is more positive for  $\text{H}_2\text{O}_2$  as the oxidant than it is for  $\text{O}_2$  (Figure 3). The ECP at the lower oxidant limits corresponds,  $-0.79 \text{ V}_{\text{SHE}}$ , corresponds closely to the calculated HER equilibrium potential. The ECP deviates in the positive direction when the oxidant concentration exceeds 1 ppb, demonstrating that, even in a PWR coolant environment, the ECP is sensitive to low concentrations of oxidizing radiolysis products, as noted from Figure 1. The curves of ECP vs. [Oxidant] do not bifurcate until an oxidant concentration of about 10 ppb exists, after which the ECP for  $\text{H}_2\text{O}_2$  becomes significantly (and increasingly so) more positive than that for  $\text{O}_2$ . The critical oxidant concentration of 1  $\mu\text{g}/\text{kg}$  (1 ppb,  $0.5 \times 10^{-6} \text{ m}$ ) at which the ECP is displaced from the hydrogen electrode behavior is in good semi-quantitative agreement with experimental data obtained from laboratory studies by Bertuch, et al. [4] (Figure 1). Because most PWRs operate with high hydrogen levels [20–70 cc(STP)/kg  $\text{H}_2\text{O}$ ], radiolysis is suppressed and the concentrations of oxidizing species are very low ( $\ll 1$  ppb), so that the PHTSs of these reactors display ECP values that are about  $-800 \text{ mV}_{\text{she}}$ .

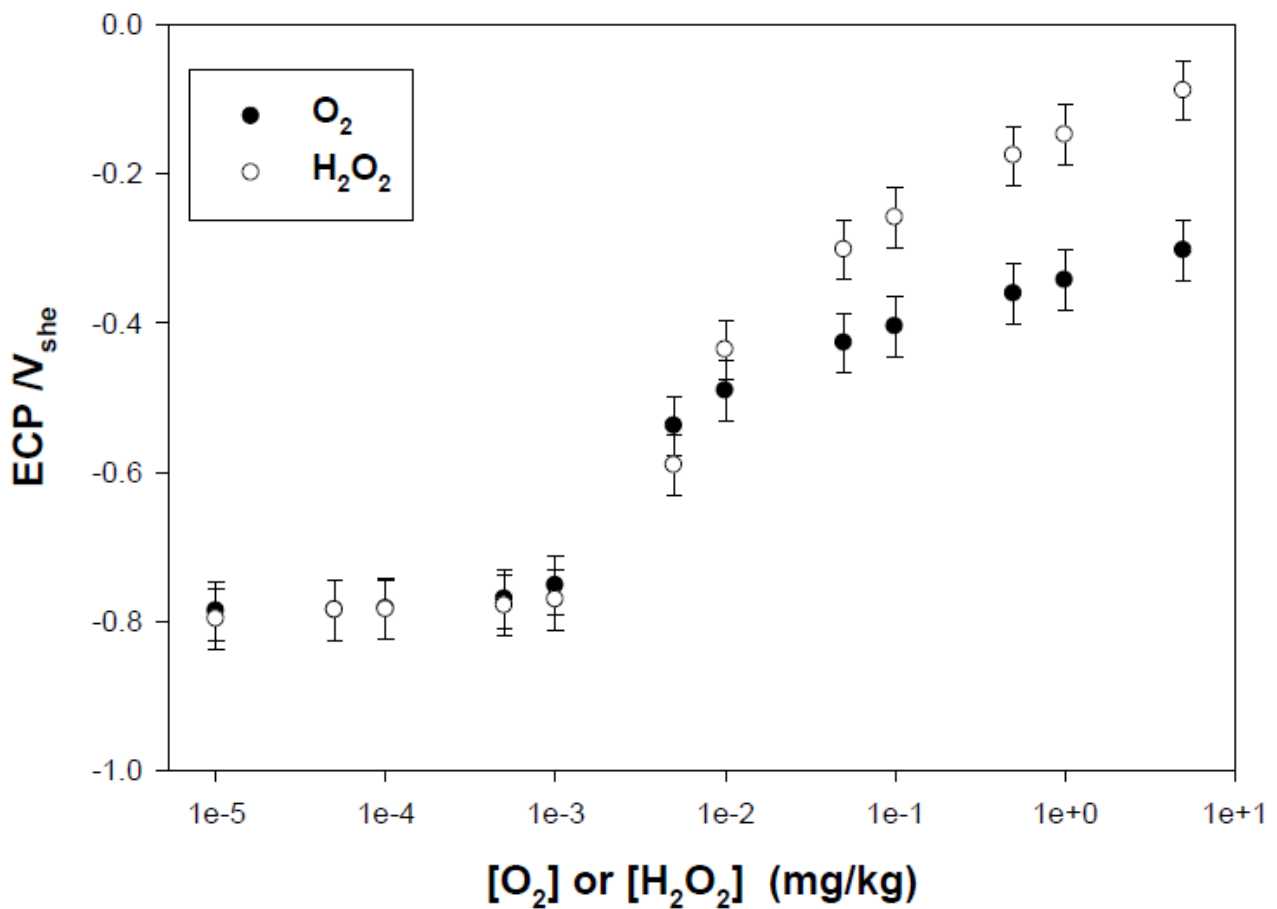


**Figure 3.** Calculated ECP for Type 304 SS as a function of [H<sub>2</sub>O<sub>2</sub>] and [O<sub>2</sub>] in simulated PWR coolant at 320 °C, [B] = 1000 mg/kg, [Li] = 2 mg/kg, [H<sub>2</sub>] = 25 cc/kg (2.23 mg/kg), pH = 7.36, flow velocity = 100 cm/s, channel hydrodynamic diameter = 100 cm [20].

One issue that is seldom recognized when assessing the dependence of the ECP on plant operating parameters is the dependence on fluid flow velocity [10]. This dependence arises, because of the dependencies of the limiting currents on flow velocity as expressed by Equation (8). The importance of this effect is displayed in Figure 4. The figure also shows the range of ECP that have been reported in practice from both laboratory and in-plant measurements and it is evident that the ECP is hypersensitive to Re (and hence flow velocity) in the transition region between 1 and 20 ppb O<sub>2</sub>. This is the coolant oxygen concentration for BWRs operating on HWC with feedwater hydrogen of about 0.5 ppm. For NWC operation, [O<sub>2</sub>] is about 200 ppb in the recirculation piping system, which places the ECP at  $0 \pm 0.1 V_{she}$  (Figure 4). An important point from this graph is that the system may change from a non-cracking state where  $ECP < E_{crit}$  ( $-0.23 V_{she}$  at 288 °C) to a cracking state of  $ECP > E_{crit}$  merely by changing the flow velocity without changing species concentrations. Furthermore, the large scatter observed in the laboratory measurements reflects the poor control that most experiments have of the mass transfer conditions. This is a good illustration of the complexity of the factors that control the ECP in operating BWRs.

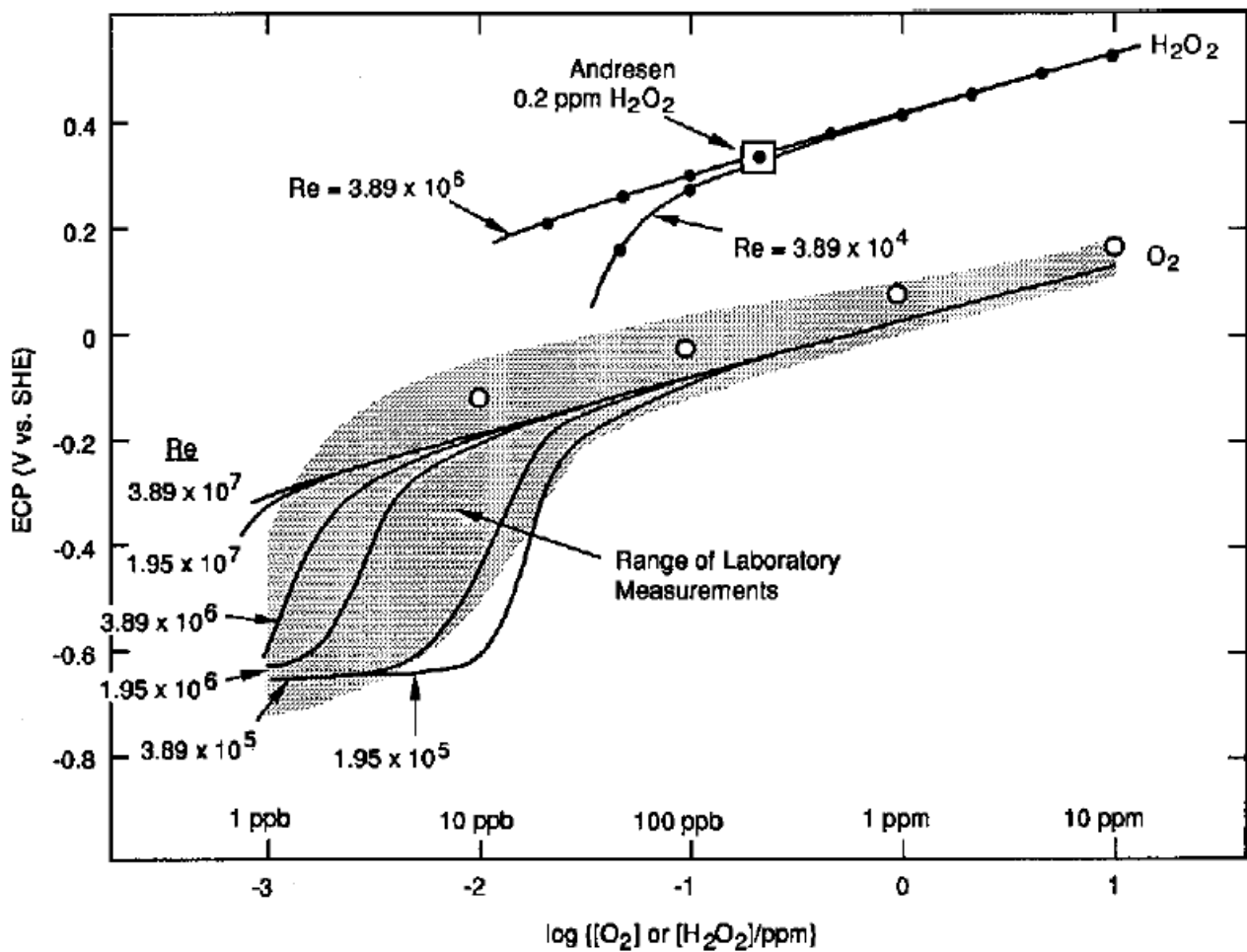


**Figure 4.** Calculated ECP vs. log [Oxidant] as a function of Reynolds number for Type 304 SS in BWR primary environment under NWC conditions at 288 °C. The Re values correspond to a 50 cm ID pipe with flow velocities ranging from 1 to 10 m/s, which are typical for a BWR recirculation piping system [10].

The accuracy of the Mixed Potential Model in predicting ECP has been evaluated by comparing calculated ECP values for Type 304 SS against measured BWR plant data (Figure 5). These data are considered to be particularly important, because the original authors also reported values for the concentrations of oxygen and hydrogen (but not  $\text{H}_2\text{O}_2$ ), and we employ those data that were obtained during a Hydrogen Water Chemistry (HWC) mini-test at the Leibstadt BWR in Switzerland [21,22]. The vendor retained us to model the reactor chemistry and predict the ECP in a “double blind” manner (i.e., we did not have access to the ECP data prior to submission of our calculations and the vendor did not have access to our calculations while performing the mini-test). We were, of course, provided with the required input data, such as the flow velocity, hydrodynamic diameter,  $[\text{H}_2]$ , and  $[\text{O}_2]$ , and temperature data for the test system. The calculated and measured (plant) ECP data for this case are summarized in Figure 5. Excellent agreement is obtained in systems to which hydrogen had been added, with the measured and calculated ECP values agreeing within the combined uncertainty levels. In the normal water chemistry case, the measured ECP is significantly higher than the calculated value. This is almost certainly due to the presence of hydrogen peroxide in the coolant, which was not measured by the personnel conducting the HWC mini test. Accordingly, we were unable to input a value for  $[\text{H}_2\text{O}_2]$  into the MPM. However, if we use the calculated values for  $[\text{H}_2]$ ,  $[\text{O}_2]$ , and  $[\text{H}_2\text{O}_2]$  obtained from our radiolysis code, excellent agreement is obtained over the entire hydrogen concentration range [21,22].

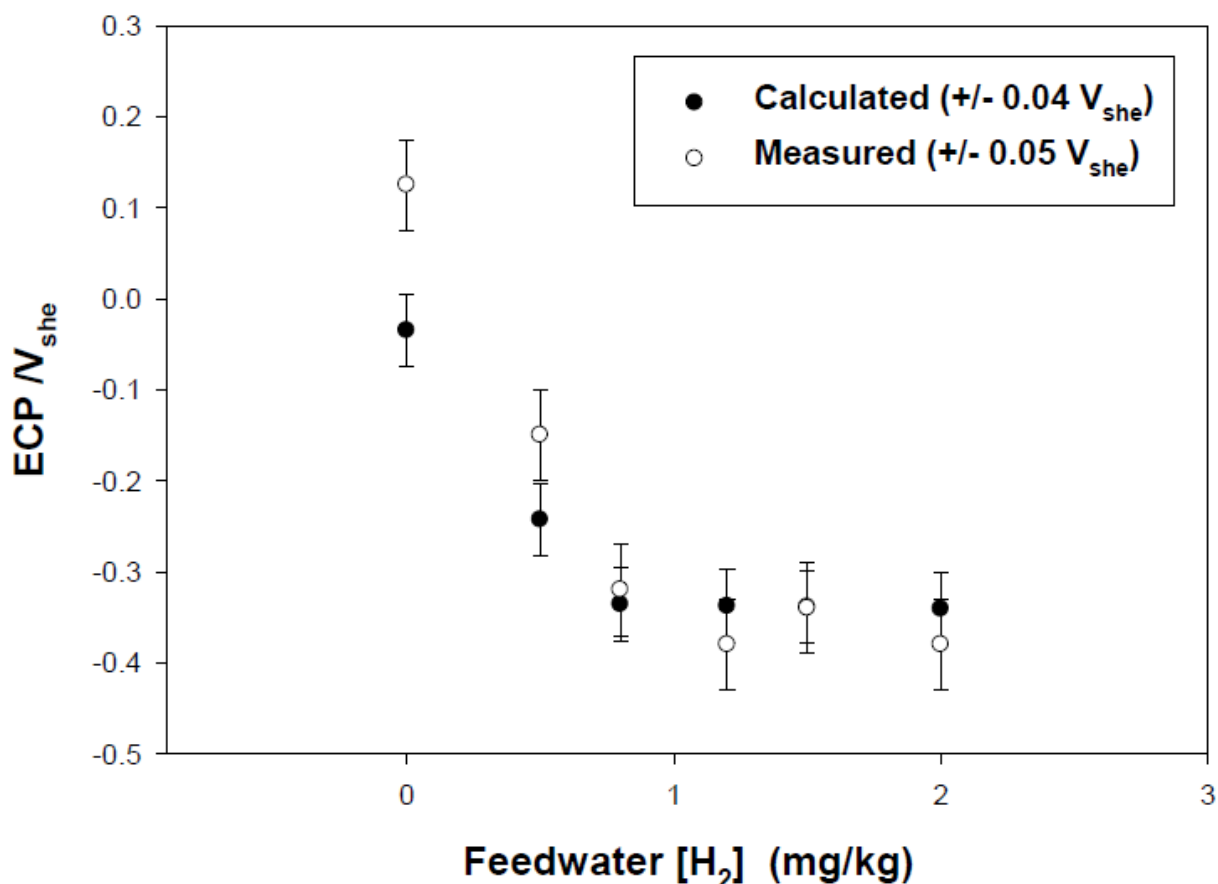


**Figure 5.** Comparison of calculated and measured ECP in a test cell attached to the recirculation piping in the Leibstadt BWR as a function of the concentration of hydrogen added to the feedwater. The concentrations of O<sub>2</sub> and H<sub>2</sub> concentration were supplied from the vendor. No data for H<sub>2</sub>O<sub>2</sub> was available so that this species was not incorporated in the calculation (see text) [21,22].

Additional studies on modeling the electrochemical and corrosion properties of BWR coolant circuits are presented later in this review in Section 5.

### 3. Calculation of Crack Growth Rate

The ultimate goal of modeling the electrochemistry of reactor coolant circuits is to calculate the crack growth rate in structural materials and then to estimate the accumulated damage (i.e., crack length vs. time) along the corrosion evolutionary path (CEP, i.e., the operating history) of the reactor. Various models have been proposed for calculating crack growth rate in PHTS structural materials, such as the austenitic stainless steels (like Type 304 SS, Type 316 SS) and nickel-base alloys, such as Alloy 600. A comprehensive review of all proposed models is beyond the scope of this review, so that attention is focused on describing those models that explicitly incorporate electrochemistry, because the ECP is the key parameter in determining the ECP and the CGR. The only deterministic model (i.e., one whose output is constrained by the natural laws) that has been developed to date is the Coupled Environment Fracture Model (CEFM) [23] and variants thereof [24], so that the present discussion is restricted to the CEFM.

The basis of the CEFM is the differential aeration hypothesis (DAH), as illustrated in Figure 6. Thus, SCC occurs because of the separation of the local anode (in the cavity) and the local cathode (on the external surfaces that have maximum exposure to the cathodic depolarizers (O<sub>2</sub>, H<sub>2</sub>O<sub>2</sub>, H<sub>2</sub>)). As a result, a net positive, ionic current flows through the solution inside the crack and then through the external environment from the crack tip, where it is produced by the electro-dissolution of the steel to the external surfaces,

where it is annihilated by charge transfer reactions [Reactions (13)–(15)] and the matching electron current flowing through the metal from the crack tip. That current is termed the “coupling current (CC)”, because it couples the internal (crack enclave) and crack external environments, hence the name of the model. For a model to be deterministic and hence robustly predictive, the system must be constrained by the conservation of charge, which is stated here as [23]:

$$\int_S idS = 0 \quad (16)$$

where  $dS$  is an increment the area of the interface between the metal and the environment, including that within the crack.

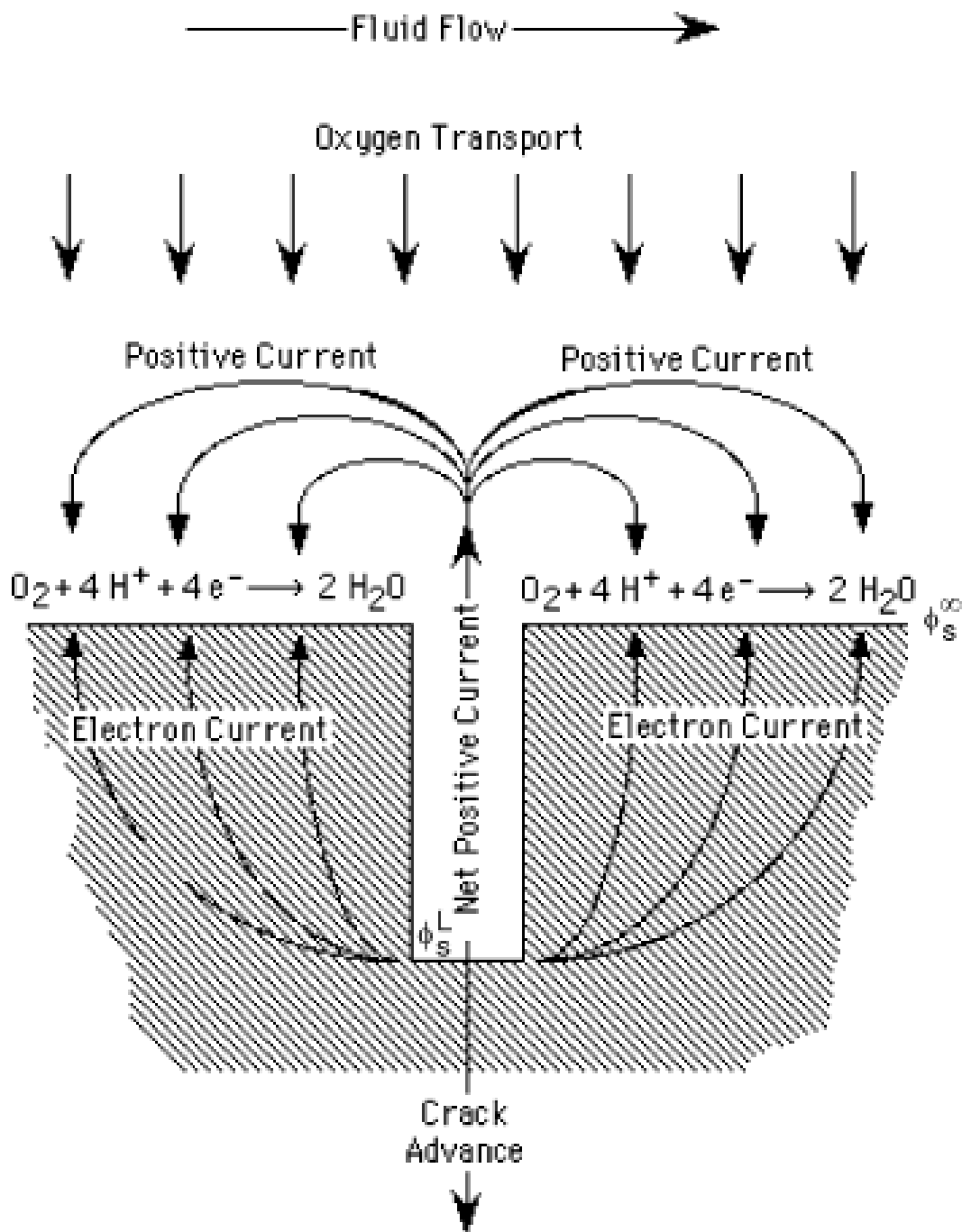


**Figure 6.** Schematic of differential aeration in localized corrosion such as stress corrosion cracking (SCC), intergranular stress corrosion cracking (IGSCC), pitting corrosion, and crevice corrosion [19].

The integral is evaluated over the entire area, but modeling shows that, because the net current on the external surface decreases exponentially and asymptotically towards zero as the distance on the external surface increases from the crack mouth, the effective distance (“throwing power”) is limited. Indeed, the integral needs to be evaluated over a region of about  $\pm 10$  crack opening dimensions on either side of the crack for most conditions of interest. Now, mathematically, an infinite number of solutions of the Nernst-Planck equations coupled with Poisson’s equation exist for the distributions of species concentrations and potential, and hence the current, for the crack internal current depending upon the potential in the solution at the crack mouth. Likewise, an infinite number of solutions also exist for the distributions in the potential and the current on the external surface, depending upon the value of the same potential. However, there is only one value of the crack mouth potential for which Equation (16) is satisfied and that value imbues the model with determinism. Once this value is determined by iteration, together with an embedded iteration on the potential in the solution at the crack tip until electroneutrality is achieved, the corrosion current density is calculated and hence the crack growth rate is obtained via Faraday’s law.

The model adopted for describing the events that are envisioned to occur at the crack tip is the periodic slip/dissolution/repassivation model [25] from which the average metal dissolution current is determined. However, measurement of the micro crack dimension (MCD) coupled with the known crack growth rate for IGSCC in sensitized Type 304 SS in water at 250 °C (simulated BWR primary coolant) shows that the area of metal exposed upon each cycle (the “micro crack dimension”) is too large ( $\approx 2 \mu\text{m}$ ) to be accounted for by slip alone. If slip alone was the reason for crack advance, the MCD should be a small multiple of the Burgers vector or a few nm in size and the microfracture frequency (MFF) would have to be in the kHz range, rather than in the observed Hz range, to account for the measured CGR [26]. The strain rate at the crack tip, which is required for calculating the MFF was initially that of Ford and Andresen [27], but later those of Congleton [28] and Shoji [29], and finally that of Hall [30] were used. The current version of the CEFM employs Hall’s expression for the crack tip strain rate, and includes small scale yielding and strain-rate hardening effects. The CEFM predicts that the MFF is initially zero for  $K_I < K_{ISCC}$ , corresponding to the absence of environmentally assisted cracking (EAC), but quickly increases to about 2 Hz for  $K_I > K_{ISCC}$  (Figure 7). The latter condition demonstrates fracture by IGSCC and results in a microfracture dimension of nearly 2  $\mu\text{m}$ ; about a factor of 1000 larger than that expected from slip alone. The same type of analysis preformed on cracking in sensitized Type 304 SS in thiosulfate solution at ambient temperature [31] and in AISI 4340 steel in 7 M NaOH at 70 °C [32], both being well recognized as systems subject to hydrogen-induced (HIC), the crack dimensions were calculated to be 42–134  $\mu\text{m}$  and  $\approx 60 \mu\text{m}$ , respectively [33]. In the BWR environment, the MCD is sub grain sized (1/3 to 1/10 the grain size) but for the cases of Type 304 SS in thiosulfate and in AISI 4340 steel in 7 M NaOH at 70 °C, the MCD is super grain size. For this reason, cracking in Type 304 SS in BWR coolant is attributed to slip/dissolution/repassivation augmented by HIC, resulting from the injection of cathodically generated atomic hydrogen into the matrix ahead of the crack tip followed by recombination in creep-induced voids on the grain boundaries. This recognizes that some cathodic reaction (hydrogen evolution via proton reduction) occurs at the crack tip even though the bulk of the cathodic activity occurs on the external surfaces, as required for maintaining differential aeration. The resulting pressure within the voids is added to the hydrostatic stress at the crack tip, resulting in the increase in the MFF displayed in Figure 7. Additional details on the CEFM may be found in [34,35].

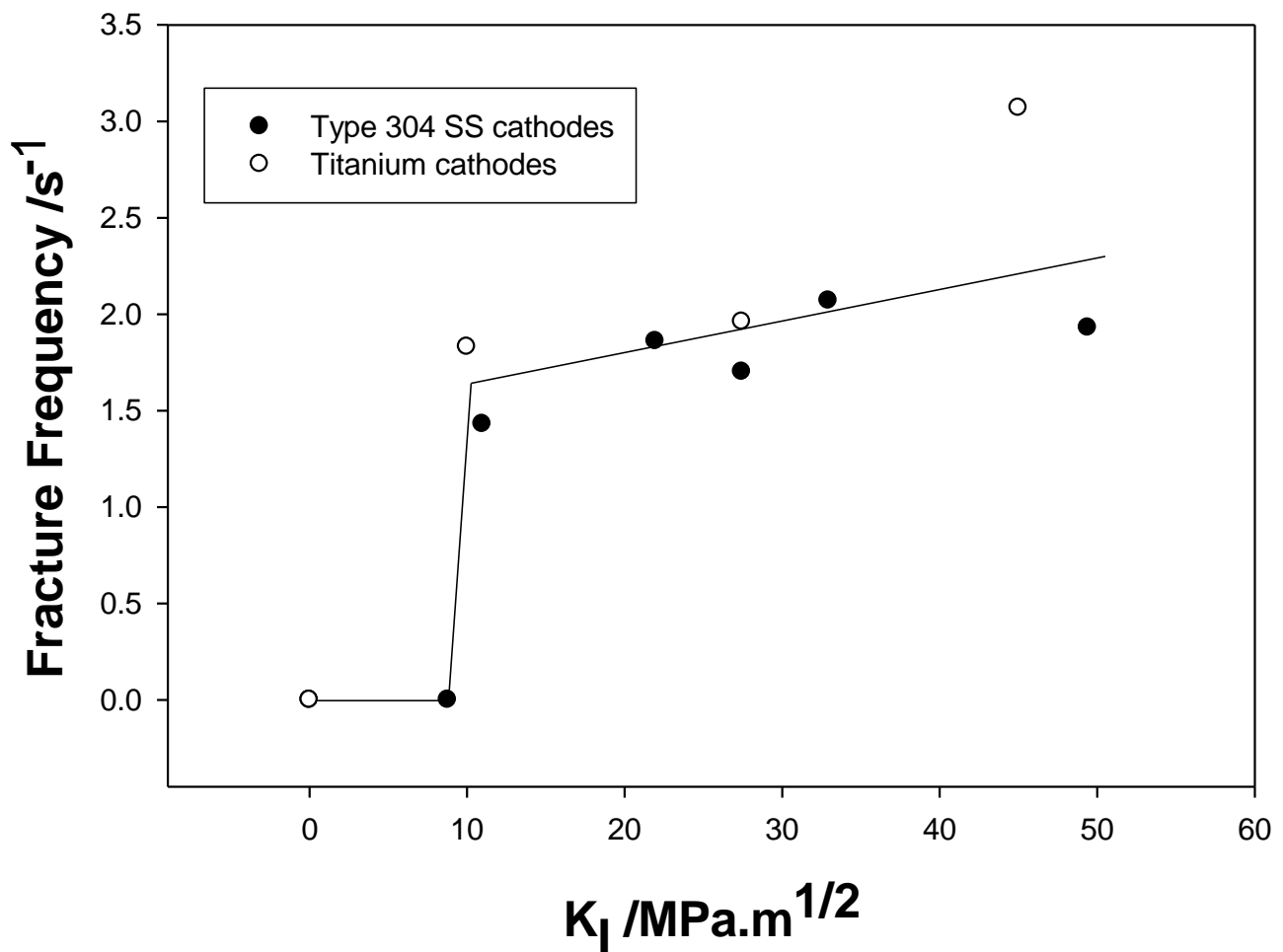


**Figure 7.** Frequency of the brittle micro fracture events versus stress intensity factor for IGSCC in sensitized Type 304 SS in water at 288 °C,  $\kappa$  (25 °C) = 0.5–1.3  $\mu\text{S}/\text{cm}$ ,  $[\text{O}_2] = 0.15 \times 10^{-3} \text{ m}$  [26].

Comparison of the CEFM predicted and measured CGR in sensitized Type 304 SS in BWR coolant as a function of the ECP for different values of the ambient temperature conductivity is shown in Figure 8. Of course, the conductivity at the operating temperature of 288 °C was used in the CEFM. In the light of the fact that the CEFM contains several poorly known parameters, such as the strain for fracture of the passive film at the crack tip, the CEFM was calibrated against two measured CGR data at different temperatures, one of which is shown in Figure 8. Two CGR data at different temperatures were necessary, so as to determine the activation energy [36], which was found to be 1000 kJ/mol when using the Congleton expression for the crack tip strain rate.

As stated previously, the ECP is the single most important parameter in determining the damage accumulation rate for corrosion, including IGSCC in sensitized Type 304 SS, and that position is borne out by the data presented in Figure 8. Thus, we see that the CGR increases exponentially with ECP [linear log(CGR) vs. ECP] at potentials over which environmental (electrochemical) effects dominate, i.e., at  $\text{ECP} > -0.2 V_{\text{she}}$ . Below this ECP, crack advance occurs by creep, which in the CEFM is described by the void nucleation model of Wilkinson and Vitek [23]. The CGR is also predicted to be a sensitive, positive function of the coolant conductivity, a property that is discussed at length by Lu, et al. [23]. Increasing coolant conductivity increases the throwing power of the coupling current across the surface external to the crack, thereby leading to a larger area for the reduction of the cathodic depolarizer (e.g., oxygen) and hence in a larger coupling current (CC). Since the coupling current is linearly related to the CGR by Faraday's law, the CGR increases correspondingly. At very high ECP ( $> 0.2 V_{\text{she}}$ ) the CGR is so large that mass transfer of

the cathodic depolarizer exerts an influence on the rate and the predicted  $\log(\text{CGR})$  vs. ECP correlations deviates negatively from the linear relationship that is apparent at lower ECP. Finally, it is noted that the Nuclear Regulatory Commission (NRC) sanctions a critical value for the critical potential of IGSCC as  $E_{crit} = -0.23 V_{she}$ , but we caution that the critical potential is a function of many variables, including temperature, degree of sensitization, and crack length, as discussed below.

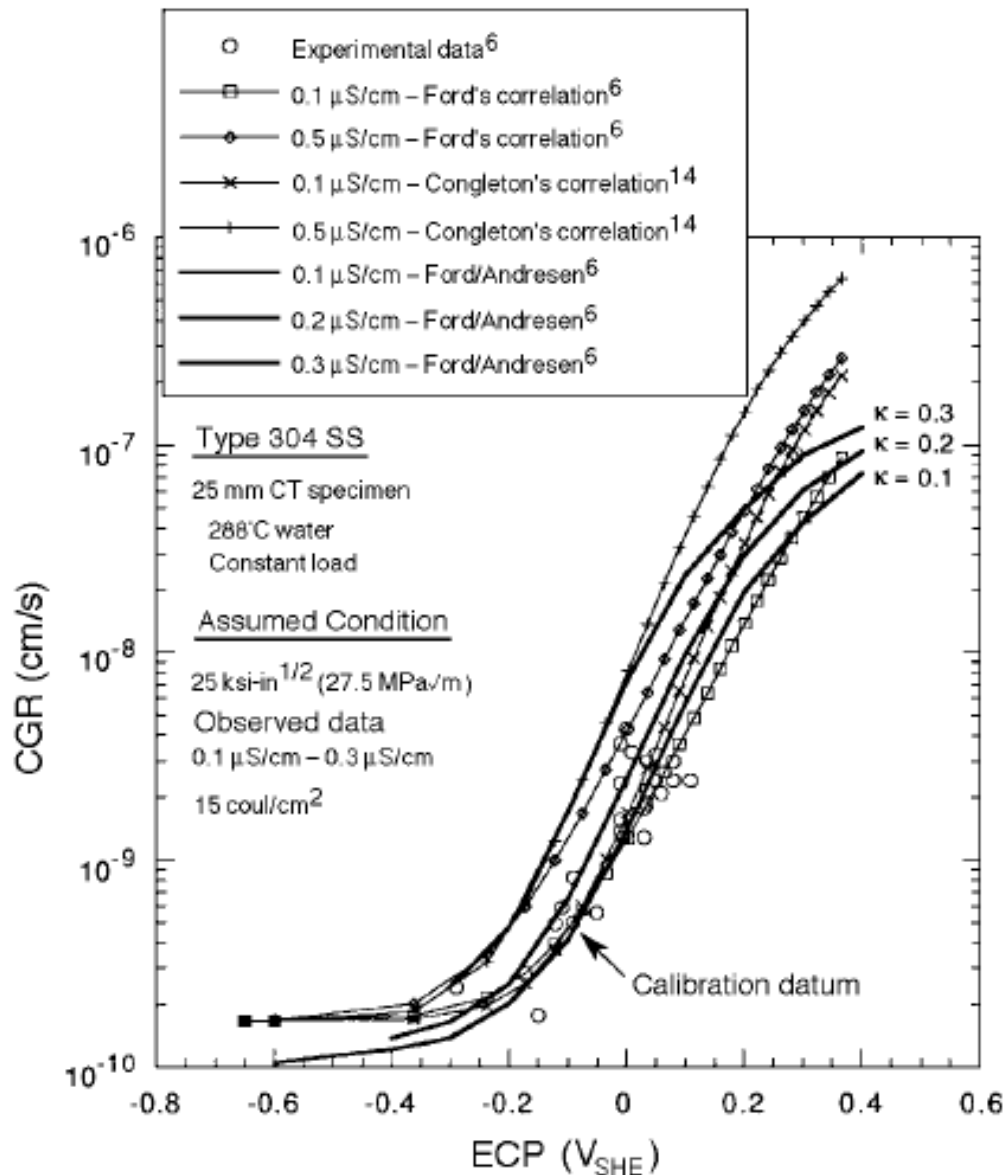


**Figure 8.** Comparison of the predicted dependence of the CGR on ECP in BWR coolant (water at 288 °C) for different values of the ambient temperature conductivity. The experimental data are from Ford and Andresen [27]. The citations in the figure are to the original source [19].

The predicted dependence of the CGR for sensitized Type 304 SS in BWR coolant on temperature is displayed in Figure 9 [36] together with experimental data from Andresen [37]. As seen, the CGR is predicted and found to pass through a maximum at about 170 °C, which has important implications for the accumulation of IGSCC damage during the start-up and shut down of BWRs. The maximum arises from the competing positive effect of temperature on the crack tip strain rate at low temperature and the negative effect of decreasing conductivity and especially decreasing ECP at higher temperatures.

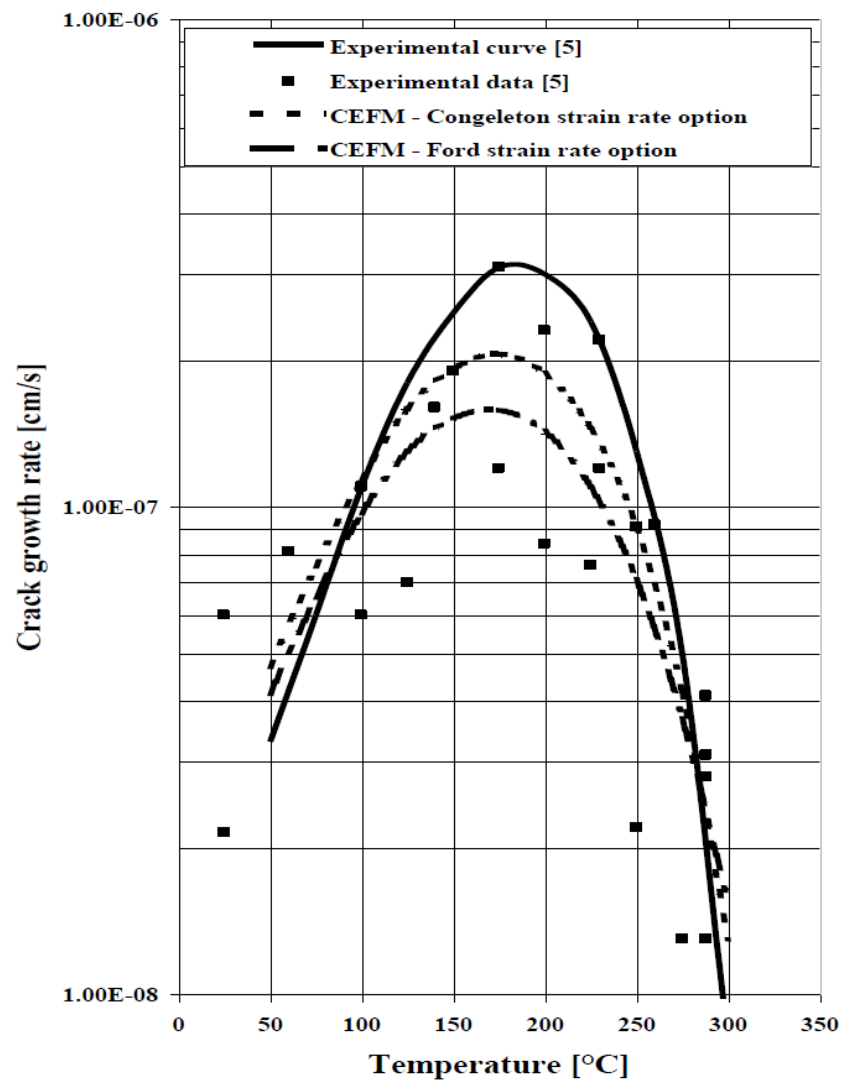


**Figure 9.** The effect of temperature on crack growth rate in Type 304 stainless steel in dilute sulphuric acid solution having an ambient temperature (25 °C) conductivity of 0.27  $\mu\text{S}/\text{cm}$  and a dissolved oxygen concentration of 200 ppb. The experimental data (curves) are taken from Andresen (see [36]). The model curves are calculated using the CEFM calibrated at 288 °C and assuming crack tip strain rate thermal activation energies of 75 kJ/mol or 100 kJ/mol when using the Ford or Congleton crack tip strain rate models, respectively [36,37]. The citations in the figure are to the original source [36,37].

A particularly important prediction of the CEFM is the dependence of the CGR on the electrochemical crack length (ECL), as shown in Figure 10 [23]. This dependence was missed in past experimental studies of crack growth, because standard fracture mechanics, C(T), specimens tend to be employed, in which the ECL stays essentially constant as the crack grows. This is because the ECL is the least resistive path through the solution from the crack front to the external surfaces; in the case of a through thickness crack in a C(T) specimen, that path is out through the crack opening on the specimen side rather than the much longer path down the crack and out through the crack opening at the mechanical loading location. Thus, the CEFM dictates that two crack lengths must be defined if stress corrosion cracking is to be understood mechanistically; a mechanical crack length (MCL), as defined conventionally, as being the distance between the load line and the crack front, and an electrochemical crack length (ECL), which is defined as being the shortest distance (least resistive path through the solution) between the crack front and the free external surface upon which the cathodic depolarizer reacts. It is this latter crack length that is indicated in Figure 10.

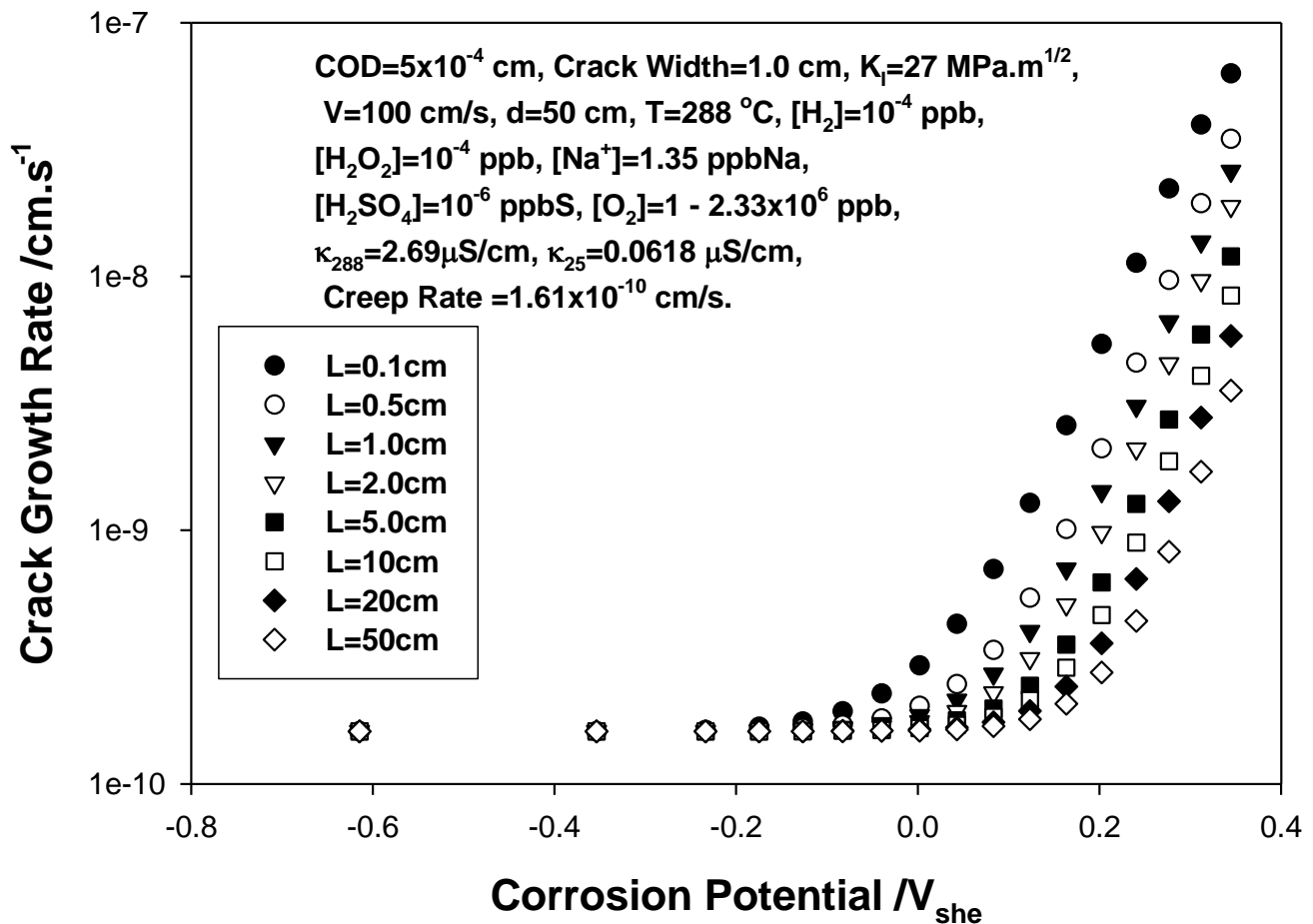


**Figure 10.** Predicted CGR in Type 304 SS in simulated BWR coolant as a function of ECP for different values of the crack length [23]. T = 288 °C.

When CT specimens are employed for measuring CGR, the shortest distance from the crack front is directly to the specimen side surface and this distance tends to be independent of the MCL. Indeed, the ECL obviously varies with position along the crack front, such that the crack growth rate should be greatest at the crack edges and least in the crack center. This is predicted to result in a convex crack front, as viewed from the crack mouth, as is commonly observed experimentally [33]. If cracking occurs by creep, the crack growth rate should be lower at the crack edge, where plain strain conditions are no longer fulfilled, than in the crack center and the crack front should appear concave, as is also commonly observed. An important prediction of the CEFM, as seen in Figure 10, is that the critical potential for IGSCC for a pre-existing crack is also a function of crack length. Thus, for the stated conditions,  $E_{crit} = -0.15 V_{she}$  for an ECL of 0.1 cm but is  $0.1 V_{she}$  for ECL = 60 cm. The practical implication of this dependence is that all cracks must eventually die (repassivate). Thus, if the ECP of the steel is  $0.1 V_{she}$  (typical of the non-irradiated core of an operating BWR), the crack is predicted to die when the ECL reaches about 2 cm, resulting in  $E_{crit}$  becoming equal to the ECP. Indeed, it is evident that death occurs at a shorter length the more negative is the ECP. For an ECP of the steel of  $0.2 V_{she}$ , the crack is not predicted to die until the ECL is greater than 60 cm, demonstrating that the critical ECL for crack death (repassivation) is very dependent on the prevailing ECP. This dependence of the CGR on ECL arises because of the IR potential drop down the length of the crack, due to the flow of the coupling current. This IR potential drop is subtracted from the driving force for the crack, which is  $ECP - E_{crack\ tip}$  resulting in the potential drop across the external surface that drives the cathodic reaction(s) being reduced. This results in a smaller throwing power of the CC from the crack mouth and hence to a lower CC and CGR. The authors know of

no other model for CGR that makes this important prediction, the consequences of which are discussed further below.

The CEFM predicts that the crack become acidified due to the hydrolysis of  $\text{Fe}^{2+}$ ,  $\text{Ni}^{2+}$ , and  $\text{Cr}^{3+}$  at the crack tip and that  $\text{Cl}^-$  is concentrated within the crack to a factor of up to  $10^6$  compared with  $[\text{Cl}^-]$  in the external environment while  $\text{Na}^+$  is rejected from the cavity [35]. The concentration factors increase with the ECP or more accurately with the magnitude of the coupling current, because  $\text{Cl}^-$  “climbs up” the potential gradient that drives the coupling current as it flows through the solution from the crack tip to the external environment. These are the expected consequences of the DAH.

The CGR is also predicted to be a function of coolant flow rate [23]. For a high aspect ratio crack (high crack length/COD), in which flow-induced mixing between the crack internal environment and the external environment is geometrically inhibited, the CEFM predicts that the CGR increases with increasing flow rate, corresponding to the positive shift in the ECP as shown in Figure. As with the shift in the ECP, the increase in the CGR occurs because of enhanced supply of the cathodic depolarizers to the metal surface external to the crack resulting in a greater CC and hence CGR. In the case of a low aspect crack, mixing of the crack internal and external environments destroys the aggressive conditions of high  $[\text{Cl}^-]$  and low pH at the crack tip, which result from differential aeration and that are necessary to maintain the crack electrochemically active. Consequently, the dissolution rate at the crack tip decreases and hence so does the CC and the CGR. This is expected to be a significant issue in the nucleation of cracks, where nucleation often occurs at stress raisers, such as corrosion pits, but this subject is beyond the scope of the current chapter.

Because of space limitations, the following discussion concerns only Intergranular Stress Corrosion Cracking (IGSCC) in sensitized Type 304 SS in BWRs, Hydrogen Induced Cracking in PWR mill-annealed steam generator tubing, and an assessment of the likelihood of IGSCC in the ITER. However, we note that the principles underlying these examples are common to all forms of corrosion, including general corrosion (GC), pitting corrosion (PC), crevice corrosion (CC), and corrosion fatigue (CF).

#### 4. The Critical Potential

It is evident from this discussion that the key parameters in determining the susceptibility of a reactor coolant circuit to corrosion-induced damage are the critical potential ( $E_{crit}$ ) and the ECP, such that when  $\text{ECP} > E_{crit}$ , PC, SCC (IGSCC), and CF may occur in the PHTS structural materials. In the case of HIC, the opposite applies, i.e.,  $\text{ECP} < E_{crit}$ . As also noted, both ECP and  $E_{crit}$  are functions of other variables, notably temperature, as shown in Figure 11 for sensitized Type 304 SS in dilute (0.01 M) NaCl solution at temperatures between 100 °C and 250 °C [6,38,39]. The reader will note that the solid line demarcates regions of ductile failure (no SCC) and regions of PC/IGSCC, as determined using constant extension rate tests (CERTs) under potential control. Extrapolation of that line to 25 °C yields  $E_{crit} = 0.17 \text{ V}_{\text{she}}$  and to 288 °C,  $E_{crit} = -0.52 \text{ V}_{\text{she}}$ . This latter value is significantly more negative than the  $-0.23 \text{ V}_{\text{she}}$  sanctioned by the NRC for IGSCC in sensitized Type 304 SS in BWR coolant. Noting that crack initiation must begin with passivity breakdown, for whatever reason (e.g., pitting, surface slip, grain boundary penetration), part of the difference may be attributed to the impact of  $[\text{Cl}^-]$  on the passivity breakdown potential at which pitting occurs, which coincides with  $E_{crit}$  for IGSCC at  $T < 120 \text{ °C}$  (Figure 11).

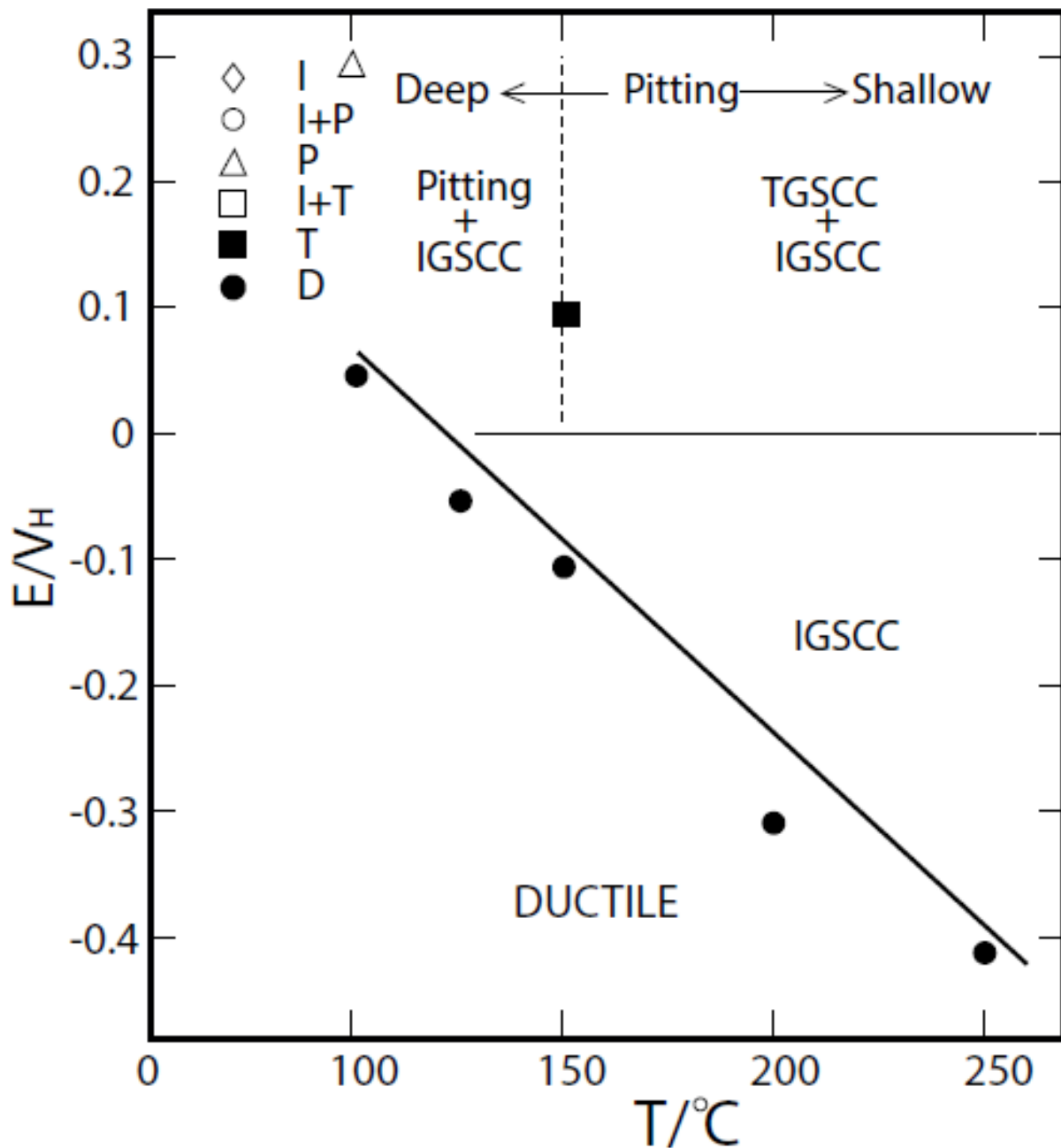


**Figure 11.** Values for  $E_{crit}$  for sensitized Type 304 SS in 0.01 m NaCl solution as a function of temperature as reported by Lin, et al. [38].

To a very good approximation, a correction to the data in Figure 11 can be made by using the Point Defect Model (PDM) [13] for the difference in chloride concentration [10 ppb ( $3.5 \times 10^{-4}$  m) for BWR coolant vs. 0.01 m in the experiments (Figure 11)].

$$E_{crit} = E_b^0 - \frac{2.303RT}{\alpha F} \log(a_{Cl^-}) \quad (17)$$

where  $E_b^0$  is the standard breakdown potential,  $\alpha$  is the polarizability of the barrier layer/solution (bl/s) interface, and  $a_{Cl^-}$  is the activity (concentration, for our purposes) of

chloride. The correction needed to bring the data plotted in Figure 11 (0.01 m NaCl) into compliance with BWR conditions ( $3.5 \times 10^{-4}$  m NaCl) at any given temperature is given as:

$$E_{crit}^{0.01} - E_{crit}^{PB} = -\frac{2.303RT}{\alpha F} \log\left(\frac{0.01}{3.5 \times 10^{-4}}\right) \quad (18)$$

or

$$E_{crit}^{PB} = E_{crit}^{0.01} + \frac{3.353RT}{\alpha F} \quad (19)$$

where the critical potential is designated  $E_{crit}^{PB}$ . Note that  $E_b^0$  is a function of temperature but not of  $[Cl^-]$ . Using parameter values for a stainless steel ( $\alpha = 0.8$  [14]), Equation (19) is evaluated at various temperatures, as listed in Table 2 (Row 3), along with the ECP for Type 304 SS in BWR coolant with 200 ppb  $O_2$  (Row 5). The corrected critical potentials are in reasonable agreement with the value of  $-0.23 V_{she}$  determined in an operating BWR [9] as sanctioned by the NRC. Unfortunately, there are no data for  $E_{crit}$  for IGSCC that have been measured for BWR coolant conditions at other temperatures with which to compare. We also note that the CERT test method tends to “overshoot” the true critical potential, particularly if the reciprocal of the passivity breakdown induction time is small compared with the strain rate employed in the experiment. Accordingly, the true critical potential is likely to be even more negative than those listed in Rows 1 and 3, Table 2.

**Table 2.** Estimated critical potentials for IGSCC for sensitized austenitic stainless steels as a function of temperature.

Parameter/T °C	25	50	100	150	200	250	288	300
$E_{crit}^{0.01}/V_{she}$	0.16	0.13	0.05	-0.09	-0.25	-0.40	-0.52	-0.67
$E_{crit}^{PB} - E_{crit}^{0.01}/V_{she}$	0.108	0.116	0.135	0.153	0.171	0.189	0.203	0.207
$E_{crit}^{PB}/V_{she}$	0.268	0.246	0.185	0.063	-0.079	-0.211	-0.317	-0.463
$E_{crit}^{CGR}/V_{she}$ , Expt							-0.230 [9]	
$E_{crit}^{CC}/V_{she}$	-0.086	-0.108	-0.138	-0.170	-0.190	-0.195	-0.200	-0.342
ECP (0.2 ppm $O_2$ )/ $V_{she}$	0.118	0.134	0.140	0.119	0.074	0.010	-0.056	-0.070

A alternate strategy exists for estimating the critical potential and that is based on the concept that a minimum coupling current (CC) is required to maintain the conditions at the crack tip sufficiently aggressive (low pH, high  $[Cl^-]$ ) to maintain the steel at the crack tip in the active state. Based upon extensive modeling work and upon experiment [26], for sensitized Type 304 SS, the critical CC for a standard crack (see below) is estimated to be 1 nA. Thus, since the CC depends upon the ECP, the critical potential ( $E_{crit}^{CC}$ ) corresponds to that ECP at which the CC = 1 nA. Values for  $E_{crit}^{CC}$  are presented in Table 2 as a function of temperature (Row 5).

The value of  $E_{crit}^{CGR}$  at 288 °C ( $-0.317 V_{she}$ ) may be compared with that measured by Indig and Nelson [9] ( $-0.23 V_{she}$ , Row 4, Table 2). However, each order of magnitude decrease in  $[Cl^-]$  (e.g., from the assumed 10 ppb to 1 ppb) results in a 0.342 V shift in the correction term ( $E_{crit}^{BWR} - E_{crit}^{0.01}$ ) shown in Table 2, increasing the critical potential to  $0.025 V_{she}$ . This suggests that  $E_{crit}$  is also a function of  $[Cl^-]$ ; a relationship that has not been previously detected (or looked for, to our knowledge), but which is understandable if the critical potential is determined by passivity breakdown, as is assumed in the present analysis in determining  $E_{crit}^{PB}$  [13]. In that case,  $E_{crit}^{PB}$  will shift in the negative direction by  $2.303RT/\alpha F$  with each decade increase in the chloride activity (concentration), where  $\alpha$  is the polarizability of the barrier oxide layer/solution interface. The shift is typically 100 mV/decade in  $[Cl^-]$ . It is important to note, however, that the sensitivity to chloride activity and other factors (metallurgical, mechanical, geometric, and environmental) indicates that the critical potentials (both  $E_{crit}^{CGR}$  and  $E_{crit}^{CC}$ ) are no more accurate than  $\pm 0.15$  V. Although there are not many experimental data available for the critical potentials for IGSCC in sensitized austenitic stainless steels, those that were available in 1981 are reviewed by

Cragolino and Macdonald [6]. These data mostly refer to 0.01 M NaCl solutions (c.f., Figure 11) but some data for sulfate and borate solutions may be gleaned from the review. The data are generally in accordance with those summarized in Table 2. Designating the critical potential at which the environmentally assisted CGR as  $E_{crit}^{CGR}$ , the data in Figure 10 reveals a dependence of  $E_{crit}^{CGR}/V_{she}$  on ECL that is greater than the difference between the calculated and measured  $E_{crit}$  values. Additionally,  $E_{crit}$  has long been suspected of also being a function of the degree of sensitization (DoS) of the alloy and of the conductivity of the solution [23]. Accordingly, we conclude that the values of  $E_{crit}$  given in Table 2 as a function of temperature are quite realistic within the bounds of uncertainty, as discussed above, although we opine that  $E_{crit}^{CC}$  is possibly the most relevant to the initiation of IGSCC in the IBED-PHTS in the ITER.

As noted above, cracking in mill-annealed Alloy 600 also exhibits a critical potential; in this case for HIC. This potential has been measured in a typical PWR primary coolant by Totsuka and Smialowska [5] using the CERT technique as shown in Figure 12. Thus, in this case, HIC is induced for  $E_{crit} < -820 V_{she}$ . These data are used later in this review when Primary Water Stress Corrosion Cracking (PWSCC) of Alloy 600 steam generator tubes is discussed. Unfortunately,  $E_{crit}$  does not appear to have been measured at other temperatures, so that, at the current time our analysis of this problem is restricted to PWR full power operating conditions.

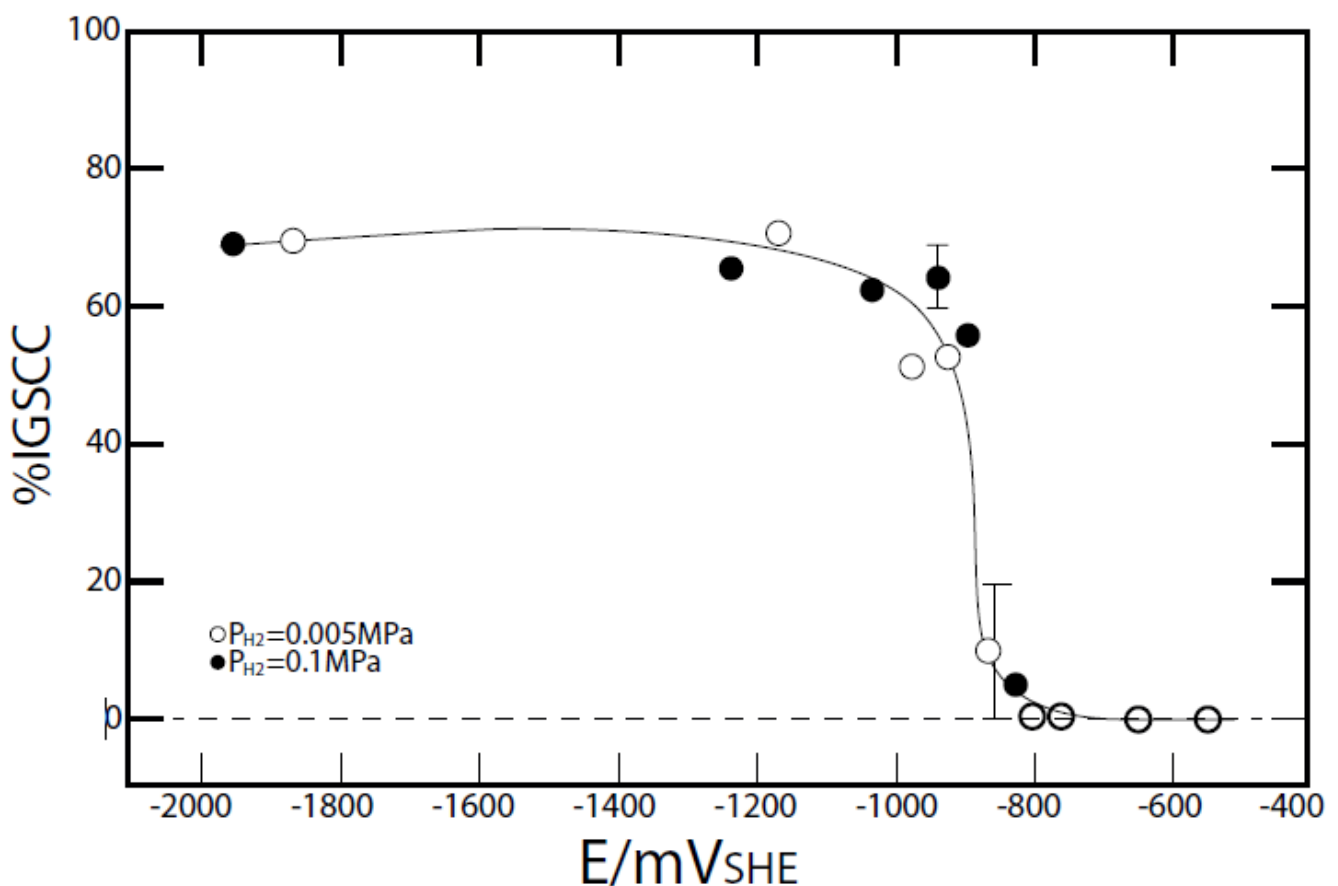


Figure 12. Effect of potential on the IGSCC of Alloy 600 in simulated PWR primary coolant at 350 °C [5].

## 5. Boiling Water Reactors (BWRs)

### 5.1. The Anatomy of a BWR

Boiling Water Reactors were developed in the USA primarily by the General Electric Co. from the naval reactor program in the 1950s/60s. Currently, there are 31 BWRs and 63 PWRs operating in the USA for a total of 94 nuclear power plants in the country although

this number is reducing as plants are retired from service and few new plants are being built. The reactor is a direct steam cycle system that does not involve heat exchange between a primary circuit and a secondary circuit, as in the case of a PWR (see below). In essence, it is a conventional thermal (fossil fueled) power plant with a ‘different heat source’ (a nuclear core vs. a furnace).

A simplified BWR coolant circuit is shown in Figure 13 [40]. Not shown are the other circuits, such as the decay heat removal circuit, reactor water cleanup system, reactor core isolation cooling circuit, standby liquid control system, and the high pressure and low-pressure emergency cooling systems. Briefly, water is boiled in the core and dry steam is sent to the turbines via the piping shown in the figure. The steam exiting the turbines is condensed, cleaned (deionized) via partial flow through the reactor water clean-up system, and returned to the feedwater of the reactor together with make-up water, as is necessary. The piping that flows through the recirculation pump is the recirculation piping system that recirculates liquid water from the upper core through the jet pumps and into the lower core plenum. This circuit contains liquid and is referred to as the “primary coolant circuit” to distinguish it from the steam phase circuit. The water from the lower plenum then flows up through the core where it boils to produce saturated steam exiting the core into the upper plenum, where it is dried and sent to the turbines. The system displayer in Figure 13 employs external recirculation pumps but BWRs in other countries, particularly in Europe, employ internal recirculation pumps.

A cutaway view of the core of a GE Model 6 BWR is presented in Figure 14. In this type of reactor, the neutron-absorbing control rods, which are used to control the core reactivity by absorbing neutrons, project into the core through the bottom of the reactor pressure vessel (RPV); when these rods are fully inserted, the population of thermalized neutrons is such (low) that a chain reaction can no longer be maintained, and the reactor shuts down. Although other means are available for shutting down the reactor in an emergency, such as flooding the core with borated water ( $^{11}\text{B}_5 + ^1_0\text{n} \rightarrow ^7\text{Li}_3 + ^4\text{He}_2$ ) via the standby liquid control system, the control rods are used to control reactor power during normal operation.

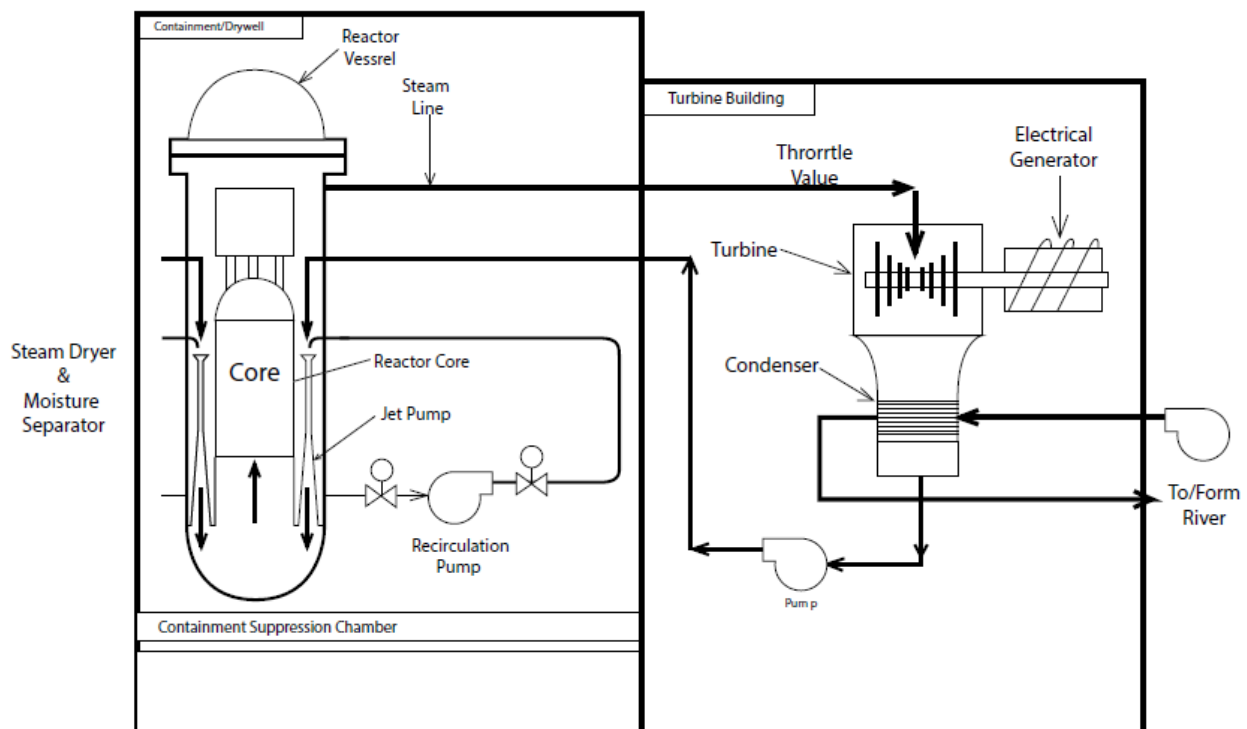


**Figure 13.** Simplified BWR coolant circuit showing the primary coolant circuit (blue line) and the steam (secondary) circuit (red line) [40].

Additionally, shown in this figure is the recirculation piping system that is external to the vessel and comprises an array of large diameter (e.g., 36-inch) and small diameter pipes and the main recirculation pump, which are external to the RPV in US plants. As noted above, some BWRs, notably those in Sweden, Switzerland, and Germany, employ coolant pumps that are housed within the RPV. Briefly, the water is taken from the bottom of the downcomer and is pumped into the nozzle of the jet pumps, which then draw water from the upper plenum and inject it into the lower plenum where it eventually enters the bottom of the core. The core itself is housed within a stainless-steel drum termed the “core shroud” (Figure 14). As indicated in Figure 14, the flow from the lower plenum bifurcates and approximately 10 % flows into the bypass, which is the gap between the inner RPV surface and the outer surface of the core shroud, with the remaining 90 % flowing into the core, where it boils to produce steam. The water in the bypass does not boil but it is subjected to  $\gamma$ - and n-induced radiolysis, albeit at a much lower dose rate than the water in the core.

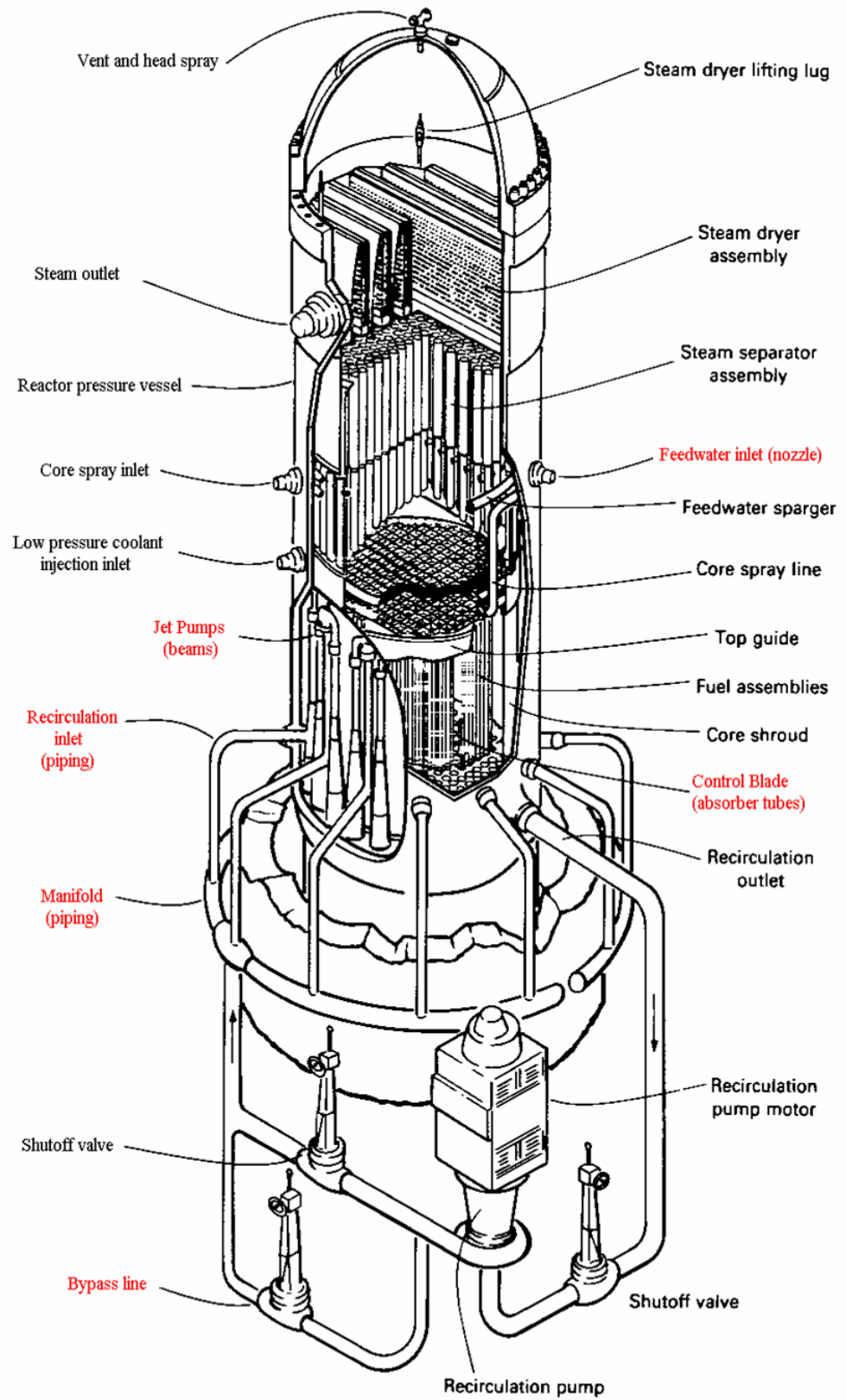
Figure 14 shows areas, labeled in red, in which IGSCC in weld-sensitized Type 304 SS has been observed in operating BWRs. This figure is a little out-of-date, as extensive cracking has also been observed in the core shroud, for example, in the region of the H3 weld towards the top of the shroud, where the ECP is predicted to be high (see below). While cracking occurred early on in BWR operation (1970s) in the recirculation piping system, and was attributed to weld sensitization, as it appeared in the heat-affected zones (HAZs) adjacent to field welds that are not easily solution annealed, eventually it spread to the RPV internal components (1980s, 90s, and 2000s). Cracking in the internal components also appeared in weld HAZs, but a contributing factor is irradiation-assisted stress corrosion cracking (IASCC), resulting from irradiation of the steel with high energy ( $> 1$  MeV) neutrons [41,42], which induces a state that is sometimes referred to as “irradiation-induced sensitization”. IASCC becomes a major factor for neutron fluences above  $10^{21}$  n/cm<sup>2</sup>. This phenomenon is restricted to high neutron flux areas in the reactor core.

A schematic of the flow path of the PHTS in a BWR is displayed in Figure 15.

The reader will note that the flow bifurcates in three places in the flow path (Figure 15b): at the top of the core where dry steam is sent to the turbines; at the mixing plenum where the flow of liquid water is divided into components that go through the recirculation system and a component that flows directly to the lower plenum; and in the lower plenum, where the flow is divided between the core bypass and the core.

In the initial code developed in Macdonald’s group [1,18,19,21,22,43–50], DAMAGE PREDICTOR, the radiolysis code of Burns and Moore [18,43–45] was adopted with the addition of the thermal decomposition of H<sub>2</sub>O<sub>2</sub> (Reaction 30 [50–53]). Since the decomposition of H<sub>2</sub>O<sub>2</sub> decreases [H<sub>2</sub>O<sub>2</sub>] but increases [O<sub>2</sub>] (H<sub>2</sub>O<sub>2</sub> → 1/2O<sub>2</sub> + H<sub>2</sub>O), the rate of this reaction, which occurs principally in the recirculation system, because of the long residence time compared with other components in the flow path, has a large impact on the ECP. Accordingly, the rate constant was varied to calibrate the model on plant [O<sub>2</sub>] and data from Dresden-2, but the value adopted was restricted to the range of values reported in the literature [52–56]. From then on, the value was not changed when modeling the electrochemistry of some of the reactors that spanned the BWR fleet in their response to hydrogen water chemistry (HWC).

Finally, it is important to note that BWRs differ in two important respects with regard to understanding the electrochemistry of the coolant: (1) the fraction of the coolant passing through the core vs. that passing through the bypass; and (2) the residence time that the coolant has in the downcomer, where much of the recombination of radiolysis products is believed to occur. This latter issue will be highlighted later in this paper.



Key Components of the BWR. The parts names in red indicates areas of IGSCC.

Figure 14. Cutaway view of the internals of the RPV of a Model 6 BWR [40].

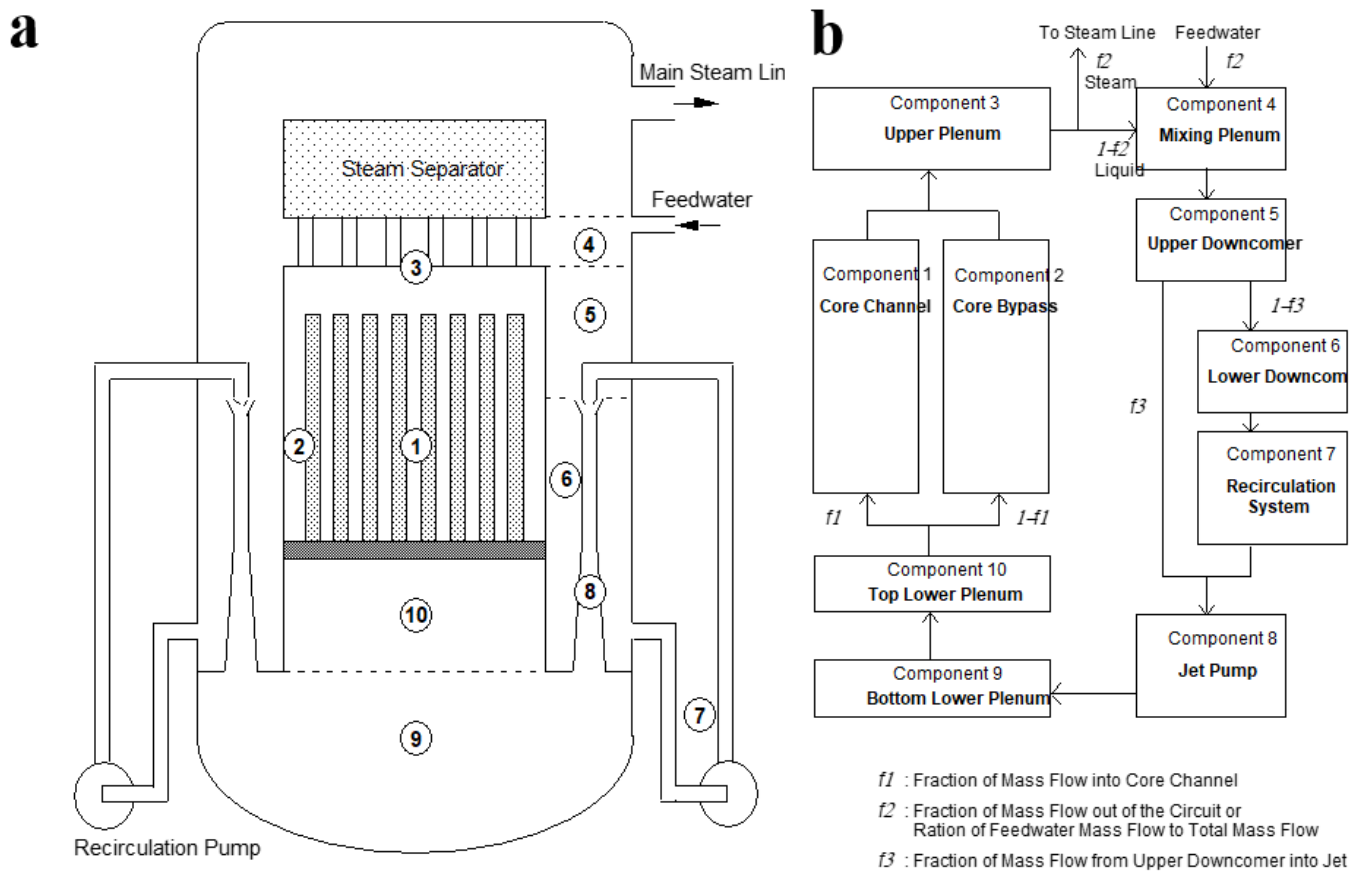


**Figure 15.** (a) Schematic of the PHTS of a BWR. (b) Schematic of primary coolant flow path. The regions are: (1) core channels; (2) core bypass; (3) upper plenum; (4) mixing plenum; (5) upper downcomer; (6) lower downcomer; (7) recirculation system; (8) jet pump; (9) lower plenum; (10) core entrance [22].

### 5.2. Radiolysis/ECP/CGR Modeling of BWR PHTSs

Extensive modeling of the electrochemistry and corrosion behavior has been reported; most notably by Macdonald and co-workers in the US, Yeh et al. in Taiwan, and Ibe, et al., and Ishigure and coworkers in Japan Ref. [1] and citations therein. These analyses all start with using a radiolysis/circuit flow model to calculate the concentrations of radiolysis species at closely spaced points around the PHTS but only the models of Macdonald et al. and Yeh and coworkers proceed to calculate the ECP and CGR of a “standard crack (typically 0.5 cm in length loaded to  $K_I = 27.5 \text{ MPa}\cdot\text{m}^{1/2}$ ) with a COD (crack opening displacement) of 0.0005 cm, a crack width of 1.27 cm, and having a Degree of Sensitization EPR (Electro Potentiokinetic Reactivation) value of  $15 \text{ C}/\text{cm}^2$ . Note that the models of these two groups have a common source [19]. Macdonald et al. [1,21] proceed further to calculate the integrated damage (crack length) as a function of the operating history of the reactor. This, more than anything else, renders the modeling of damage to a specific reactor, because reactors differ significantly in their operating histories. The radiolysis codes employed in these models are described in Part I [1] and in papers cited therein.

The concept of the “standard crack” was introduced in the analysis of BWR circuits [19] to allow the impact of the environment, through the ECP, temperature, flow velocity, and conductivity, on the tendency for the accumulation of IGSCC damage in sensitized stainless steel, so that different regions of a reactor coolant circuit could be compared. Because the CGR also depends on the stress intensity factor, which depends on the MCL (mechanical crack length) and on the ECL (electrochemical crack length) and on other mechanical/metallurgical/microstructural/microchemical factors, such as modulus, yield strength, grain size, and hardness, among others, a complete specification of the driving

force and predicted CGR for IGSCC is currently beyond SCC theory. Additionally, the prediction of the accumulation of SCC damage requires a viable model to predict the crack initiation time. While significant progress has been made toward that goal [14], a fully operational model is not yet at hand. Thus, we caution the reader to recognize these caveats when interpreting the calculated CGR data reported in this paper.

Briefly, the models of Macdonald et al. and Yeh and coworkers [1] have the general structure shown in Figure 16. The code accepts inputs of the thermal-hydraulic properties of the circuit (volume flow velocities, hydrodynamic diameter, temperature, as a function of operating power of the reactor), the initial plant conditions (e.g.,  $[O_2]$ ), and the  $\gamma$  and  $n$  dose rate profiles in the core as a function of elevation in the core channels. The code then proceeds to solve 13 tightly coupled, stiff first-order differential equations (one for each species) to yield the species concentrations around the circuit. These equations contain source terms for species radiolytic production and sink terms for reactions between various species in the system, as described in the radiolysis model, including the all-important thermal decomposition of  $H_2O_2$ . As noted previously, the rate constant for this reaction is used to calibrate the model on plant data (e.g., recirculation system  $[O_2]$ ), as shown in Figure 5 [21]. The species concentrations are then used to calculate the ECP and CGR for a model crack at closely spaced locations around the entire primary coolant circuit. The reader is referred to the literature [18,19,21,43–50] for a detailed description of the input and output files as they are too voluminous to include here.

A simplified thermal-hydraulic code, ZEBRA [57], was used to estimate the reactor thermal-hydraulic properties. The ZEBRA code is easier to use than the more sophisticated codes like the transient reactor analysis code 19 (TRAC-BD1 /MOD 1) [58,59]. ZEBRA was used to calculate the temperatures of the fuel cladding and coolant in the reactor core for specific plant data. The heat transfer coefficient and steam quality versus core height are also obtained from ZEBRA. The shortcoming of ZEBRA is that subcooled boiling is not considered, although homogeneous, two-phase flow is assumed in the algorithm. At the stage of development of DAMAGE-PREDICTOR in the early 1990s, ZEBRA was acceptable for performing the BWR core thermal-hydraulic analysis. Although the flow velocity and void fraction are not provided in the output of ZEBRA, they can be calculated using Bankoff's equation and mass balance, as described elsewhere [19].

Accurately simulating the neutron and gamma dose rates in the primary circuit, especially in the downcomer region, is of the utmost importance [19,46–50]. The decomposition of hydrogen peroxide and the radiolysis of water in the downcomer region have been determined to be important factors in determining the oxygen concentration in the recirculation line. The plant-specific dose rate profiles must be supplied for the PHTS of the plant to be analyzed, although neutron transport codes, such as DOT-III, may be employed for calculating the dose rate profiles to acceptable accuracy. In the current study, the dose rate data were obtained from [56].

DAMADE PREDICTOR, the initial code developed in Macdonald's group [19] in the early 1990s was calibrated against ECP data that had been measured in an autoclave valved into parallel with the recirculation piping system of the Dresden 2 BWR in Illinois. The data for  $[O_2]$  are summarized in Ref [19]. As noted elsewhere, the calibration involved changing the rate constant of the hydrogen peroxide thermal decomposition reaction ( $H_2O_2 \rightarrow H_2O + \frac{1}{2}O_2$ ) with an increase of the rate constant increasing  $[O_2]$  in the recirculation system, until agreement was obtained between the measured and calculated  $[O_2]$  in the autoclave valved into the recirculation piping. Once that was done the rate constant was fixed and has never deeded to be changed when modeling the radiolysis in a total of 14 BWRs (including Duane Arnold, Dresden-2, Grand Gulf, Susquehanna, Hamaoka-2, Fermi-2, Riverbend, Perry in the US, Leibstadt in Switzerland, 2 in Spain, 1 in Taiwan, 1 in Mexico, and 1 in Germany).

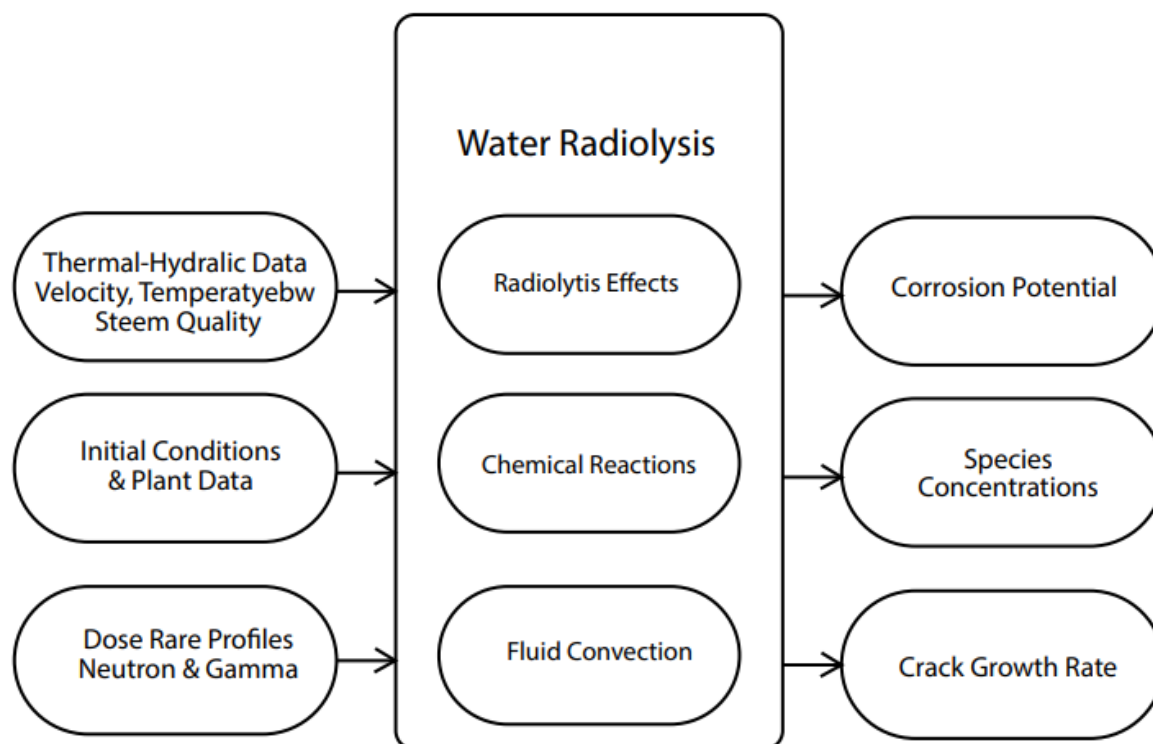


**Figure 16.** Schematic of the structure of the code DAMAGE PREDICTOR used for modeling the electrochemistry and corrosion behavior of the PHTS of a BWR [19].

The calibration on Dresden-2 is shown in Figure 17a, in which the calculated oxygen concentration is compared with the measured concentration in the recirculation system as a function of  $[H_2]_{FW}$ . As seen, good agreement is obtained demonstrating the procedure of modifying the rate constant for the thermal decomposition of  $H_2O_2$  is effective. Without changing in other parameters, including the rate constant for  $H_2O_2$  decomposition, the same comparison is shown for Duane Arnold in Figure 17b. Again, excellent agreement is obtained. In both cases, the lower limit of  $[O_2]$  corresponds to the detection limit (1 ppb) of the oxygen measuring technique. The true  $[O_2]$  for high  $[H_2]_{FW}$  is orders of magnitude lower than indicated in the plots.

The two reactors, Dresden-2 and Duane Arnold are at the low and high extremes of the US BWR fleet, respectively, with respect to their response to HWC, as measured by the ECP in the recirculation piping autoclave. Thus, as shown in Figure 17a, about 1.3 ppm of  $H_2$  is required to “suppress radiolysis” as judged by  $[O_2]$  in the case of Dresden-2, whereas a little over 0.2 ppm is sufficient to achieve the same condition in Duane Arnold (Figure 17b). Accordingly, Duane Arnold is much more sensitive to HWC than is Dresden-2. The difference has been traced to the residence time of the coolant in the downcomer where radiolysis-catalyzed recombination between  $O_2$  and  $H_2$  occurs with the recombination being more effective in the case of Duane Arnold, with its larger residence time in the downcomer than in the case of Dresden-2, which has a shorter residence time, but other factors may also be at play.

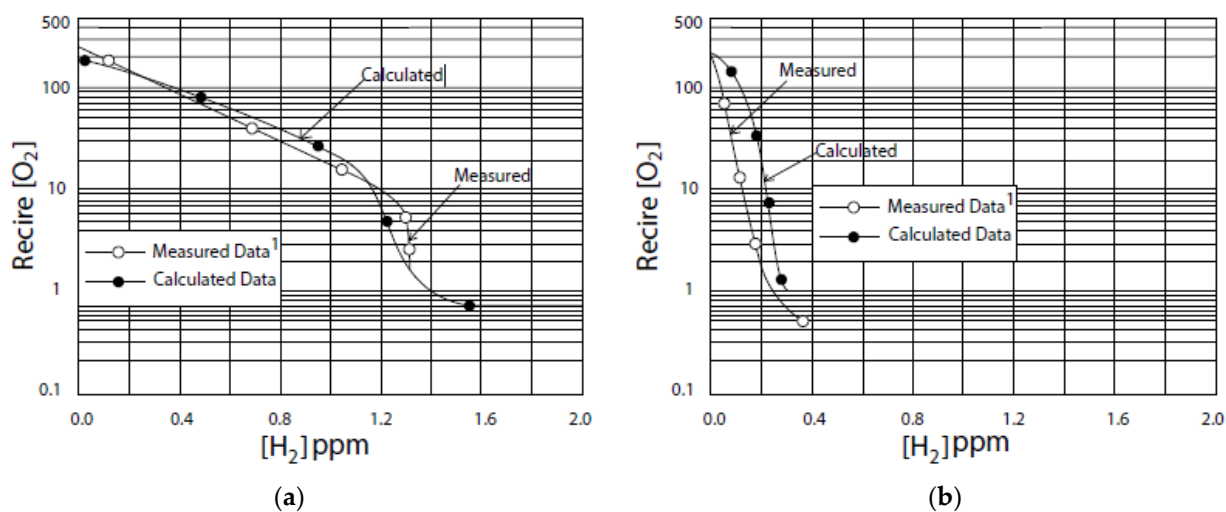


**Figure 17.** Comparison of measured [O<sub>2</sub>] in the recirculation piping autoclave with data calculated via DAMAGE PREDICTOR, (a) Dresden-2 and (b) Duane Arnold [19].

The accuracy with which [O<sub>2</sub>], [H<sub>2</sub>], and ECP can be calculated may be judged by the comparison of the calculated and measured values for these quantities in an autoclave valved into the recirculation piping in the Leibstadt BWR in Switzerland (Figure 18) [21]. One sees that the two sets of data agree very well, even though the exact hydrodynamic conditions in the autoclave were not known with certainty. Values for the measured [O<sub>2</sub>] of around 1 ppb reflect the detection limit of the measuring instrument and this limit was adopted for the calculated values even though the calculation yielded values for [O<sub>2</sub>] that are orders of magnitude lower than those indicated in Figure 18. As is evident from the discussion elsewhere in this review (Figure 4), oxygen levels below about 1 ppb have little impact on the ECP at the low Reynolds numbers that characterize low flow rate autoclaves.

In the late 1990s, DAMAGE PREDICTOR was upgraded successively into two more advanced codes named REMAIN and ALERT [60–64] and more recently to BWR\_Master [14]. These improved codes employ much more efficient and faster methods for solving the 13 simultaneous, stiff, first order differential equations for calculating the concentrations of radiolysis products around the PHTS and were specifically developed for BWRs that had internal coolant pumps, such as Leibstadt in Switzerland and the BWRs in Sweden and Germany. The calculated ECP around the PHTS of the Leibstadt BWR under NWC conditions ([H<sub>2</sub>]<sub>FW</sub> = 0) and HWC ([H<sub>2</sub>]<sub>FW</sub> = 1.2 ppm) is displayed in Figure 19a,b, respectively [21].

As seen, the ECP is predicted to vary significantly around the entire PHTS with the highest values being predicted for the regions experiencing the greatest radiolysis (core channels and upper plenum). An important finding was that no point in the PHTS had an ECP that was more negative than  $E_{crit} = -0.23 V_{she}$ , the value that had been sanctioned by the NRC as the critical potential for IGSCC in sensitized Type 304 SS. Thus, the entire PHTS in this reactor is in a spontaneous state of cracking and the most likely reason that crack was not more severe than had been observed is that the initiation time is very long and/or the stresses are lower than those used in defining the “standard crack”.

With the addition of 1.2 ppm of hydrogen to the feedwater, however, the ECP for many components is displaced below  $-0.23 V_{she}$ , as depicted in Figure 17b. Thus, much of the recirculation system, the bottom of the lower plenum, and the lower reaches of the downcomer are protected by this level of HWC, but the core channels, much of the core bypass, the upper and mixing plenums, the upper downcomer, the top of the lower downcomer, the entrance of the recirculation system, the jet pumps, and the top of the downcomer, and the top of the lower plenum are not be protected. This led one of the present authors (DDM) in 1992 to question the viability of HWC in protecting the PHTS of BWRs, particularly, the RPV internal components [10]; a question for which he was loudly criticized by a vendor but which, in retrospect, was justified. In particular, the subsequent,

extensive occurrence of IGSCC in the internal components of BWRs worldwide vindicated this position.

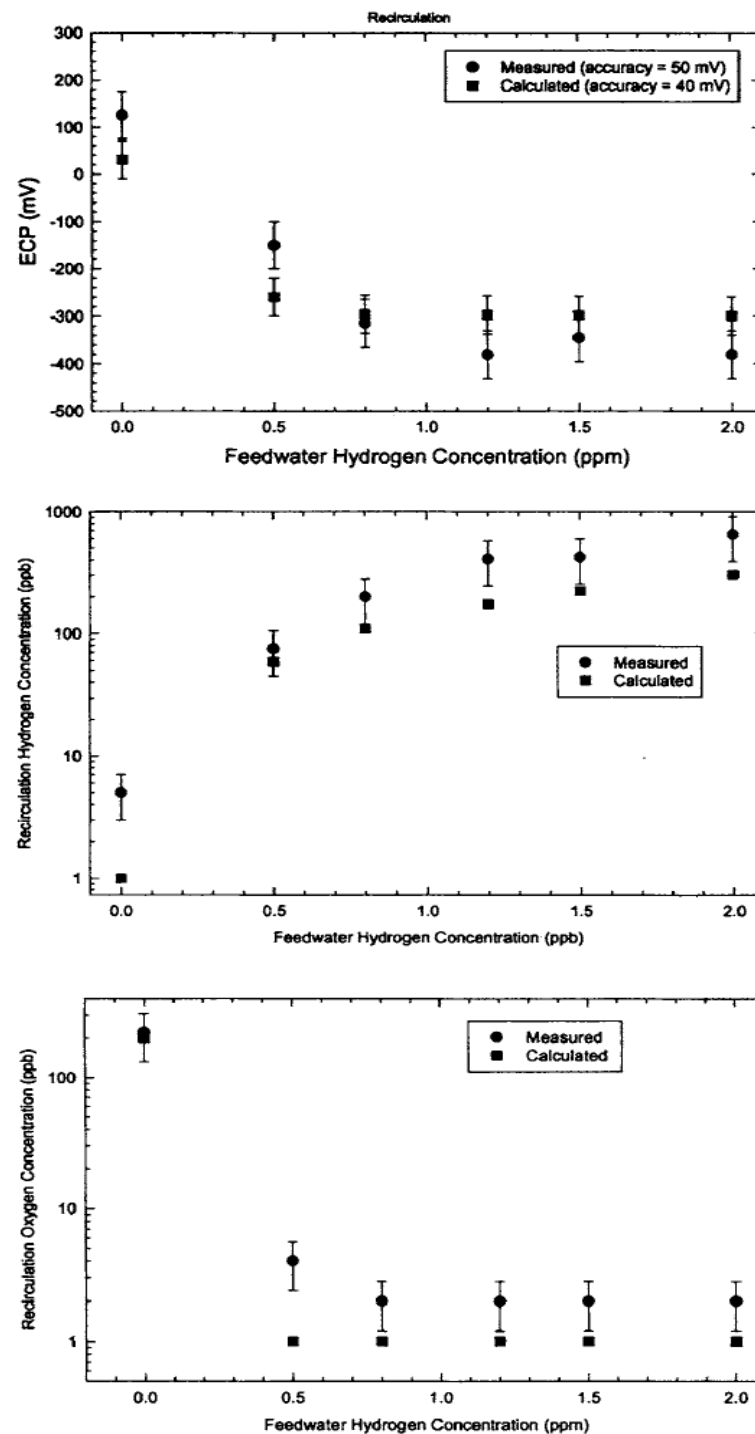
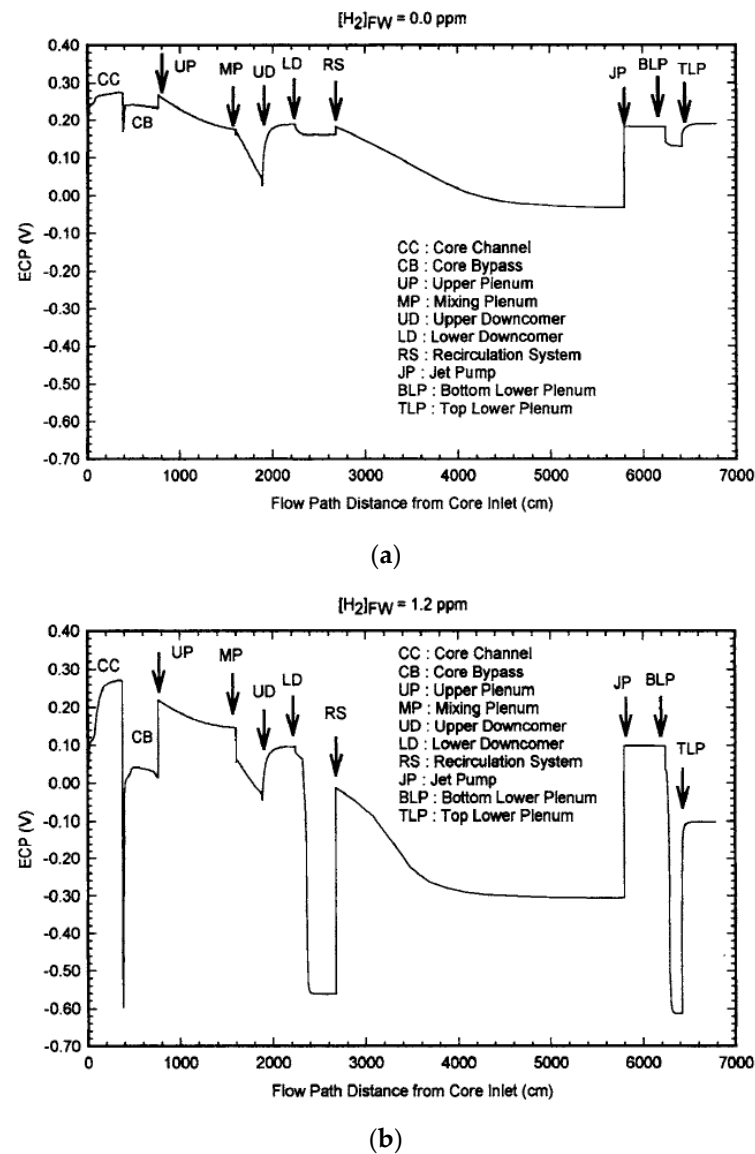
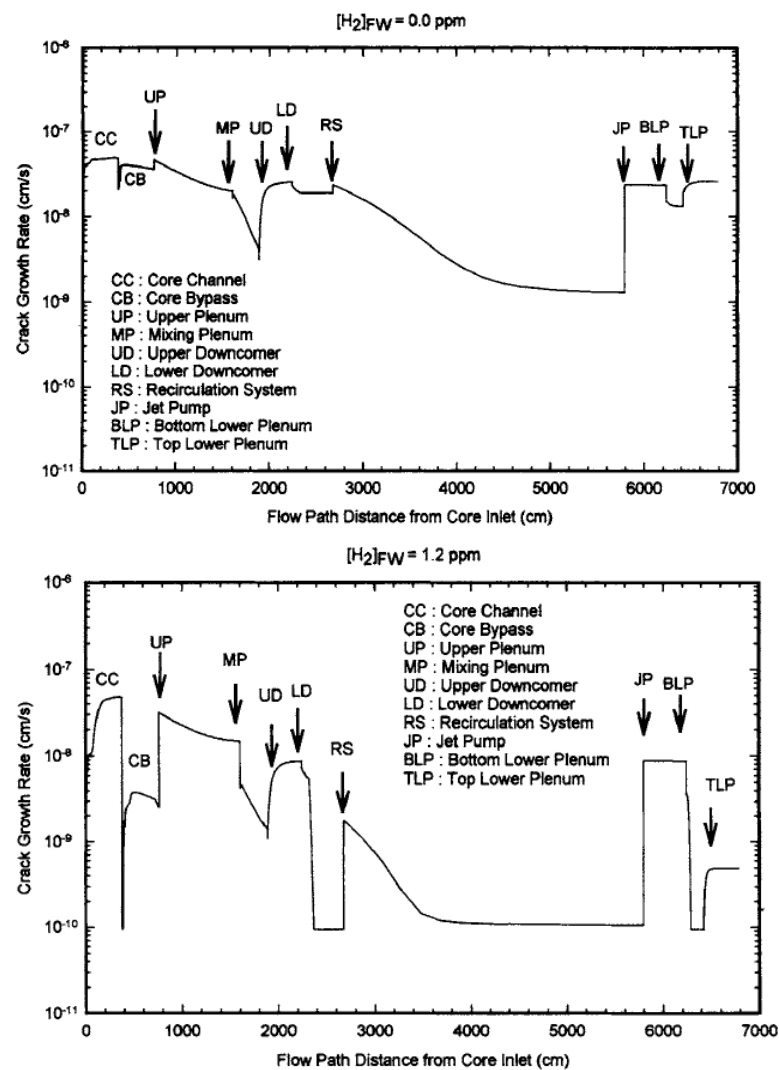


Figure 18. Comparison of calculated and measured ECP, [H<sub>2</sub>], and [O<sub>2</sub>] in the recirculation piping system from a double blind HWC mini test at the Leibstadt BWR in Switzerland [21].



**Figure 19.** Predicted ECP under NWC (a) and HWC (b) vs. flow path distance from the bottom of the core for the Leibstadt BWR in Switzerland [21].

Because of the exponential relationship between CGR and ECP, it is expected that the variation of  $\log(\text{CGR})$  for a 0.5 cm long standard crack loaded to a stress intensity factor of  $K_I = 27.5 \text{ MPa}\cdot\text{m}^{1/2}$  as a function of distance around the PHTS would mirror that of the ECP and this is found to be the case as shown by comparing Figures 19 and 20. A “standard crack” was defined, because, as we see above, the CGR is a function of the electrochemical crack length (ECL) at constant  $K_I$  and is a function of  $K_I$  for constant ECL. It is also a function of the degree of sensitization (DoS) of the steel as well as the neutron fluence (“Irradiation-Assisted Stress Corrosion Cracking”, IASCC) [41]. In an actual reactor, cracks may exist that possess wide ranges in ECL and  $K_I$  depending on when they nucleated (i.e., on the growth time), the local ECP and stress, so that it becomes an almost impossible task to fully and accurately describe the state of IGSCC in a reactor PHTS at any given moment without a major computational effort and a viable model for calculating the initiation time. The definition of a “standard crack” appears to be the best compromise.



**Figure 20.** Predicted CGR vs. flow path distance from the bottom of the core for 0 ppm H<sub>2</sub> (NWC) and 1.2 ppm H<sub>2</sub> (HWC) added to the feedwater of the Leibstadt BWR in Switzerland [21].

The importance of the effect of ECL on the prediction of CGR is illustrated in Figure 21 for crack adjacent to the H3 weld in a BWR core shroud. Thus, if no dependence of CGR on ECL was recognized (the “linear” case), crack extension to 2.8 cm would have occurred in 24 months whereas it would take more than 120 months for the crack to extend to that depth if the impact of the ECL on CGR is recognized, as in the case of the CEFM [23]. In other words, a model that did not recognize the dependence of the CGR on the ECL would greatly over predict the rate of damage accumulation and possibly trigger further inspection and unscheduled maintenance when, in fact, none was called for.

In the early 2000s, REMAIN was upgraded ALERT to predict the accumulated IGSCC damage (crack length) for cracks at specified locations. This required knowledge of (and an input files for) the operating history of the reactor in addition to the reactor specific parameters (geometry and thermal hydrodynamics of the PHTS, dose rate profiles, etc) that had been required previously. The new code, ALERT, represents a powerful predictive code, because it allowed, for the first time, to forge a link between plant operation and accumulated damage for a crack in a specified location in the PHTS. An example of such a calculation for a reactor operating in Taiwan is shown in Figure 22 [62]. Three scenarios were explored for a crack in the HAZ of the H3 weld in the outside surface of the core shroud; normal water chemistry (NWC), full Hydrogen Water Chemistry (1 ppm [H<sub>2</sub>]<sub>FW</sub>), both for 10 years; and a combined protocol of 5 years of NWC followed by 5 years on HWC,

as shown in the figure. As seen, the crack extends from an assumed initial length of 0.5 cm under NWC over 10 years but under HWC, the crack extends to only 1.1 cm over the same period. If the reactor operates on NWC for the first 5 years, the crack extends to 2.1 cm, but when operating on HWC for the remaining 5-year period, the crack extends further by only about 0.1 cm to 2.2 cm. There are several lessons to be learned from this simulation of IGSCC damage in BWRs: (1) the curves show that, as time proceeds, the CGR (the slope of the curve) decreases, corresponding to the impact of crack length on the CGR (see Figure 10); (2) The benefits to be obtained by switching from NWC to HWC is governed by the “law of decreasing returns”, in that the cost of operating on NWC for the first year in terms of crack extension is 1.6 cm whereas switching to HWC saves only 0.6 cm in crack extension. This, the operator would have to decide whether the cost of installing and maintaining large amounts of hydrogen on site, as well as the increased man-REM cost due to the transfer of radioactive nitrogen in the form of ammonia to the turbines, is worth the effort. Finally, the ECP at this location is about  $0.15 V_{she}$ , well above the critical potential for IGSCC in sensitized Type 304 SS of  $-0.23 V_{she}$ , so that the benefits of operating on HWC are evident, in terms of a reduction in ECP and hence in CGR, even though full protection is not achieved.

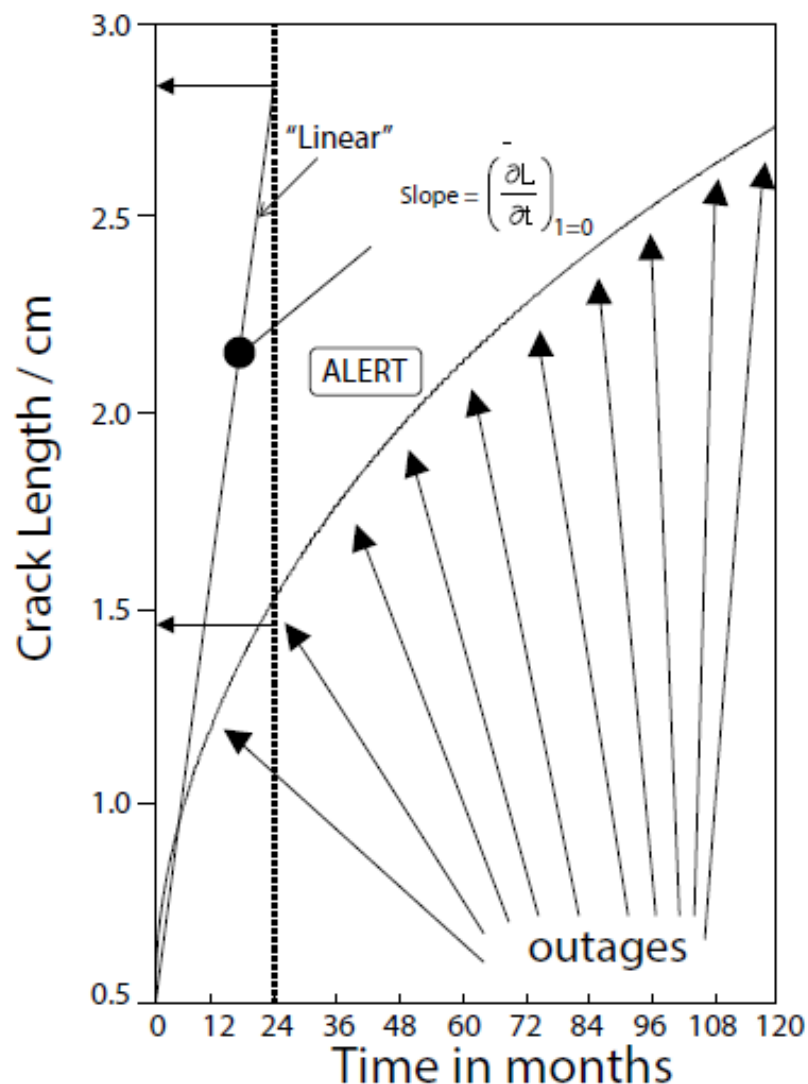


**Figure 21.** Illustration of the non-linearity of accumulated damage (crack length) and the inadequacy of a linear crack growth model for extrapolating crack accumulation rate (CGR) data to longer times and greater crack lengths [61,62].

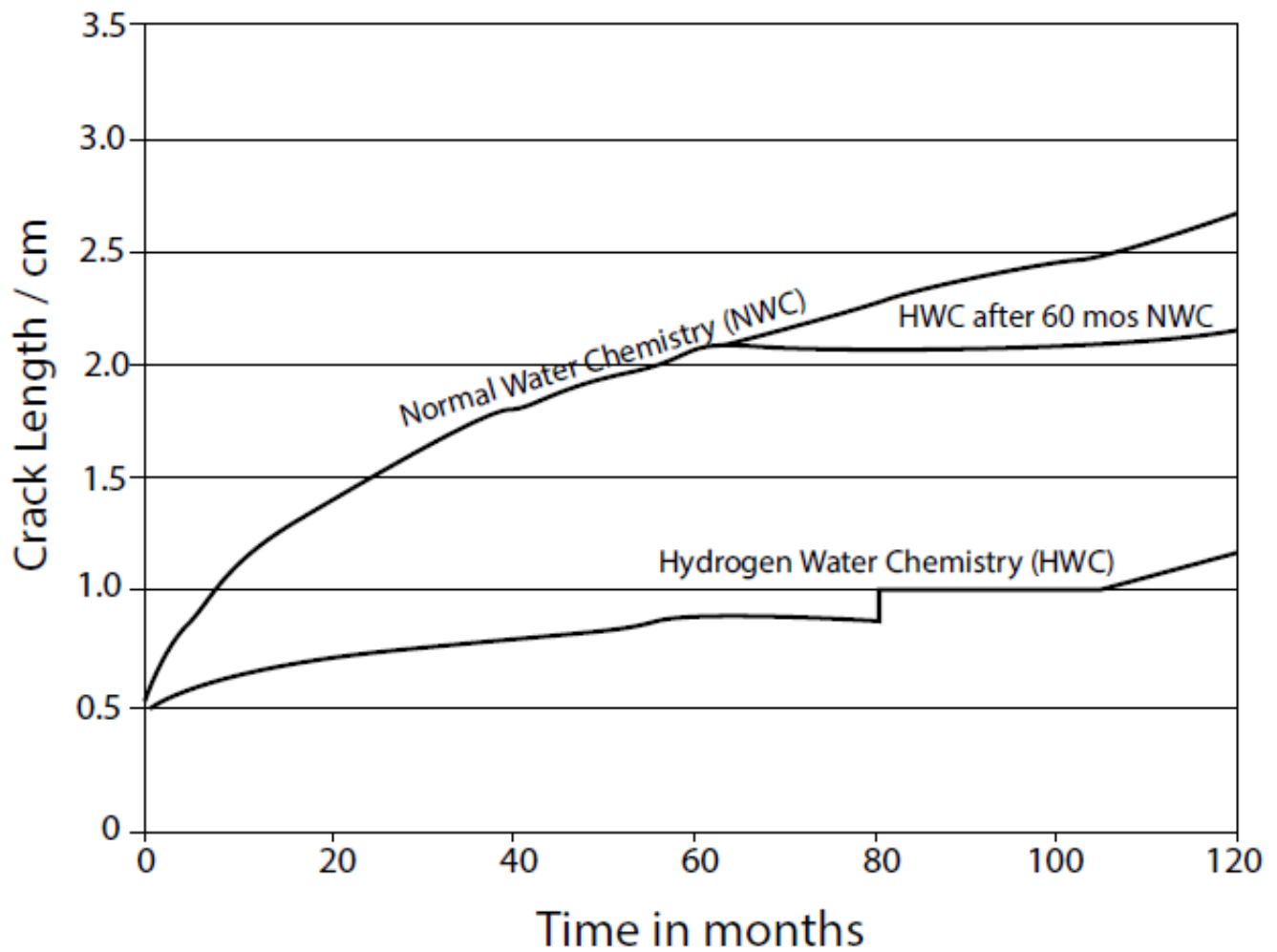


**Figure 22.** Predicted accumulated IGSCC damage due to a crack adjacent to the HAZ of the H3 weld in the core shroud of a BWR. Note that the discontinuities in the crack length arise from changes in the CGR during start-up and shut-down transients [62].

The discontinuities in the crack growth curves displayed in Figure 22 are due to power transients, including shutdowns and start-ups. These are responsible for a significant fraction of accumulated damage, as indicated in Figure 23. The calculations were performed assuming “hard” and “soft” restarts, corresponding to a rapid power ramp-up (1 h) and to a slow ramp-up (24 h), respectively. The simulations predict that the restart contributions to the accumulated damage after 10 years of operation are significantly greater when operating on HWC than when operating on NWC and that in each case hard restarts contribute about twice the damage as do soft restarts. However, when corrected to crack extension, the hard restart under NWC amounts to 0.102 cm under HWC and to 0.048 cm under NWC. The relatively poorer performance under HWC, in this regard, is attributed to the transients in temperature and conductivity that accompany start-ups and shutdowns that partially negate the benefits of HWC.

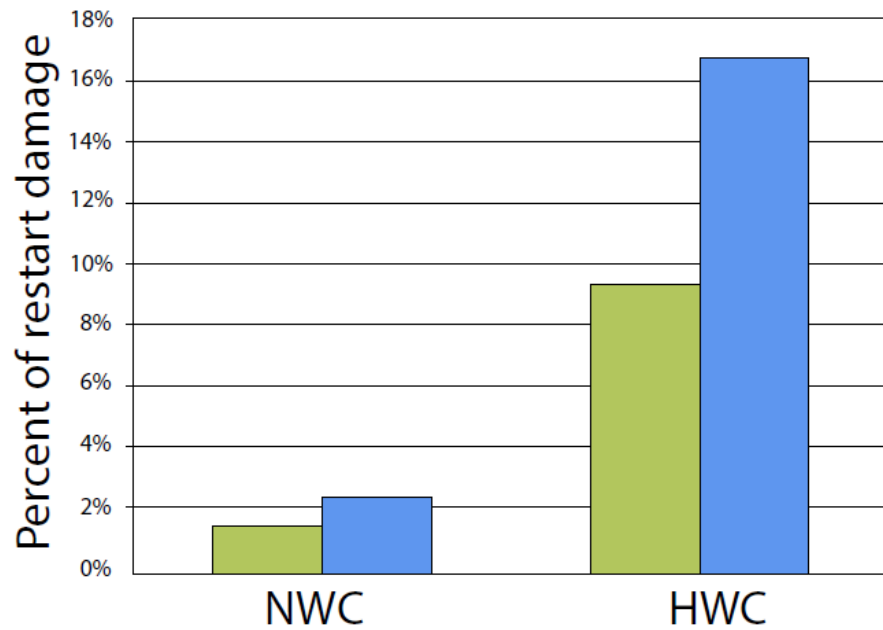


**Figure 23.** Predicted impact of water chemistry and restart/shutdown transients on the accumulated IGSCC damage due to a crack adjacent to the HAZ of the H3 weld in the core shroud of a BWR [62]. Green bars correspond to “soft” (24-h) restarts and blue bars to “hard” (1-h) restarts.

The reader may ask: “How accurate are these simulations?” An answer to that important question is provided in Figure 24.

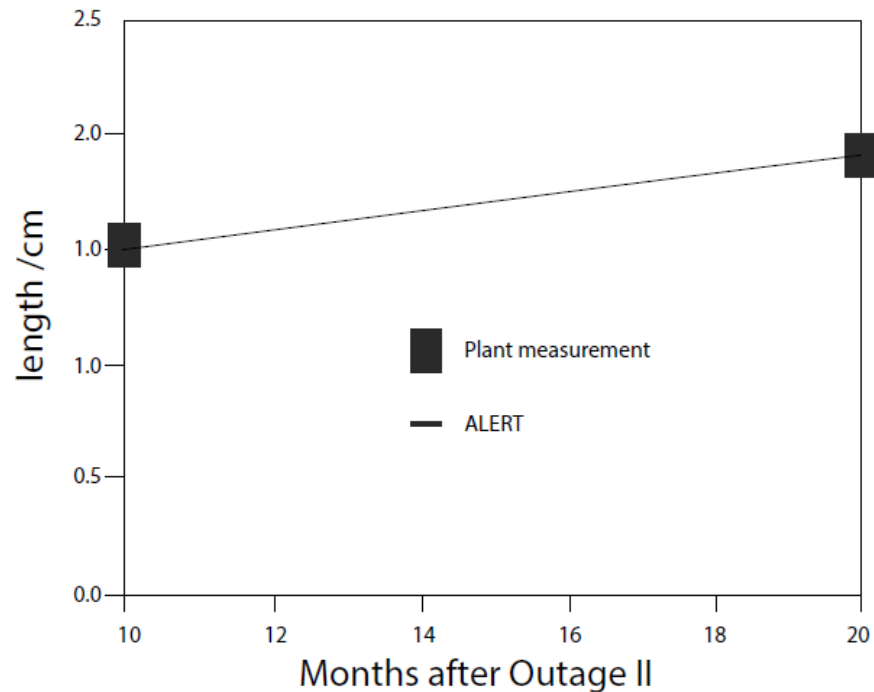


**Figure 24.** Comparison of predicted crack extension with plant observation over a ten-month period after Outage 11 in an operating BWR [21]. Note that the crack initiation time was adjusted so that the calculated data pass through the initial point. Accordingly, only the comparison after 10 months after Outage 11 has probative value [62].

In this figure, the initiation time of the crack was adjusted so that the curve passed through the crack depth measured at the beginning of operation after the 11-th outage

and the curve is then compared with the crack length measured twenty months later [62]. Thus, only the comparison at 10 months after Outage 11 has probative value. During that period, the crack was found to have grown about 0.3 cm, whereas ALERT predicted an extension of about 0.25 cm. Given that there was some uncertainty in the operating history and conditions of the reactor, we posit that the agreement is very good.

One important feature of the MPM and the CEFM is that the kinetics of the HER, OER, and HPER on the external surfaces that consume the coupling current and hence determine both the ECP and the CGR, may be manipulated to modify both the ECP and CGR in a manner that reduces the threat of IGSCC during reactor operation. The parameter of each of these reactions that is of interest in this regard is the exchange current density,  $i_{0,O/R}$ . This can be done by using a catalyst or an inhibitor the increase or decrease the exchange current density, respectively.

Numerous workers have commented on an apparent relationship between the CGR and the oxide on the external surface and the CEFM provides a theoretical explanation of that relationship. We show in Figure 25 the ALERT predictions for the case of the general catalysis of the HER, OER, and HPER by a factor of  $10^4$ ; that is, by multiplying the exchange current density for each reaction by that amount. Because under NWC conditions the environment is oxidizing in nature, due to low molecular weight hydrogen being preferentially stripped from the coolant by boiling in the core, the molar excess of  $O_2$  and  $H_2O_2$  are rendered more powerful as oxidizing agents by virtue of catalysis, which increases the exchange current densities for the reduction of both species by a factor of  $10^4$ . Recall that the ECP lies closest to the equilibrium potential of that partial process that has the greatest exchange current density, so that the ECP will move closer—in the positive direction- to  $E^{\circ}_{OER}$  or  $E^{\circ}_{HPER}$ , because the partial anodic process is not catalyzed and  $H_2$  is greatly reduced in the coolant due to boiling and hence contributes little to the ECP. As a result, the ECP is shifted in the positive direction [compare Figures 19a and 25a for the non-catalyzed and catalyzed cases, respectively] changes little around the circuit, because  $[O_2] + 1/2[H_2O_2]$  is essentially constant around the circuit. In the case of HWC ( $[H_2]_{FW} = 1$  ppm, however, hydrogen is now in molar excess in the out-of-core regions and, as the HER is also catalyzed (recall this is for general catalysis where all of the redox reactions are catalyzed to the same extent) hydrogen now becomes a much more powerful reducing agent, resulting in the displacement of the ECP to very negative values [Figure 25a compared with the NWC case ( $[H_2]_{FW} = 0$  ppm)]. In terms of the CGR, the value predicted for catalysis under NWC conditions [Figure 25b] is about  $8 \times 10^{-8}$  cm/s (2.52 cm/year) while under HWC, the crack growth rate for most of the PHTS is the creep limit of about  $1 \times 10^{-10}$  cm/s (31.5  $\mu$ m/year), except for the core, where rates as high as  $10^{-7}$  cm/s are predicted. This is the underlying basis of NobleChem [65], as developed by the General Electric Company, in which a noble metal (e.g., Pt) is electrolessly deposited on the PHTS surfaces with the goal of catalyzing the recombination of  $H_2$  with  $O_2$  and  $H_2O_2$ . While that may occur, from an electrochemical viewpoint, the principal effect is on enhancing the rates of the HER, OER, and HPER, as discussed above. The effectiveness of general catalysis is further illustrated in Figure 26 where the accumulated damage is plotted as a function of time over a 20-month operating period for a typical crack in a BWR under full-power conditions. We see that general catalysis effectively suppresses crack extension but only in the presence of excess hydrogen, reinforcing the conclusion drawn above. From the known impact of NobleChem in various reactors, as reported by Balachov, et al. [62], it is apparent that the level of catalysis achieved in a lot less than the  $10^4$  assumed in the above calculations, possibly only as much as 10, but that is sufficient to afford significant benefits to plants operating on HWC.

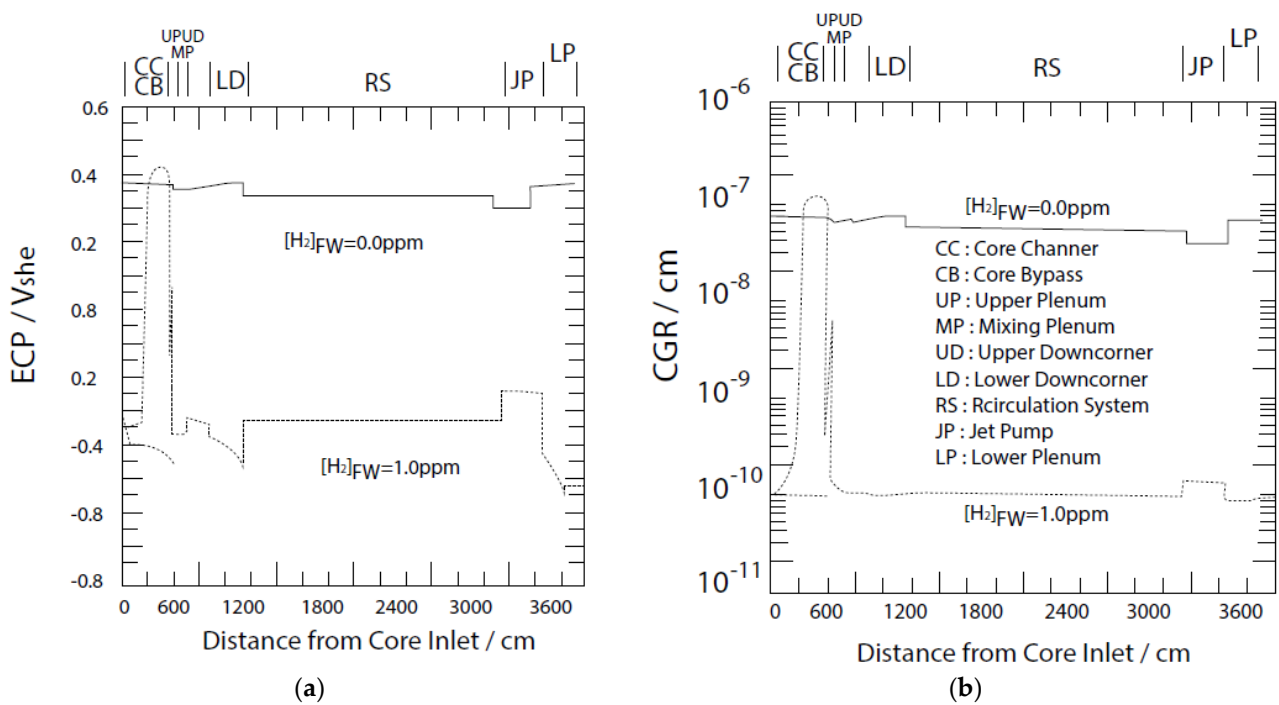


**Figure 25.** Predicted ECP (a) and CGR (b) in the PHTS of a BWR (Dresden-2) employing general catalysis (exchange current density multiplier of  $10^4$ ) under NWC ( $[H_2]_{FW} = 0$  ppm) and HWC ( $[H_2]_{FW} = 1.0$  ppm) [21,61–63].

Nevertheless, general catalysis raises an important issue. As seen from Figures 25 and 26, catalysis is only effective if the system has a stoichiometric excess of hydrogen in the coolant. If an excess of H<sub>2</sub> does not exist, then both the ECP and the CGR are elevated from their uncatalyzed values; this being due to the catalysis of the OER and the HPER over that of the HER. Thus, if a reactor that has been operating on HWC/NobleChem is forced for any reason to abandon HWC there exists the real possibility that it may experience enhanced rates of accumulated IGSCC damage when operating in the future under NWC. Thus, a method needs to be developed to de-catalyze the steel surfaces in the PHTS of BWRs.

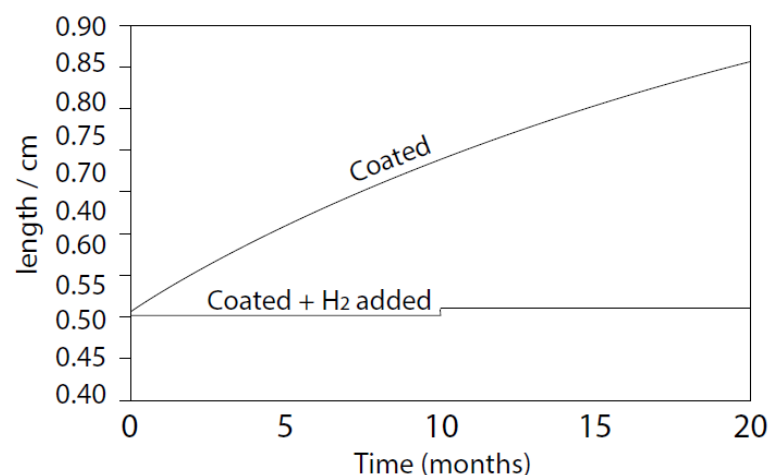


**Figure 26.** Predicted crack length vs. time for noble metal coated, sensitized Type 304 SS in BWR coolant (water at 288 °C) with and without a stoichiometric excess of hydrogen [62].

The codes predict that general inhibition might also be an effective method for inhibiting the development of IGSCC damage in BWRs [21]. In this case, the exchange current densities of the HER, OER, and HPER are reduced by a factor of  $10^{-4}$ . Predictions of this

effect for Dresden-2 are shown in Figure 27. The effect is predicted to be very significant as the ECP under both NWC ( $[H_2]_{FW} = 0$ ) and HWC ( $[H_2]_{FW} = 1.0$  ppm) are displaced in the negative direction for all components in the PHTS to values that is much lower than  $E_{crit}$ , except for the core, where the ECP is at the critical potential [Figure 27, left frame]. As expected, the CGR is decreased to the creep limit, indicating that IGSCC might be eliminated in the entire PHTS (Figure 27, right frame). Of great importance, is that general inhibition would eliminate the need for HWC entirely, freeing BWR owners and operators of the costs associated with installing hydrogen water chemistry in their reactors.

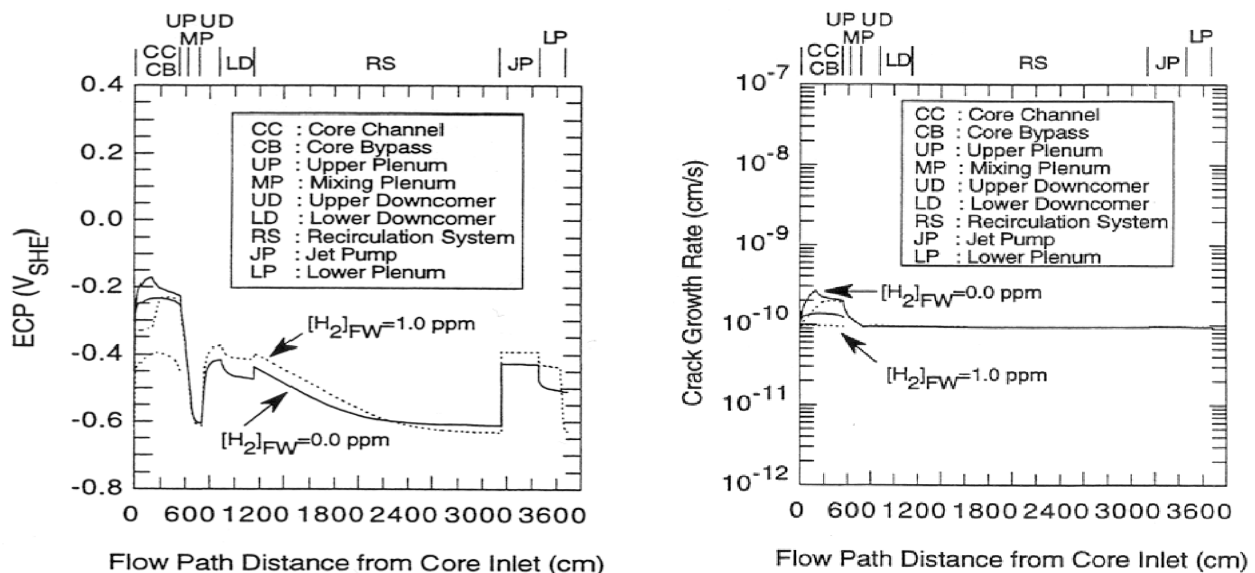


**Figure 27.** ECP and crack growth rate variations in the heat transport circuit of Dresden-2 employing general inhibition (exchange current density multiplier =  $10^{-4}$ ) under NWC ( $[H_2]_{FW} = 0.0$  ppm) and HWC ( $[H_2]_{FW} = 1.0$  ppm) [21].

General inhibition has been tested in the laboratory by daisy-chaining two bolt-loaded ( $K_I \approx 25 \text{ MPa}\cdot\text{m}^{1/2}$ ), pre-cracked CT specimens of sensitized Type 304 SS in an autoclave in simulated, conductive coolant containing  $0.005 \text{ M Na}_2\text{SO}_4$  at  $250^\circ\text{C}$  [64], as shown in Figure 28. The solution was sparged in the reservoir at  $22^\circ\text{C}$  with pure oxygen to yield a concentration of  $40 \text{ ppm}$  ( $1.25 \times 10^{-3} \text{ m}$ ).

One specimen was coated with an electrophoretically deposited  $\text{ZrO}_2$  coating that was cured at  $250^\circ\text{C}$  for 48 h to form a resilient ceramic coating. The crack lengths in both specimens were measured by compliance and the results are displayed in Figure 27. The quality of the coating was measured using electrochemical impedance spectroscopy (EIS) with a  $0.01 \text{ M Fe}(\text{CM})_6^{2-}/\text{Fe}(\text{CN})_6^{3-} + 0.1 \text{ M NaOH}$  fast redox couple before and after exposure to the high temperature aqueous environment to detect any changes in quality (porosity). It was found that the specific impedance ( $\text{ohm}\cdot\text{cm}^2$ ) was 100 to 1000 times higher for the coated than for the uncoated specimen.

The data shown in Figure 29a reveal that the  $\text{ZrO}_2$  coating displaces the ECP in the negative direction by  $400\text{--}500 \text{ mV}$  and completely suppresses IGSCC crack extension [Figure 29b] as predicted theoretically (Figure 27). Indeed, no crack growth was detected in the coated specimen, whereas the crack grew by nearly  $0.5 \text{ cm}$  over the 400 h exposure period for a CGR of about  $3.1 \times 10^{-7} \text{ cm/s}$ . This value reasonably agrees with the data plotted in Figure 9 for a temperature of  $250^\circ\text{C}$ . According to theory, for an increase in the specific impedance of the surface of a factor of 100 to 1000, due to the presence of the coating, the ECP should be displaced to  $-200 \text{ mV}_{\text{she}}$  to  $-350 \text{ mV}_{\text{she}}$ , in excellent agreement with experiment [Figure 29a] while the CGR should be displaced to the creep limit; again in good agreement with the CEFM. Not only do these experiments confirm the validity of the concept of general inhibition, but they provide a robust test against direct experiment of the MPM and the CEFM

for estimating ECP and IGSCC CGR in sensitized Type 304 SS, respectively, under realistically simulated reactor operating conditions. It seems that for this technique to become a practical IGSCC control method for use in operating BWRs, a method must be developed for coating the internal surfaces of the PHTS with a resilient, dielectric coating that can withstand the rigors of exposure to high temperature BWR coolant.

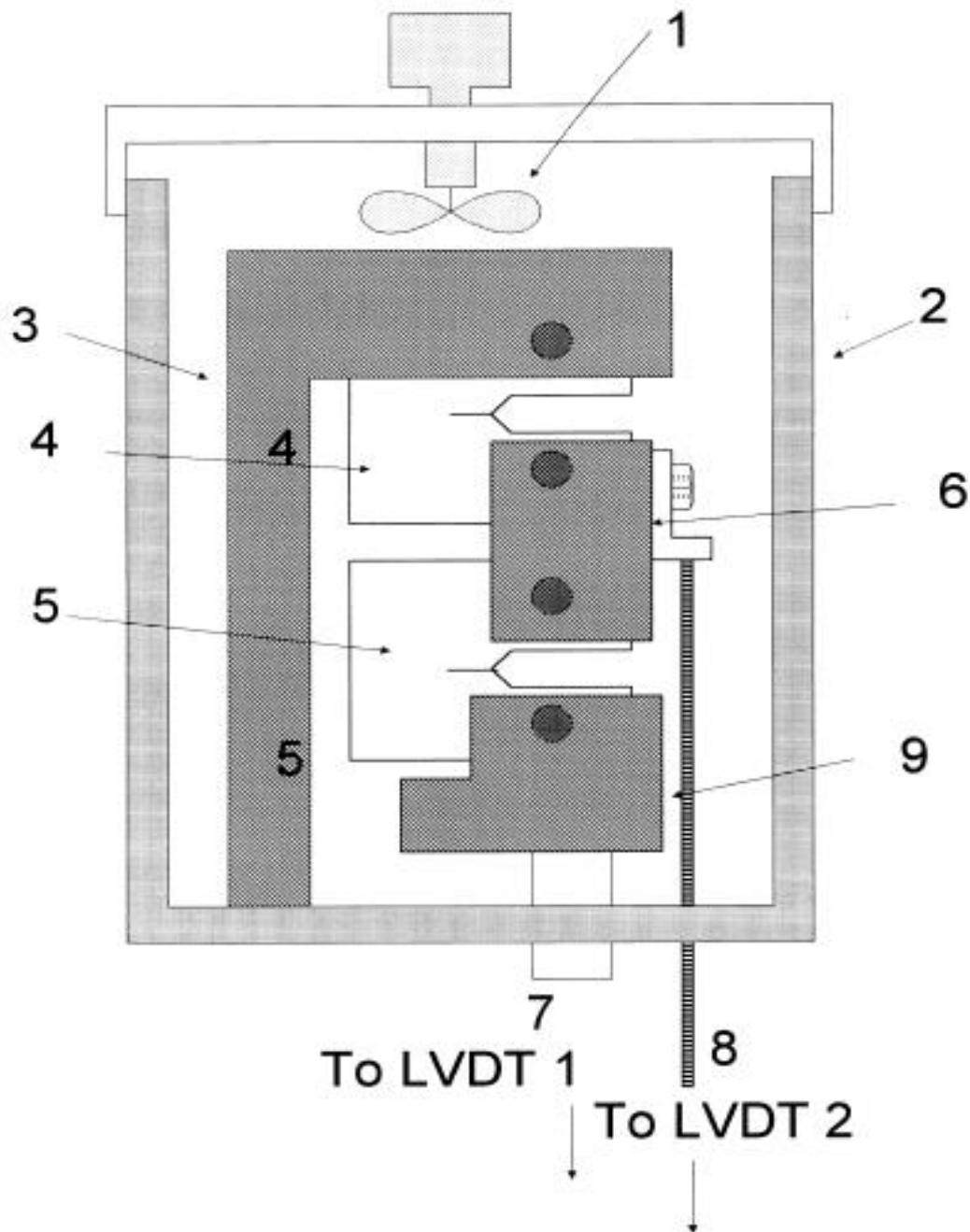


**Figure 28.** Schematic of daisy-chained C(T) specimens of sensitized Type 304 SS for determining IGSCC behavior of  $ZrO_2$  coated and uncoated steel. 1. Impeller, 2. Pressure vessel. 3. Upper holder. 4. Upper C(T) specimen. 5. Lower C(T) specimen. 6. Chain piece. 7. Pull rod. 8. Push rod. 9. Clevis [64].

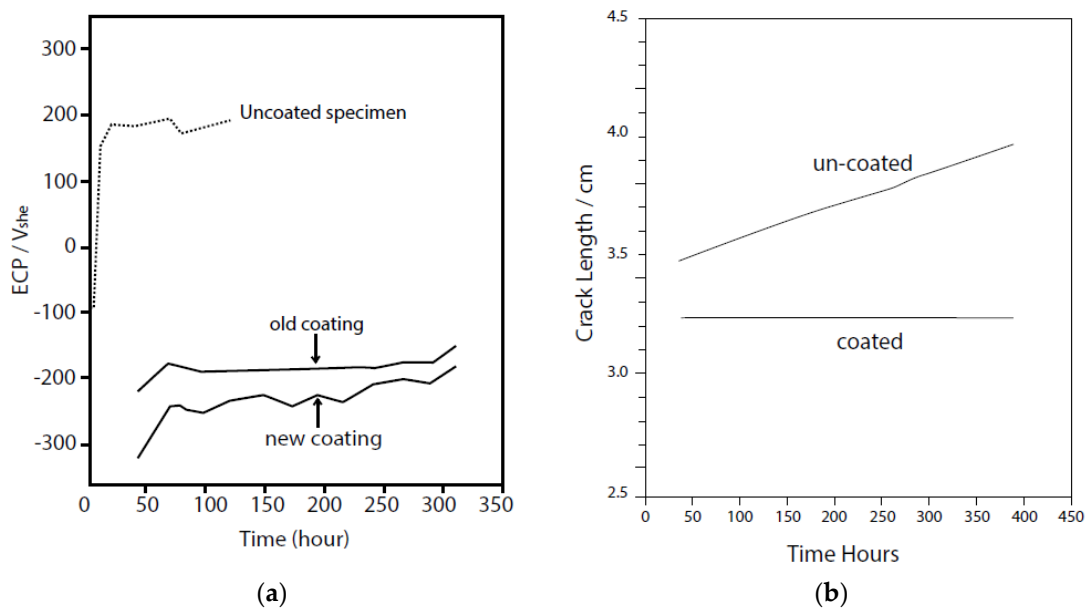


**Figure 29.** Experimental demonstration of the inhibition of IGSCC in sensitized Type 304 SS by a dielectric ZrO<sub>2</sub> coating. The experiment was performed with two C(T) specimens daisy chained together in the same solution of 0.005 M Na<sub>2</sub>SO<sub>4</sub> at 250 °C, [O<sub>2</sub>] = 40 ppm. [64]. (a) ECP vs time. (b) Measured crack length vs time.

In the opinion of one of the present authors (DDM), the critical potential for IGSCC in sensitized Type 304 SS of  $-0.23 V_{she}$  is possibly a too severe a metric, in that under the conditions assumed for a standard crack, it corresponds to a CGR of about  $2 \times 10^{-10}$  cm/s, which is slightly above the creep CGR ( $1.6 \times 10^{-10}$  cm/s at 288 °C, Figure 8). However, a CGR of  $2 \times 10^{-10}$  cm/s corresponds to a crack extension of 63  $\mu$ m over a one-year period of operation or 2.52 mm over 40 years. While this estimate does not account for enhanced CGR during temperature (Figure 10) and conductivity excursions, the worst-case scenario suggests that the accumulated damage might be a factor of 10 higher, amounting to 1-inch (25.2 mm) over 40 years of operation. Noting that an average CGR of  $1 \times 10^{-9}$  cm/s amounts to a crack extension of 0.315 mm over a one-year exposure and to 1.26 cm (1/2-inch) over 40 years of operation, the corresponding critical ECP ( $E_{crit}$ ) for IGSCC might be revised upward to  $-0.05 V_{she}$  (Figure 9) with little apparent risk. This being the case, all the recirculation system should be protected from IGSCC, although the remaining regions all remain susceptible to IGSCC with the accumulated damage being predicted to be in excess of 1-1inch over 40 years.

## 6. Pressurized Water Reactors (PWRs)

### 6.1. Anatomy of a PWR

A PWR coolant system comprises a primary loop containing a pressurized aqueous-based coolant that is pressurized with hydrogen in a pressurizer to suppress boiling, although nucleate boiling occurs (bubbles form and collapse) on the surface of the fuel cladding, and a secondary circuit in which the coolant boils to produce steam that drives conventional turbines to generate electricity [66]. Heat generated by fissioning of the enriched fuel (typically 2.5% <sup>235</sup>U<sub>92</sub>) is exchanged with the secondary circuit via heat exchangers called Steam Generators (SGs). A schematic of the primary coolant circuit of a PWR is displayed in Figure 30.

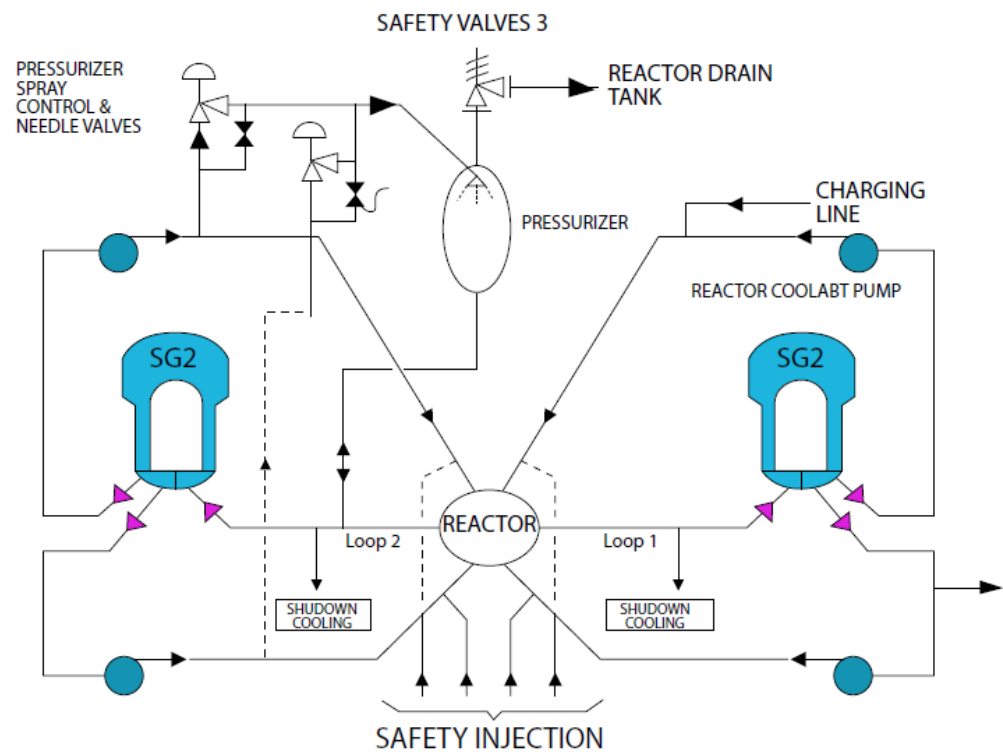
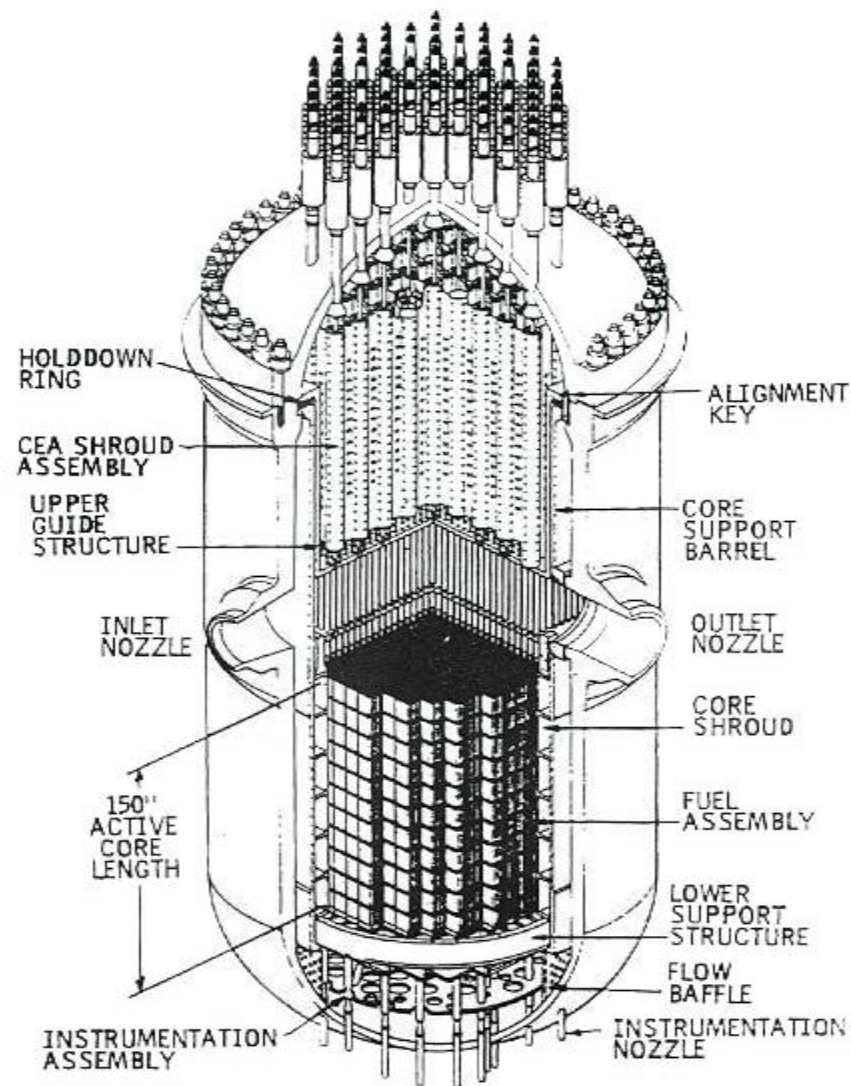


Figure 30. Schematic of a PWR primary coolant circuit [8].

The circuit shown indicates two SGs but, typically, a large unit has three or four. The discussion presented below is restricted to one corrosion problem that has plagued PWRs for several decades; the PWSCC of mill-annealed Alloy 600 SG tubing, an example of which is shown in [5]. The fractures are typically intergranular.

A cut-away view of a recirculating steam generator that is commonly employed in US PWRs is displayed in Figure 31. Of note is the fact that the control rods protrude through the top of the reactor vessel head and are guided into the core to enact shutdown by Alloy 600 guide tubes. The guide tubes are welded to the head at the bottom of the protrusion using an Alloy 182 weld (or a similar weld metal). These welds have failed in many reactors by IGSCC have allowing borated coolant to leak into the annulus between the penetration through the carbon steel head and the outer surface of the tube. Because the annulus is at atmospheric pressure, the borated coolant boiled and resulted in the formation of a concentrated boric acid that proved to be very corrosive to the carbon steel, resulting in the formation of a football-sized hole in the head at the location of the penetration and hence in the head being structurally compromised. The best example of this phenomenon is the Davis Besse PWR in northern Ohio.

The conditions that typically exist in a PWR PHTS under full power operation are summarized in Table 3 [8]. The coolant comprises a boric acid ( $\text{H}_2\text{BO}_3$ ) containing up to 4000 ppm B + up to 4 ppm Li as LiOH at the start of a fuel cycle depending upon the design of the core and the enrichment of the fuel. The boron is added as a “nuclear shim”, as a means of controlling the nuclear reactivity of the core via the reaction  $^{10}\text{B}_5(1n_0, ^4\text{He}_2)^7\text{Li}_3$ , which absorbs excess neutrons that, otherwise, would fission the  $^{235}\text{U}_{92}$  (and  $^{239}\text{Pu}_{94}$ ) in the fuel. Note that as the fuel is “burned up” ( $^{235}\text{U}_{92}$ ) is consumed, the boron concentration decreases and the lithium concentration increases, so that at the end of a fuel cycle the boron is reduced to typically <100 ppm and Li also decreases as displayed in Figure 32. However, the concentration of  $\text{Li}^+$  is controlled by ion exchange to ensure that the pH follows a pre-specified trajectory as displayed in Figure 32.



**Figure 31.** Schematic cut-away diagram of a PWR reactor vessel showing the various internal components [8].

**Table 3.** Typical conditions that exist in the main loop of the primary coolant circuit of a PWR [8,66].

Property	Value	Comment
Temperature	295 °C–330 °C	Typical
Pressure	150 bar (2250 psi)	Typical
Coolant composition	4000–0 ppm B as boric acid, 4–1 ppm Li as lithium hydroxide, depending upon the burn-up of the fuel and the vendor	Li-B trajectory over a typical fuel cycle is shown in Figure 32
Hydrogen concentration	25–55 cc(STP [standard temperature and pressure])/kg(H <sub>2</sub> O)	Some noncommercial units operate with [H <sub>2</sub> ] as high as 70 cc(STP)/kg(H <sub>2</sub> O)
Core channel dose rate		
γ-Photon	$3 \times 10^5$ Rad/s	Typical
Neutron	$6 \times 10^5$ Rad/s	
α Particles	$3 \times 10^5$ Rad/s	
Coolant Mass Flow Rate	18,000 kg/s	Typical

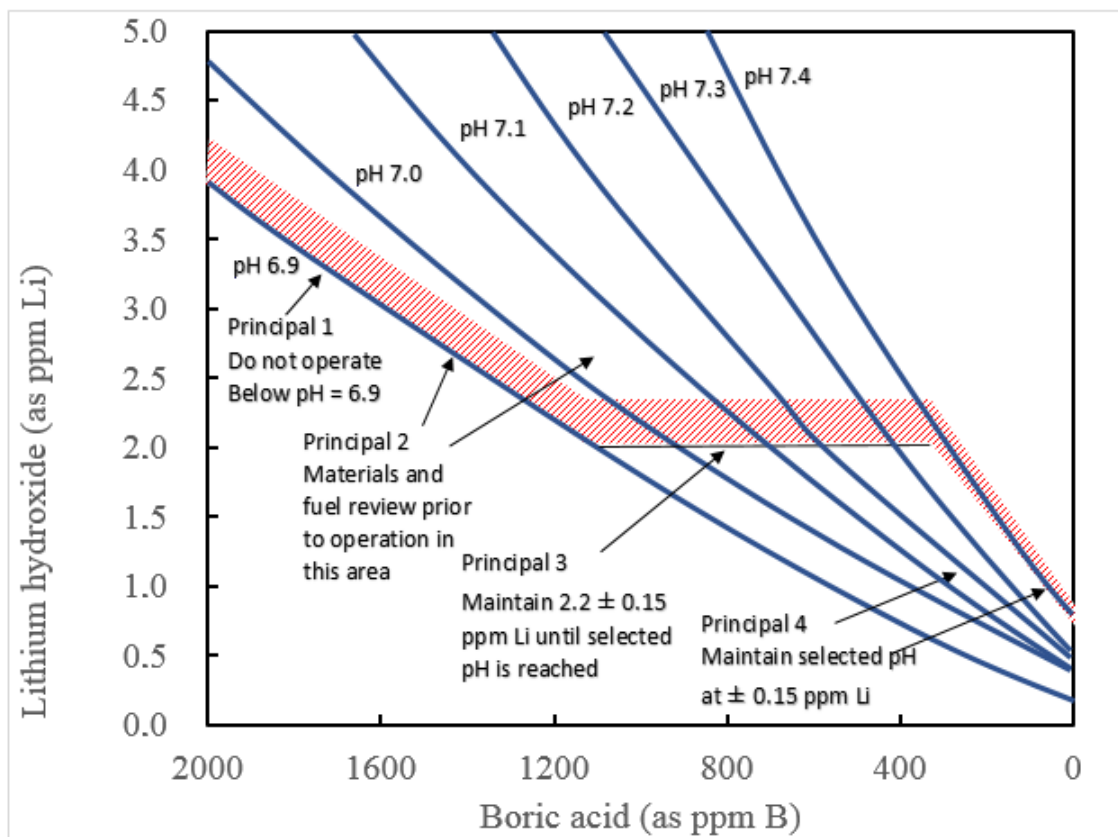


**Figure 32.** pH control strategies affected by adjusting the lithium concentration as the boron is consumed during fuel burnup. The trajectory that is commonly employed over a typical fuel cycle is represented by the hatched path, with the lithium concentration being controlled by ion exchange [8].

### 6.2. Radiolysis/ECP/CGR Modeling of PWR PHTSs

As noted earlier, much less work has been reported on modeling the PHTS of PWRs, possibly because corrosion has been less of an operational problem in these reactors than in BWRs. However, serious corrosion problems have occurred ranging from denting of steam generator tubes in tube/support plate crevices, PWSCC of mill-annealed Alloy 600 steam generator tubes, cracking of control rod guide tubes and other penetrations through the RPV top and bottom head, cracking of highly cold-worked Type 316L SS core barrel bolts, and cracking of Alloy 82/182/600 heater sleeves and other components in pressurizers, to name but a few examples.

The vessel of a PWR differs substantially from that of a BWR, in that the control rods penetrate the vessel head, with only various instrumentation nozzles and assemblies penetrating the bottom (Figure 31). Additionally, because the coolant does not boil (except for nucleate boiling on the fuel in the fuel channels), the vessel does not contain steam separators or dryers, as in the case of a BWR. Accordingly, no separation of volatile gases to the steam phase occurs in a PWR as it does in the case of a BWR. This makes describing the redox electrochemistry in a PWR primary coolant circuit somewhat more straightforward than for a BWR, even though the chemistry itself is significantly more complex (Table 3) than that of pure water in a BWR PHTS. Thus, there are significant differences between the primary coolant circuits of PWRs and BWRs, regarding coolant chemistry, materials of fabrication, physical geometry, flow path configuration, and in-core dose rates. Firstly, the coolant in the primary circuit of a PWR is a boric acid/lithium hydroxide solution, with the boric acid concentration starting at the beginning of a fuel cycle at a concentration of 2000–4000 ppm of boron (0.18–0.36 m), depending upon the reactor, and ending as essentially depleted (Figure 32). As noted above, the boron is used as a “nuclear shim” to control core reactivity via the absorption of neutrons by  $^{10}\text{B}_5$

via the nuclear reaction  $^{10}\text{B}_5(^1\text{n}_0, ^4\text{He}_2)^7\text{Li}_3$ , which has a high capture cross section for thermal neutrons. Simultaneously, some of the excess neutrons are captured by  $^{238}\text{U}_{92}$  via  $^{238}\text{U}_{92}(^1\text{n}_0, ^0\text{e}_{-1})^{239}\text{Np}_{93}$  that decays by  $\beta$  (i.e.,  $^0\text{e}_{-1}$ ) emission to  $^{239}\text{Pu}_{94}$  via the reaction  $^{239}\text{Np}_{93}(^0\text{e}_{-1})^{239}\text{Pu}_{94}$ . This plutonium isotope is also fissile and fissions to produce energy and additional neutrons. Indeed, it is estimated that at the end of the fuel cycle, about 40 % of the fission energy produced in the core of a PWR is derived from the fissioning of  $^{239}\text{Pu}_{94}$ . Thus, a PWR “breeds” fuel, but is not classified as a “breeder reactor”, because the breeding (conversion) ratio ( $^{239}\text{Pu}_{94}$  produced/ $^{235}\text{U}_{92}$  consumed) is less than one. As the concentration of  $^{235}\text{U}_{92}$  in the fuel is depleted from an initial value of about 2.5%, (compared with the natural abundance of 0.7%), the number of “excess” neutrons gradually decreases, corresponding to a reduction in core reactivity, so that the boron concentration is reduced correspondingly by neutron transformation while the lithium concentration increases. The pH of the coolant depends upon the B/Li ratio and this ratio is carefully controlled by lithium ion exchange columns to maintain the ratios depicted by the shaded trajectory shown in Figure 32.

Thus, initially, the B/Li ratio is controlled such that the pH of the coolant at the full power operating temperature (350 °C) is slightly above 6.9 but after almost 50 % through burn-up, the ratio is controlled such that the pH increases to 7.4. Thereafter, the ratio is controlled so that this pH is maintained as the remaining B is consumed. At that point, the [Li] is about 1 ppm. This “coordinated water chemistry” protocol was adopted to control the corrosion of ferrous alloys, but we show later in this review that this protocol needs to be modified to reduce PWSCC of Alloy 600 steam generator tubing.

Note that boron, which is added to the primary coolant to act as a “nuclear shim,” produces lithium via the nuclear reaction  $^{10}\text{B}_5(^1\text{n}_0, ^4\text{He}_2)^7\text{Li}_3$  as well as alpha particles ( $^4\text{He}_2$ , 2.31 and 2.79 MeV). The  $\alpha$ -particles ( $^4\text{He}_2$ ) produced by this reaction contribute to the radiolysis of water. Table 3 summarizes dose rates from neutrons,  $\gamma$ -photons, and alpha particles produced in the core of a typical PWR, corresponding to dose rates of  $3 \times 10^5$  Rad/s,  $6 \times 10^5$  Rad/s and  $3 \times 10^5$  Rad/s, respectively. These dose rates are about an order of magnitude greater than those in a BWR, because of the higher power density of a PWR core and it is noted that alpha irradiation accounts for a significant fraction of the total energy deposited in the coolant.

Modeling of the electrochemistry of a PWR primary coolant circuit has been reported by a number of groups [8,66–77], including Macdonald and Urquidi-Macdonald [8,69] using a custom code titled PWR\_ECP. The PWR\_ECP code is similar in structure to the DAMAGE-PREDICTOR code that the authors previously employed to model state points in BWRs, as described above [19]. The code has now been extended to the point of predicting the accumulation of damage due to SCC over the corrosion evolutionary path for the reactor, primarily because of the (then) lack of a viable CGR model that can accommodate HIC at the time that the work was performed (year 2000; such a model now exists [14,78]). Instead, PWR\_ECP predicts the ECP vs. distance in the main loop and four secondary loops, as follows: (1) main loop, (2) Reactor Water Clean Up (RWCU) loop, (3) Reactor Heat Removal System (RHRS), and (4) pressurizer.

The PWR\_ECP code begins by employing a chemical speciation model to calculate the composition of the coolant and the pH at closely spaced points around the primary coolant circuit, including the pressurizer, RWCU, and RHRS loops (Figure 33).

Note that the purpose of the RHRS is to remove decay heat from the core upon shutdown of the reactor. Accordingly, this system is isolated from the primary coolant circuit during normal operation. As noted above, the radiolysis of water is predicted using a 48-model radiolysis model, based upon that of Christensen [75], with the radiolytic yields being given in by the same authors. The calculations were carried out at 10 cm increments, with the ECP being calculated at each increment using the Mixed Potential Model (MPM) [10]. Dose rates for  $\gamma$ -photons, neutrons, and  $\alpha$ -particles, coolant path geometry, and detailed thermal hydraulic data for each location was provided by the vendor for whom the modeling work was performed.

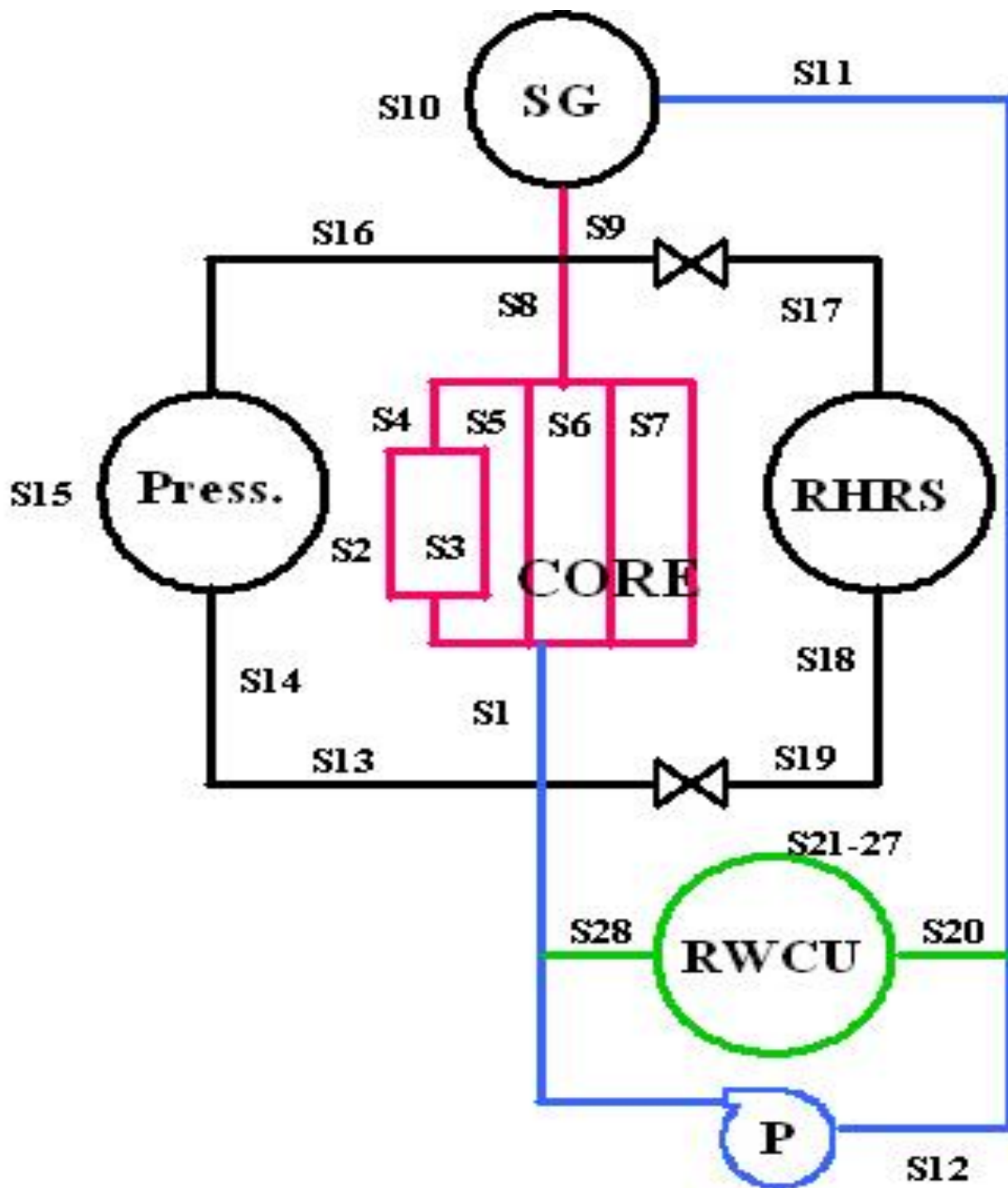


**Figure 33.** Schematic of the primary coolant circuit of a PWR, showing the three principal loops: (1) main loop (S1–S12); (2) RHR (S17–S19); (3) RWCU (S20–S28), and (4) pressurizer (S13–S16) [8].

The primary coolant circuit loops were divided into 28 sections (c.f., 10 or 11 sections in the BWR case) as shown in Figure 15. Each section is characterized by an inlet and outlet temperature;  $\gamma$ ,  $n$ , and  $\alpha$  dose rates; flow fraction; linear flow velocity; hydrodynamic diameter; section length; material of construction ( $SS \equiv$  Stainless Steel); and exchange current density multipliers, as in the case of the BWR models discussed earlier. If the inlet and outlet temperatures are different, it is assumed that the temperature varies linearly with distance between the two values. The code was used to model the ECP around the

primary coolant system for normal operation with deoxygenated (5 ppb  $O_2$ ) or oxygenated makeup water (5.0 ppm  $O_2$ ) and for cold shutdown conditions. Facilities are included in the PWR\_ECP code and its later variants [79] for modeling the periodic injection of oxygen and hydrogen peroxide into the RWCU and of oxygen into the RHRS. The concentration of hydrogen was set to 25 cc(STP)/kg( $H_2O$ ) and the coolant mass flow rate was 18,000 kg/s.

Figure 34 displays the predicted ECP vs. distance from the bottom of the core for normal, full power operation, which includes the injection of 5 ppm of  $O_2$  into the feedwater. All the sections, except for Section 7, display ECP values between  $-0.35 V_{she}$  at the core entrance and  $-0.30 V_{she}$  at the core exit. On the other hand, Section 7, which is the bypass channel, is predicted to have an ECP of  $-0.75 V_{she}$ , regardless of the position. The higher ECP in the fuel channels and related areas reflects the generation of oxidizing radiolysis products in spite of the fact that the coolant contains 25 cc(STP)/kg( $H_2O$ ) (cf. Figure 1).

Figures 35–37 display the predicted ECP vs. distance for the three principal loops in the coolant circuit under normal, full power operation with oxygenated makeup water: (1) the main loop, (2) the pressurizer, and (3) the RWCU. Note that under these operating conditions, the RHRS is not operated, so that calculated ECP data for this loop are not presented. The most important finding is that the ECP is predicted to vary over a wide range ( $-0.74$  to  $-0.20 V_{she}$  in the main loop) in a manner that is reminiscent of the primary coolant circuit of a BWR. Accordingly, the widespread belief that the primary circuit of a PWR behaves as a “giant hydrogen electrode” appears to be untenable, at least based upon the present analysis.

### Normal Operation-Core Section -Cycle 3

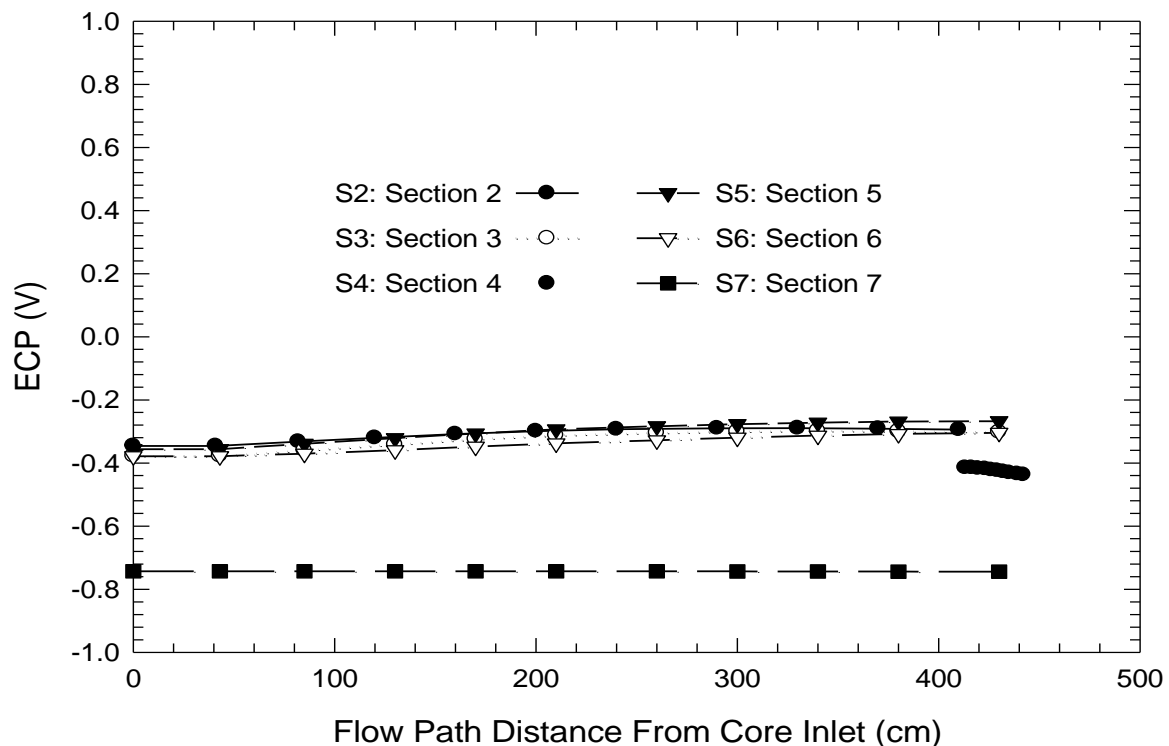


**Figure 34.** ECP vs. distance in a PWR under normal, full power operation. S1 = Core return, S2 = Fuel channels, S3 = Hot zone, S4 = Top part of the core, S5 = By-pass Tube Guide, S6 = By-pass hot zone, S7 = By-pass grid [8].

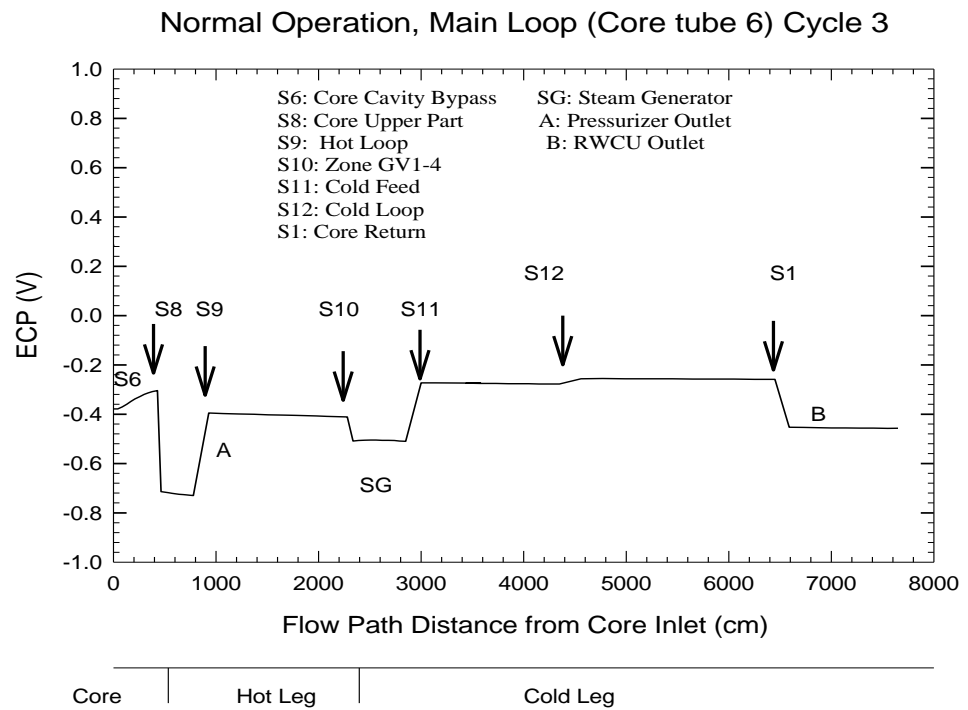


**Figure 35.** ECP vs distance for the main primary coolant loop in a PWR under normal, full power operation [8].

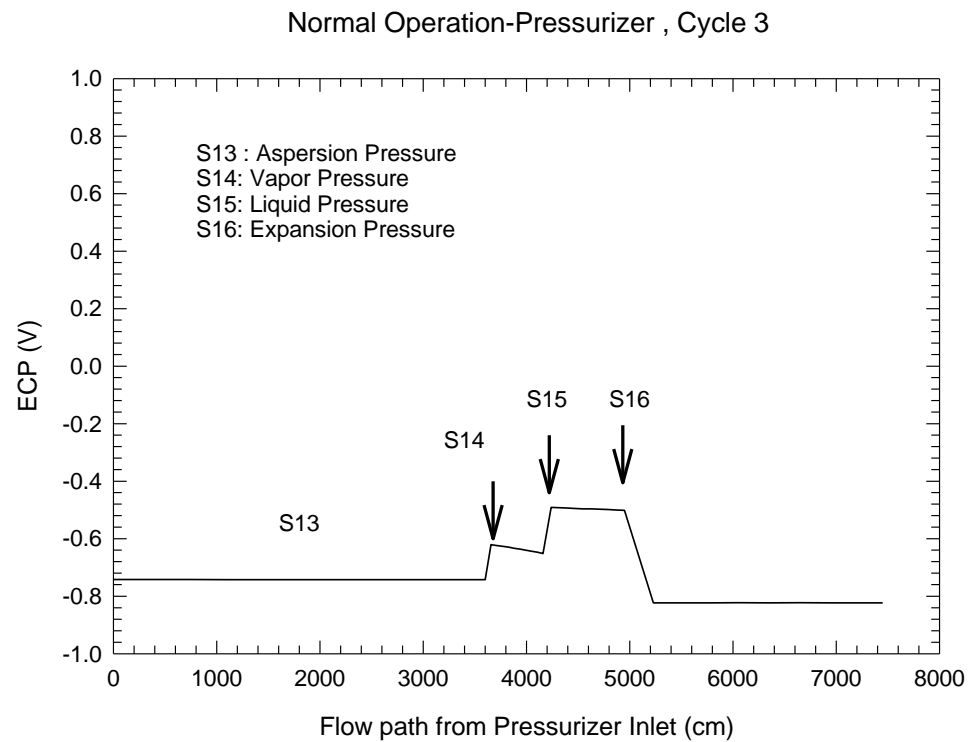


**Figure 36.** ECP vs. distance for the pressurizer loop in a PWR under full power operation [8].

## Normal Operation-RWCU, Cycle 3

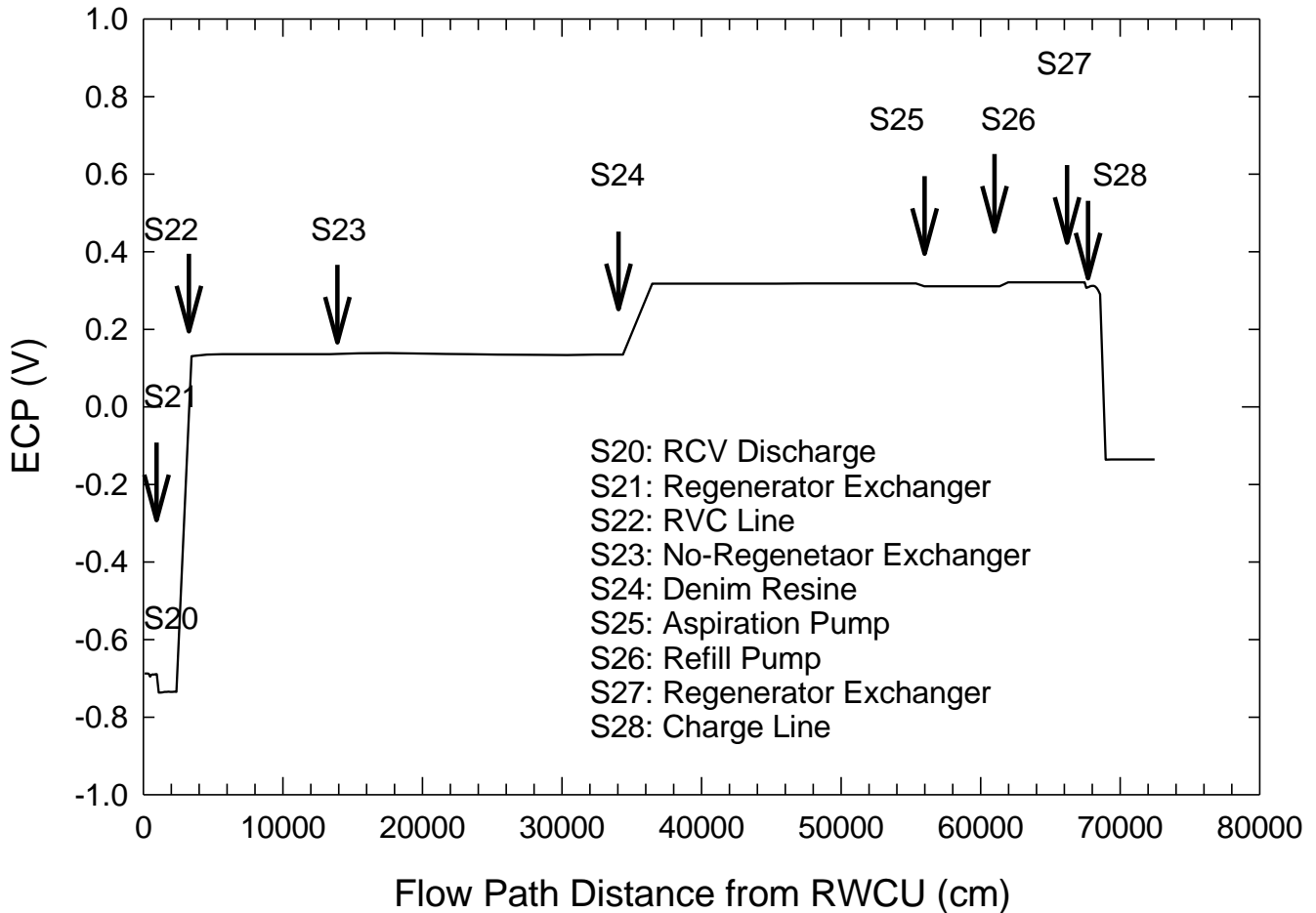


**Figure 37.** ECP vs. distance for the RWCU in a PWR under full- power operation [8].

The ECP in the pressurizer circuit is predicted to be very negative over most of the loop, with values ranging from  $-0.75$  to  $-0.81V_{\text{she}}$  in Sections 13 and 16 (Figure 36). This is not surprising because no radiation dose is present, so that no oxidizing radiolysis products are produced. However, the ECP in Sections 14 and 15 (Figure 35) is predicted to rise to about  $-0.45V_{\text{she}}$ . The origin of this rise is currently undefined [8].

Finally, the ECP in the RWCU (Figure 37) is predicted to be very positive over most of the loop, corresponding to the low temperature of operation ( $45^{\circ}\text{C}$ – $55^{\circ}\text{C}$ ). That the change in temperature is the cause of the sharp positive shift in the ECP is evident from comparing the ECP values before and after application of the HXs.

### 6.3. PWR Steam Generators

A schematic of a PWR recirculating steam generator (SG) is depicted in Figure 38a. The primary coolant from the reactor enters the primary inlet, flows up through the hot leg tubing, down the cold leg tubing and is returned to the reactor via the primary outlet [79,80]. A myriad of corrosion problems has been reported in recirculating steam generators as summarized in Figure 38b.

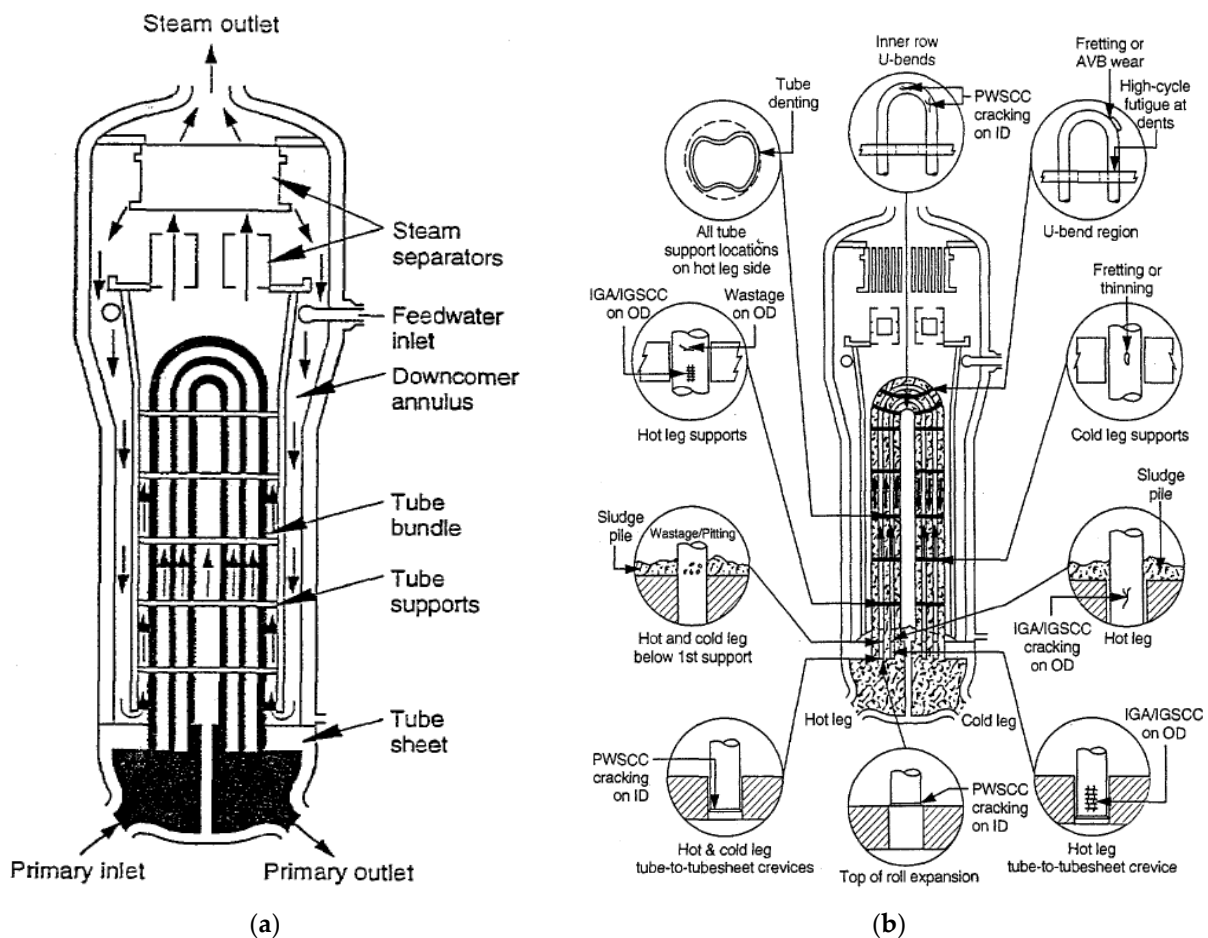


**Figure 38.** (a) Schematic of a PWR recirculating steam generator; (b) Location of known tube wall degradation phenomena in recirculating steam generators. [79,80].

As noted above, recirculating steam generators have experienced a myriad of corrosion problems that has led to extensive loss of service and steam generator replacement worldwide, as summarized in Figure 39 [80]. In the 1970s, wastage and denting were the dominant problems but, more recently, PWSCC and ODS/IGSCC have come to be the prime causes of SG degradation. In this discussion, we are primarily concerned with only one cause of SG degradation; the ID PWSCC that is found to occur on the ID surfaces of the Alloy 600 tubing in both the hot leg and the cold leg in the roll transition zone within the lower tube plate/tube penetration and at the upper U bends. Both are regions of high residual stress because of tube bending and tube expansion into the tube sheet.

Following the work of Totsuka and Smialowska [5], who demonstrated the critical roles of electrochemistry and HIC in PWSCC, Kim [71] modified the PWR\_ECP code of Macdonald and Urquidi-Macdonald [8] to address PWSCC in Korean PWRs. Of specific interest was the relationship between the water chemistry protocol during fuel burnup and the occurrence of PWSCC. Thus, it is known that mill-annealed Alloy 600 steam generator tubes suffer HIC at potentials that are more negative than  $-0.835 V_{\text{she}}$  [5]. As shown in Figures 34–37, the potential does indeed approach this critical value in typical PWRs and the additional modeling work of Kim [71] and Kim and Macdonald [68] shows that the ECP of the Alloy 600 steam generator tubes is displaced well below (i.e., is more negative) than  $-0.820 V_{\text{she}}$  toward the end of a fuel cycle on the current water chemistry protocol (“coordinated water chemistry”) [Figure 40a], thereby accounting for the rash of PWSCC that has plagued PWR operators in recent years [81]. Those same calculations indicate that the problem may be avoided by tailoring the primary circuit chemistry over the fuel cycle, as explained below [68,71]. We also note that deterministic crack growth rate models

have been developed for predicting the evolution of PWSCC in Alloy 600 steam generator tubes and in other components in PWRs that employ the same or similar alloys (e.g., Alloy 182) [14,78] but they have yet to be applied to predicting damage in actual reactors.

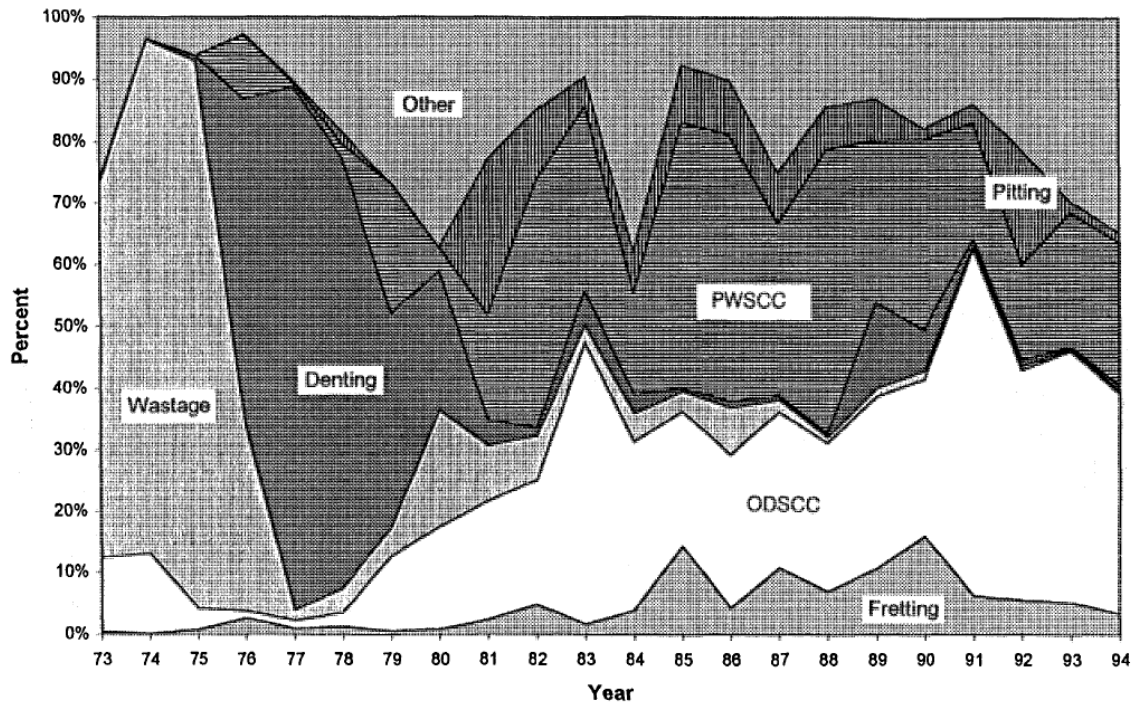
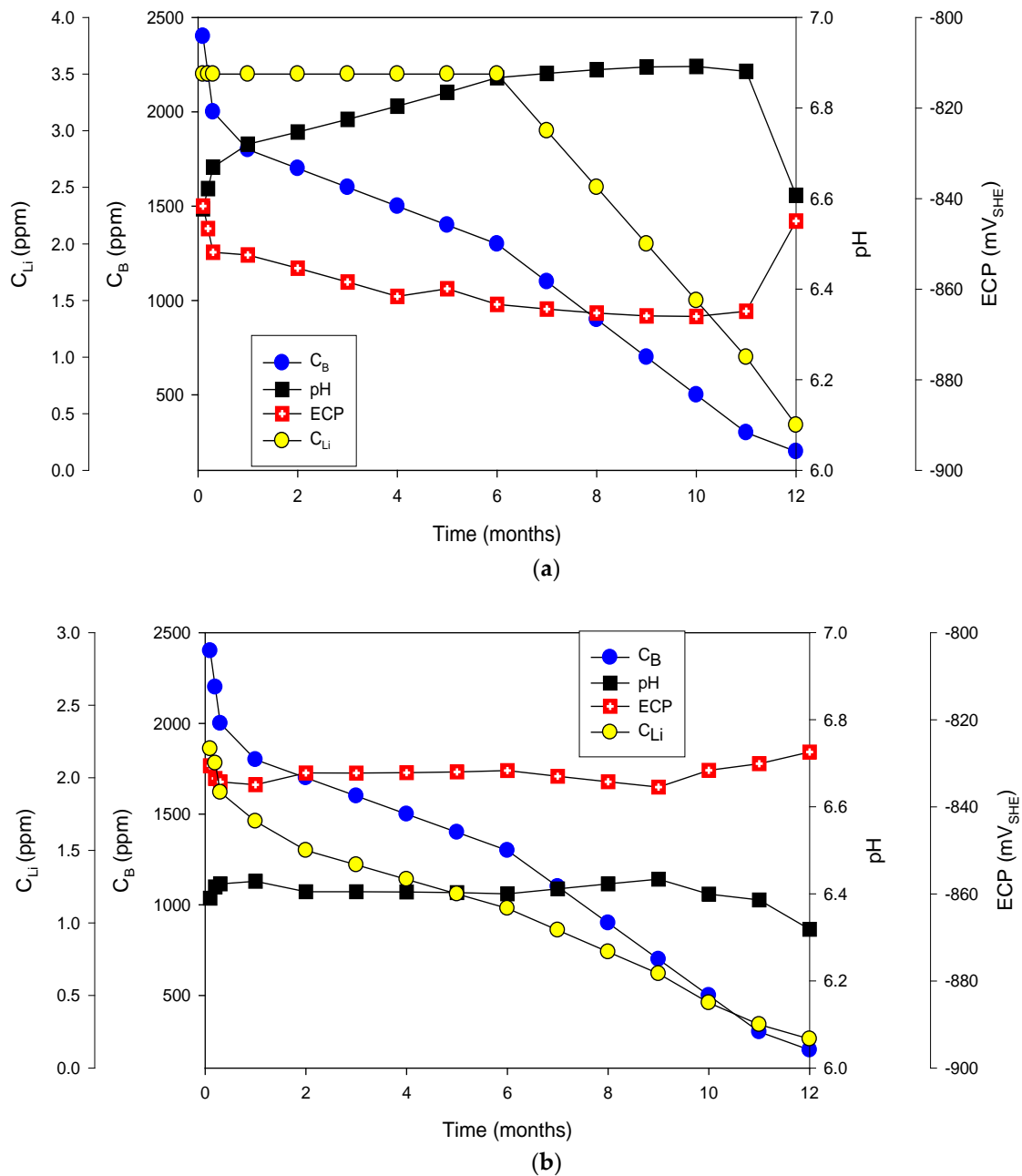


Figure 39. Causes of steam generator tube plugging in PWRs worldwide [80].

Modeling of the type described in this review may be used to mitigate serious problems in reactor operation, as illustrated here with reference to PWSCC in PWR Alloy 600 steam generator tubing. PWSCC in the tubing has plagued the operation of those reactors over several decades. Thus, under coordinated water chemistry as defined by the trajectories of the concentrations of boron and lithium over a fuel cycle, which is widely practiced (Figure 40a), the ECP of the Alloy 600 steam generator tubes in the hot leg remains below (i.e., more negative than) the critical value for PWSCC of  $-0.820 V_{she}$ , and hence the tubes are in a perpetual state of cracking.

On the other hand, if the reactor is operated under the proposed “adjusted water chemistry” protocol, as shown in Figure 40b, the ECP remains at or above the critical potential of  $-835 mV_{she}$  over the entire fuel cycle, thereby mitigating PWSCC in the steam generator tubes. As noted previously, the CGR is proportional to  $exp[-(ECP - E_{crit})]$ , where, in this case, a negative sign appears before the overpotential, because PWSCC, a form of HIC, is a cathodic process. Thus, the rate increases exponentially as the ECP becomes more negative than  $E_{crit}$ . Of course, “balance of plant” issues would need to be addressed to determine whether any unintended consequences could arise from such a change in water chemistry. For example, it is seen from Figure 40b that the pH must be reduced by as much as 0.4 of a unit to affect the desired change in the ECP, and the effect that this change would have on activity and mass transport and general corrosion in the primary circuit would have to be determined. Nevertheless, the example given above is intended to illustrate how detailed physico-electrochemical modeling may be used to refine the operation of nuclear reactors to avoid costly materials degradation phenomena, and it is hoped that the same can be achieved in the development of fusion power.



**Figure 40.** (a) Predicted ECP and pH over a fuel cycle for a PWR operating on coordinated water chemistry and (b) adjusted water chemistry (b).  $[H] = 25 \text{ cm}^3(\text{STP})/\text{kgH}_2\text{O}$ ,  $T = 320 \text{ }^\circ\text{C}$  (after Kim [68,71]).

## 7. Predicted ECP and CGR in ITER PHTS

Because the ITER has yet to operate, no actual plant data are available on the ECP in the PHTS. However, a few attempts have been made to calculate or measure the ECP of structural materials in the IBED PHTS. One such study was reported by Wikman et al. [81], in which the ECP was calculated from the concentrations of the radiolysis products over multiple burn/dwell cycles using an MPM [81] that is essentially identical to the MPM developed by Macdonald [10] in the early 1980s to model the ECP in the primary coolant circuits of water-cooled fission reactors (i.e., BWRs and PWRs). Their results are plotted in Figure 41. The potential is predicted to be about  $100 \text{ mV}_{\text{she}}$  for a temperature of  $150 \text{ }^\circ\text{C}$  during the plasma burn, that is, when the radiation dose rate is high, corresponding to the net production of oxidizing species in the coolant, even though the coolant is stated

to contain 25 cc (STP)/kgH<sub>2</sub>O (2.23 ppm) of hydrogen. This is slightly more positive than  $E_{crit}$  for IGSCC in sensitized Type 304 SS in BWR coolant at 150 °C (0.063  $V_{she}$ , Table 2), so that IGSCC is expected to be spontaneous if a crack initiates. During the dwell period, the ECP decreases with time as the radiolysis products recombine or react with structural materials to lower the concentrations of H<sub>2</sub>O<sub>2</sub> and O<sub>2</sub> and finally attains a value of about  $-460 \text{ mV}_{she}$ , which is far more negative than  $E_{crit}$ , so that crack advance is expected to cease. The transient in ECP is apparently repetitive from cycle to cycle, indicating that no cumulative effects exist. These results suggest that the ECP will be slightly more negative in the radiation zone than in the case of a BWR operating under NWC conditions [cf., Figure 19a], but it will not be as negative as that predicted for the primary circuit of a PWR. As noted in [81], the ECP during the plasma burn is considerably higher (i.e., more positive) than the critical potential for IGSCC in sensitized Type 304 SS. The ECP is also more positive than the pitting potential for this alloy, indicating that pitting may occur even at very low chloride concentrations ( $<1 \text{ ppb}$ ,  $[\text{Cl}^-] = 2.86 \times 10^{-11} \text{ m}$ ).

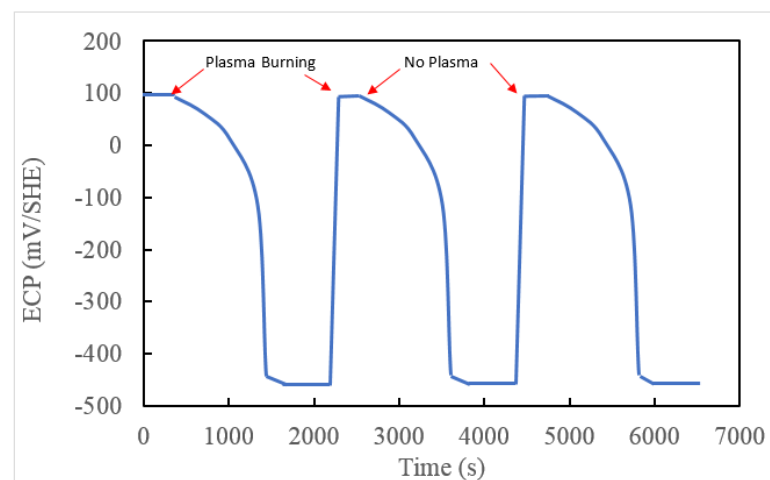


**Figure 41.** Variation of ECP of stainless steel in the ITER PHTS as a function of periodic plasma burning of 400 s in pure water at 150 °C (after Wikman et al. [81]).

Because of the predicted cyclical nature of ECP vs. time for the ITER PHTS (Figure 41), it is important to ascertain the impact of the change in ECP on the CGR. The principal issue here is whether a crack will immediately cease growing when the ECP is displaced below  $E_{crit}$  and then immediately start regrowing when the ECP is displaced above  $E_{crit}$ . We could find no data in the literature on this issue for ITER coolant conditions ( $T = 150 \text{ °C}$ ) but some work has been reported for dilute saline solutions (0.01 m NaCl) at 250 °C, as plotted in Figure 42 [38]. These experiments were performed in a CERT using a gauged, round tensile specimen under potential control. Once a crack nucleates at  $-0.20 \text{ V}_{she}$  ( $> E_{crit}$ ), the load drops as the crack propagates through the specimen. However, if the potential is then changed to  $-0.70 \text{ V}_{she}$  ( $< E_{crit}$ ), the load is observed to rise, indicating that the crack ceases to propagate. This process is repetitive, as indicated in the figure. Even though the conditions of the experiment are significantly different than those that will exist in the ITER PHTS, these data argue that any crack that nucleates will grow cyclically as the ECP cycles during operation. From Figure 9, we note that the CGR for IGSCC in sensitized Type 304 SS in water at 150 °C is about  $2 \times 10^{-7} \text{ cm/s}$ . Thus, over the plasma burn period of 400 s, any active crack is expected to grow by about  $8 \times 10^{-5} \text{ cm}$  (0.8  $\mu\text{m}$ ). Over 30,000 cycles, the intended lifetime of ITER, the crack would grow by about 2.4 cm (1-inch).

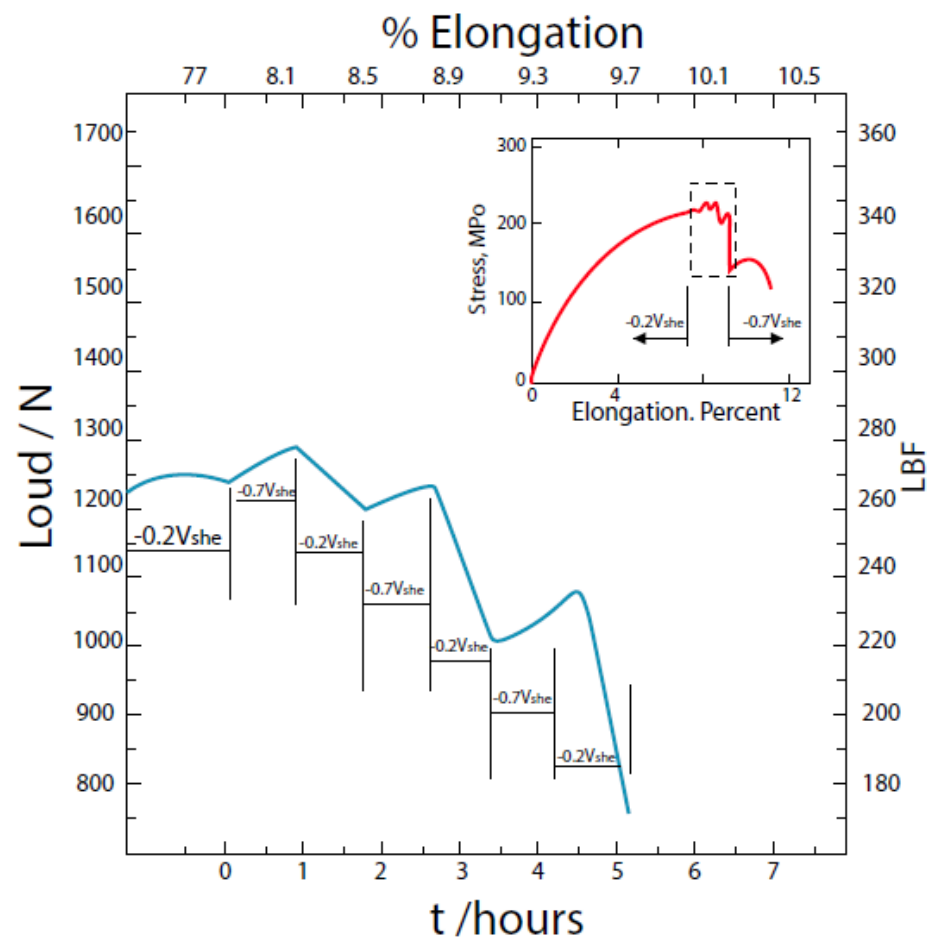


**Figure 42.** Variation of nominal stress vs. elongation/time for the IGSCC in sensitized Type 304 SS in 0.01 m NaCl solution at 250 °C as the potential is cyclically switched between  $-0.20 V_{she}$  (cracking) and  $-0.70 V_{she}$  (no cracking) [38].

Saji [82] has also attempted to calculate the potential in the ITER PHTS and his calculated “redox” potential is plotted in Figure 43 as a function of dose rate. Although the caption of the original figure clearly identifies the potential as being the “redox potential” (i.e., the potential sensed by an inert sensing electrode such as Pt or Au), the text also identifies the potential as being the “ECP”. The ECP is the open circuit *corrosion* potential measured on a corroding substrate and hence is conceptually different than the redox potential, because of the participation of the partial anodic dissolution of the metal substrate. In any event, the potential was calculated using the Nernst equation, which applies strictly to a system at equilibrium, whereas both the redox potential and the ECP are nonequilibrium, “mixed potentials.” The error appears to result from a fundamental misunderstanding of the nature of electrochemical processes at metal/solution interfaces. Nevertheless, the calculations show that in the irradiation zone, the potential increases monotonically with increasing dose rate, which is the expected behavior. In the non-irradiated zone, the potential is predicted to be low ( $-0.52 V_{she}$ ), which is in reasonable agreement with the predictions of Wikman [81] during the dwell period, when irradiation has ceased and the water radiolysis products have recombined (Figure 41). However, during the plasma burn in the irradiation zone, the predictions of Saji [82] and Wikman et al. [81] are quite different, possibly because Saji employed the Nernst equation to calculate the potential, rather than a MPM.

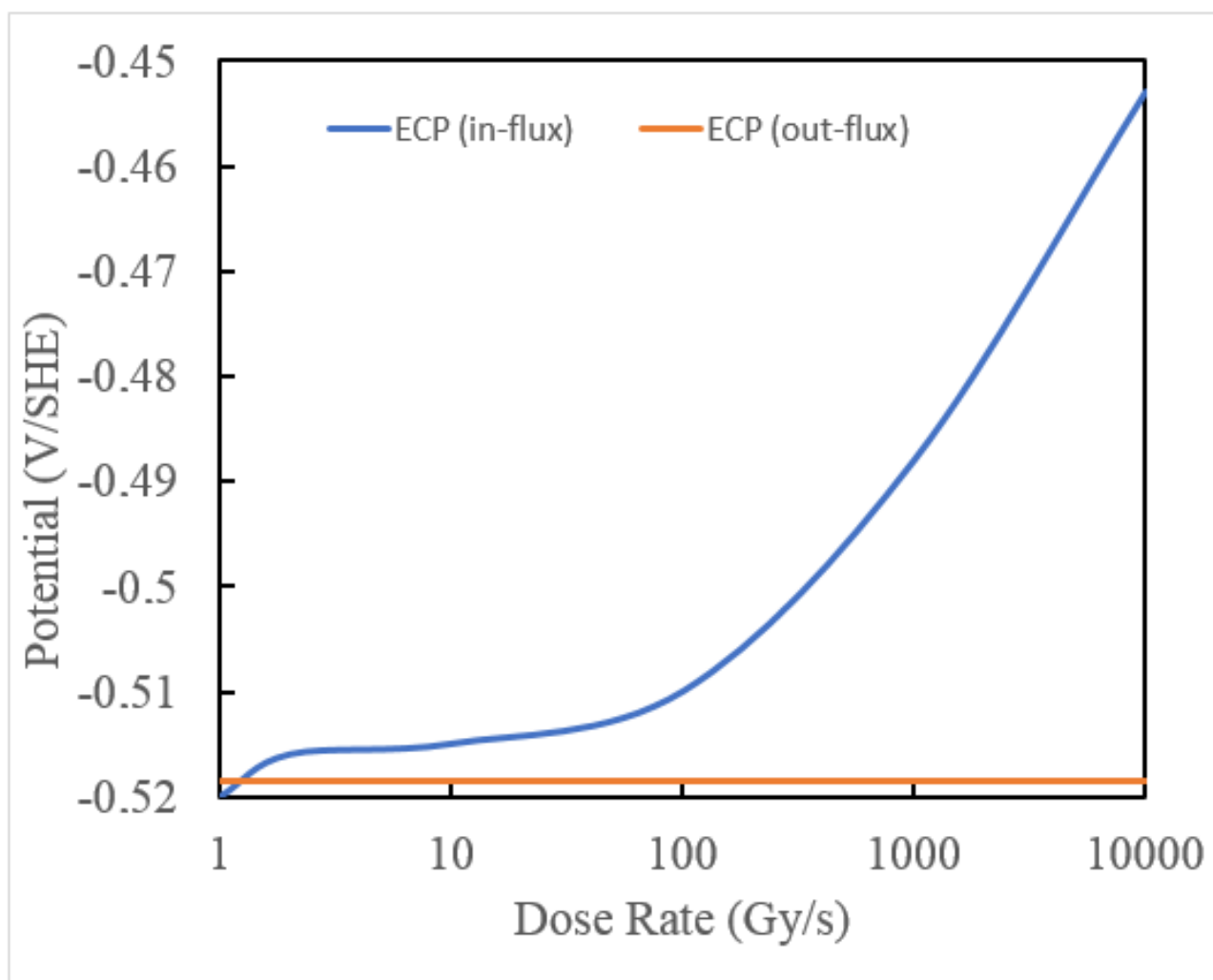


**Figure 43.** Calculated redox potential as a function of radiation dose rate according to Saji [82].

In Part I of this series [1] we report extensive modeling work on the radiolysis of the water coolant in the IBED PHTS of the ITER. The work predicted the concentrations of  $H_2$ ,  $O_2$ , and  $H_2O_2$  in the in-plasma flux area (PFA), a region that is subjected to intense, high energy (14.1 MeV) neutron irradiation and high energy (15–25 MeV)  $\gamma$ -photon irradiation, and in the out-of-plasma flux area (OPFA), where the  $n$  and  $\gamma$ -photon deposition rate is zero, but where residual irradiation occurs because of the presence of  $^{16}N_7$  and  $^{17}N_7$  that form via the neutron capture by  $^{16}O_8$  [i.e.,  $^{16}O_8(1n_0, 1p_1)^{16}N_7$  and  $^{17}O_8(1n_0, 1p_1)^{17}N_7$ , respectively] and neutron activated (metal) isotopes (e.g.  $^{60}Co_{27}$  in corrosion products). However, the energy deposition rates from these (and other) isotopes are not sufficiently large to have any significant impact on the concentration of the radiolysis products of water. Accordingly, in the following analysis, these contributions are ignored and irradiation is assumed not to occur in the OPFA.

The complex IBED PHTS comprises multiple units called “blocks”, each of which is in a specific location within the coolant system. The block that we chose to model represents 15 Equatorial Ports, which will experience the highest energy deposition rates ( $3.2 W/cm^3$  and  $4.3 W/cm^3$  for neutron and  $\gamma$ -photon irradiation, respectively) and can be considered as the block with the most severe corrosion conditions in the PFA. The set of initial parameters that describe the radiolysis conditions in the circuit for one particular case for which 1.0 cc(STP) /kg  $H_2O$  (0.09 ppm) of  $H_2$  is added to the feed water prior to the inlet of the PFA is presented in Table 4. The oxygen, nitrogen, and metal ion concentrations are

the design maximum values (DMV). Accordingly, the IBED PHTS can be condensed into a simple equivalent circuit, as shown in Figure 44. The generation of the radiolysis products in the IBED PHTS water is illustrated by modeling a block that represents Equatorial Ports.

The set of initial parameters that describe the radiolysis conditions in the circuit for one particular case for which 1.0 cc(STP)/kgH<sub>2</sub>O (0.09 ppm) of H<sub>2</sub> is added to the feed water prior to the inlet of the PFA is presented in Table 4. The energy deposition rates (3.2 W/cm<sup>3</sup> and 4.3 W/cm<sup>3</sup> for neutron and  $\gamma$ -photon irradiation, respectively) are predicted to be the highest of any module in the coolant circuit. The oxygen, nitrogen, and metal ion concentrations are the design maximum values (DMV). Curiously, no DMV has been adopted for hydrogen peroxide, even though this species, on a per mole basis, is by far the most deleterious radiolysis product in the circuit. Additionally, there does not appear to be a DMV for Cl<sup>-</sup> even through this species essentially controls the critical potential for passivity breakdown and hence the critical potential for the nucleation of stress corrosion cracking, at least for those cracks that nucleate from pits, giving rise to the condition for the occurrence of IGSCC in stainless steel as  $ECP > E_{crit}^{BWR}$ . Finally, the transit time,  $t_L = 81.3$  s, is the time for an element of the coolant to travel around the circuit. Of that time, 50 s are spent in the PFA and 31.3 s in the OPFA.

**Table 4.** Set of Parameters for the Single Module Radiolysis Assessment.

Parameter	Value
Hydrogen, cc (STP)/kg	1
Oxygen, ppb	10
Cu <sup>2+</sup> , ppb	10
Cu <sup>+</sup> , ppb	0
Fe <sup>2+</sup> , ppb	10
Fe <sup>3+</sup> , ppb	0
N <sub>2</sub> , ppm	2
Temperature, °C	98
$t_L$ , s	81.3
$Q_n$ , W/cm <sup>3</sup>	3.2
$Q_\gamma$ , W/cm <sup>3</sup>	4.3

The predicted, steady state concentrations of the three principal radiolysis products (H<sub>2</sub>, O<sub>2</sub>, and H<sub>2</sub>O<sub>2</sub>) in the PFA are given in Table 5 in units of M and ppb. For comparison, a typical BWR operating under NWC conditions (no H<sub>2</sub> added to the coolant), the H<sub>2</sub>, O<sub>2</sub>, and H<sub>2</sub>O<sub>2</sub> are predicted to be 7 ppb, 100 ppb, and 100 ppb, respectively, showing that the redox conditions in the IBED PHTS in the ITER will be somewhat more aggressive than in a BWR, although a direct comparison is difficult because the systems are at different temperatures (98 °C and 288 °C, respectively).

**Table 5.** Steady state concentrations of H<sub>2</sub>, O<sub>2</sub>, and H<sub>2</sub>O<sub>2</sub> and the estimated ECP and CGR for a standard crack in sensitized Type 304 SS in the in-the PFA of an Equatorial Port Block in the IBED PHTS of the ITER as a function of inlet hydrogen concentration, [H<sub>2</sub>]<sub>inlet</sub>.

[H <sub>2</sub> ] <sub>Input</sub> cc (STP)/kg H <sub>2</sub> O	[H <sub>2</sub> ] <sub>Input</sub> M	[H <sub>2</sub> ] <sub>Input</sub> ppb	[H <sub>2</sub> ] <sub>ss</sub> ppb	[O <sub>2</sub> ] <sub>ss</sub> ppb	[H <sub>2</sub> O <sub>2</sub> ] <sub>ss</sub> ppb	ECP V <sub>she</sub>	CGR cm/s
0	0	0	31.7524	144.8283	212.1415	0.4389	$9.71 \times 10^{-6}$
0.1	$4.31 \times 10^{-6}$	8.9229	21.6517	15.9027	212.4514	0.4480	$1.18 \times 10^{-5}$
0.2	$8.61 \times 10^{-6}$	17.8442	26.5881	4.1772	170.4914	0.4374	$9.41 \times 10^{-6}$
0.5	$2.15 \times 10^{-5}$	44.6146	48.101	0.5303	87.2583	0.4047	$4.69 \times 10^{-6}$
1	$4.31 \times 10^{-5}$	89.2292	90.4824	0.0925	48.5876	0.3744	$2.46 \times 10^{-6}$
10	$4.37 \times 10^{-4}$	892.2089	891.8567	$6.38 \times 10^{-4}$	20.9557	0.2909	$4.14 \times 10^{-6}$

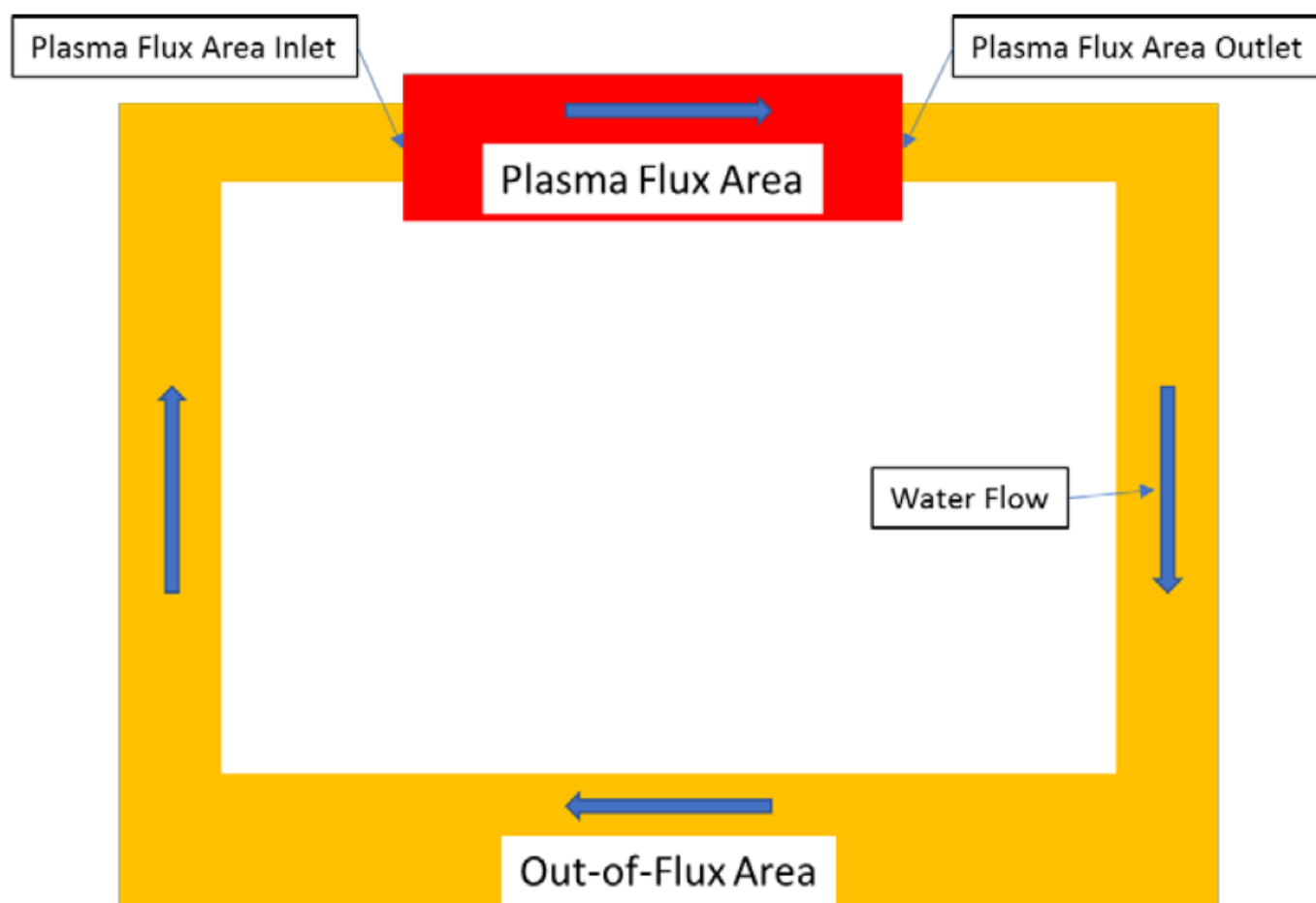


**Figure 44.** Simplified circuit of the IBED-PHTS of the ITER.

The predicted radiolytic species concentrations, the ECP, and the CGR for a standard crack for the OPFA of an Equatorial Port block of the IBED PHTS of the ITER are given in Table 6. Comparison of these tables shows that a large difference exists between the species ( $H_2$ ,  $O_2$ ,  $H_2O_2$ ) in the PFA (Table 5) and the OPFA (Table 6) demonstrating the impact of irradiation in establishing the steady-state concentrations of the principal radiolysis products of water. The ECP also differs substantially between the two regions with values ranging from  $0.439 V_{she}$  to  $0.291 V_{she}$  as  $[H_2]_{Inlet}$  increases from 0 to 10 ppb in the PFA while the ECP in the OPFA decreases from  $0.098 V_{she}$  to  $-0.334 V_{she}$  over the same range of  $[H_2]_{Inlet}$ . Interestingly, in the PFA, the addition of 0.1 cc(STP)/kg $H_2O$  of hydrogen is predicted to lead to a small increase in the ECP (by 0.009 V), which can be traced to a small decrease in  $[H_2]$  and to a small increase in  $[H_2O_2]$  that more than offsets the impact of a decrease in  $[O_2]$ . As expected from the ECP data, a large difference is predicted to exist between the CGRs for a standard crack in the PFA and the OPFA. Because the mechanical, geometric, and metallurgical factors are the same for the cracks in the two regions, the difference is entirely attributable to environmental effects. An important point must be made at this juncture. The electrochemical part of SCC is still present at a CGR level of  $8.8 \times 10^{-13}$  cm/s but, at higher temperatures (e.g., in a BWR at 288 °C, Figure 8), the creep crack growth rate (CCGR) is  $1.6 \times 10^{-10}$  cm/s and it is not possible to observe electrochemical component lower than that value, if the CGR is measured by compliance (change in the crack opening displacement) or any other method that physically measures crack length as a function of time. Thus, the CCGR imposes a lower limit on the crack growth rate that can be observed by conventional methods. However, at 70 °C the CCGR is very low (perhaps  $< 10^{-15}$  cm/s) so that an electrochemical CGR can be monitored down

to this level by measuring the coupling current, noting that the CGR and CC are linearly related by Faraday's law.

**Table 6.** Steady state concentrations of  $H_2$ ,  $O_2$ , and  $H_2O_2$  and the estimated ECP and CGR for a standard crack in sensitized Type 304 SS in the OPFA in the IBED PHTS of the ITER as a function of inlet hydrogen concentration,  $[H_2]_{Inlet}$ .

$[H_2]_{Input}$ cc (STP)/kg $H_2O$	$[H_2]_{Input}$ M	$[H_2]_{Input}$ ppb	$[H_2]_{ss}$ ppb	$[O_2]_{ss}$ ppb	$[H_2O_2]_{ss}$ ppb	ECP $V_{she}$	CGR cm/s
0	0	0	7.5569	70.5978	$6.44 \times 10^{-3}$	0.0981	$1.34 \times 10^{-8}$
0.1	$4.31 \times 10^{-6}$	8.9229	7.6366	$1.17 \times 10^{-6}$	$5.85 \times 10^{-4}$	-0.3244	$8.73 \times 10^{-13}$
0.2	$8.61 \times 10^{-6}$	17.8442	17.2391	$4.41 \times 10^{-7}$	$5.95 \times 10^{-4}$	-0.3241	$8.78 \times 10^{-13}$
0.5	$2.15 \times 10^{-5}$	44.6146	42.7094	$2.71 \times 10^{-7}$	$5.95 \times 10^{-4}$	-0.3241	$8.78 \times 10^{-13}$
1	$4.31 \times 10^{-5}$	89.2292	86.7085	$2.35 \times 10^{-7}$	$5.92 \times 10^{-4}$	-0.3242	$8.77 \times 10^{-13}$
10	$4.37 \times 10^{-4}$	892.2089	879.062	$2.14 \times 10^{-7}$	$5.92 \times 10^{-4}$	-0.3242	$8.77 \times 10^{-13}$

As noted previously in this review, the CGR is strongly correlated with the ECP and the coupling current (CC). The first correlation reflects the theoretical CEFM prediction that CGR is an exponential function of the ECP when the CGR is dominated by the stress corrosion cracking component ( $ECP > E_{crit}$ ) while the second correlation arises from the close relationship between the CGR and CC via Faraday's law. These correlations are displayed in Figures 45 and 46 for the PFA and the OPFA, respectively. In the case of the PFA (Figure 45), all three parameters are predicted to decrease sharply but monotonically with the initial addition of hydrogen  $< 1$  cc(STP)/kg $H_2O$  and then decrease more slowly as the inlet hydrogen is increased to 10 cc(STP)/kg $H_2O$ . Recall that the critical CC for the onset of IGSCC is 1 nA, which is a factor of 4 to 6 orders of magnitude lower than the CCs plotted in Figure 45. Likewise, the critical potential (Table 2) is  $-0.138 V_{she}$ , which is 0.5 to 0.6 V more negative than the ECP in the PFA. This represents a huge overpotential for IGSCC and because of the exponential relationship between CGR and ECP, this difference translates into a very high CGR. In the core of a BWR, for comparison, the overpotential is similar (about 0.5 V), but the lower temperature of the PFA in an Equatorial Port of the ITER (98 °C) compared with that of a BWR (288 °C) implies that the CGR will be about an order of magnitude greater in the former than that in the latter.

In the OPFA (Figure 46), the ECP, CC, and CRG are predicted to decrease sharply upon the addition of 0.2 cc(STP)/kg $H_2O$  and all three parameters become constant at higher  $[H_2]_{Inlet}$ . Thus for  $[H_2]_{Inlet} < 0.2$  cc(STP)/kg $H_2O$ , the ECP and the CC are predicted to be above their respective critical values ( $-0.126 V_{she}$  and 1 nA) so that environmentally assisted cracking (SCC) is expected to occur with a CGR for a standard crack being estimated at about  $10^{-7}$  cm/s. At higher  $[H_2]_{Inlet}$ , the CGR is predicted to lie below  $10^{-10}$  cm/s, which does not pose a threat to the structural integrity of the coolant circuit.

In the current technology, the composition of the cover gas in the IBED-PHTS gives a dissolved hydrogen concentration of 80 ppb [ $0.89$  cc(STP) $H_2$ /kg $H_2O$ ]. This concentration may be compared with 20–50 cc(STP)  $H_2$ /Kg $H_2O$  employed in a PWR primary coolant circuit and to 500 ppb to 2000 ppb [ $5.5$  cc(STP) $H_2$ /kg $H_2O$  to  $22.2$  cc(STP) $H_2$ /kg $H_2O$ ] employed in the primary coolant circuit of a BWR.. A  $[H_2]$  of 80 ppb is estimated to be sufficient to reduce the ECP in the OPFA to a level ( $-0.324 V_{she}$ ) that is sufficient to suppress the CGR below the practical, maximum level of  $10^{-9}$  cm/s (0.315 mm/a) at which SCC is not a problem in a coolant circuit (see Section 5.2) but in the PFA the ECP is predicted to be  $0.3805 V_{she}$ , which gives a calculated standard CGR of  $2.5 \times 10^{-6}$  cm/s. This is more than three orders in magnitude greater than the desired maximum value of  $10^{-9}$  cm/s. We recommend that the HWC issue in ITER be revisited to develop a protocol that is effective in suppressing both the ECP and the CGR in the PFA to levels that permit the operation of the IBED-PHTS in light of the experience gained in fission reactor technology (particularly in BWRs as discussed in Section 5.2).

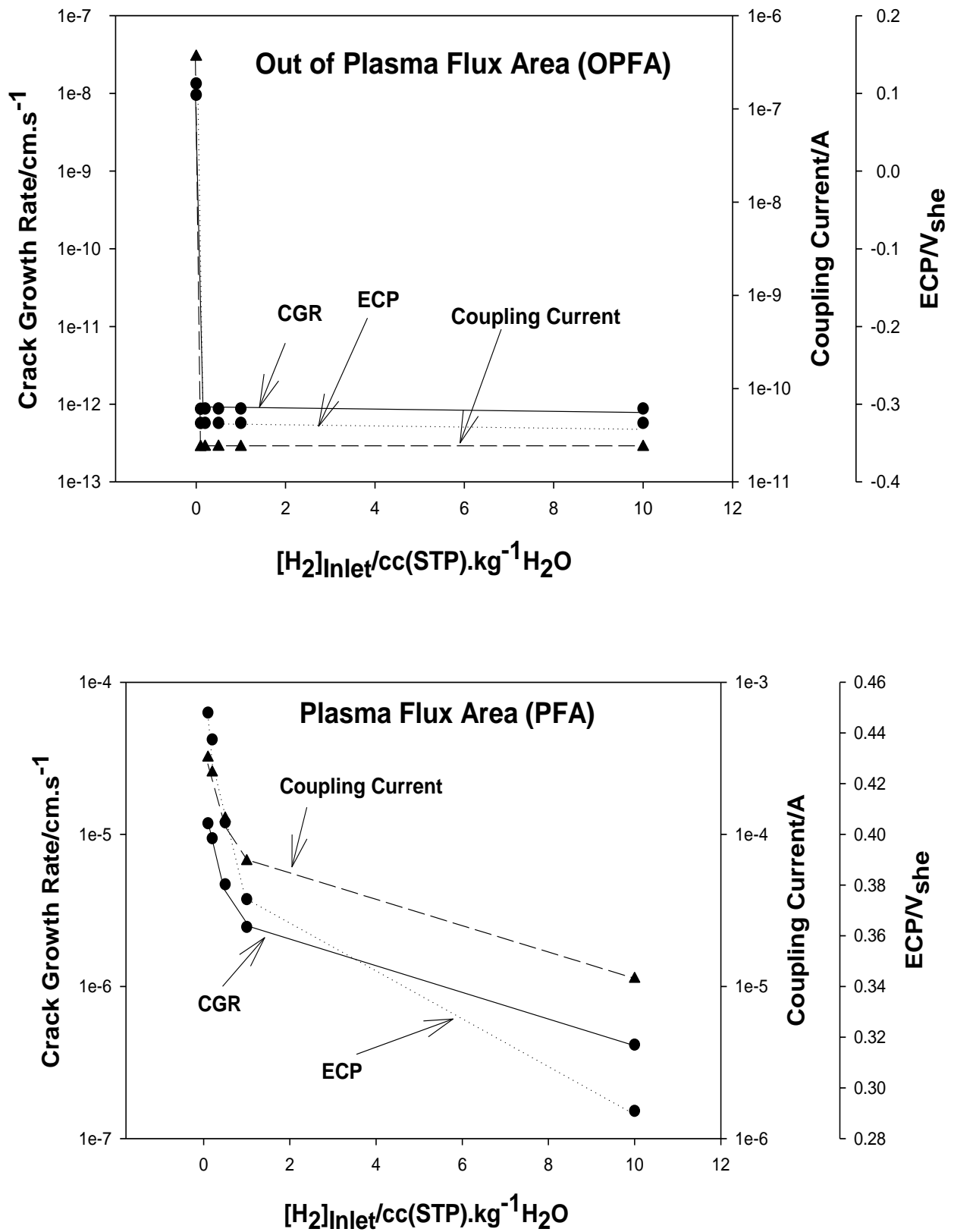


**Figure 45.** Calculated corrosion potential (ECP) and crack growth rate (CGR) and Coupling Current (CC) for a standard IGSCC crack in sensitized Type 304 SS in of an Equatorial Port module in the PFA of the IBED-PHTS of the ITER as a function of the inlet hydrogen concentration,  $[H_2]_{Inlet}$ .  $T = 70\text{ }^\circ\text{C}$ ,  $K_I = 25\text{ MPa.m}^{1/2}$ , crack length = 0.5 cm, flow velocity = 1 m/s, hydrodynamic diameter = 0.5 m,  $[Na^+] = 10\text{ ppb}$ , conductivity at  $98\text{ }^\circ\text{C} = 0.94\mu\text{S/cm}$ . Degree of Sensitization of the steel,  $EPR = 15\text{ C/cm}^2$ .

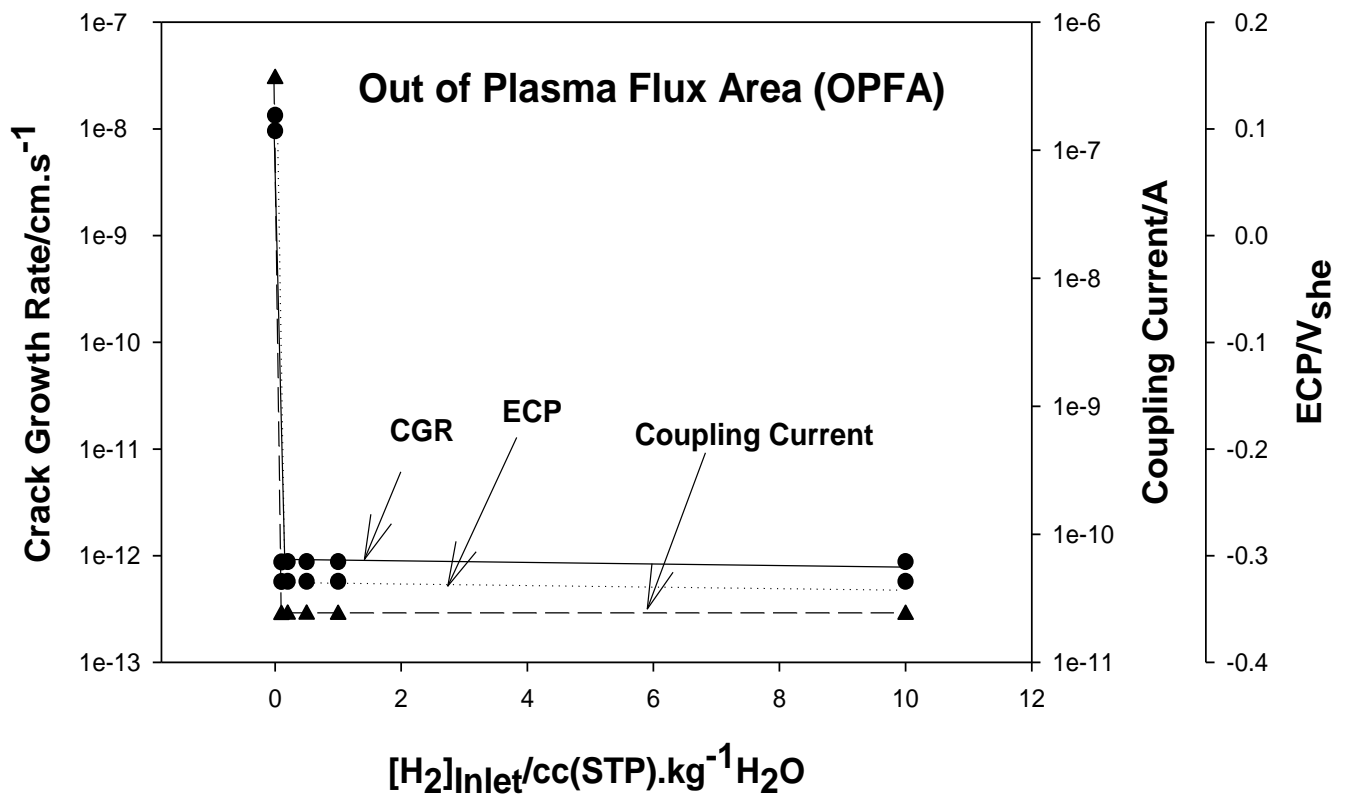


**Figure 46.** Plots of ECP and Coupling current (CC) and crack growth rate (CGR) for IGSCC in stainless steel (Type 304) in the OPFA of an Equatorial Port module of the IBED-PHTS of the ITER as a function of the inlet hydrogen concentration,  $[H_2]_{Inlet}$ .  $T = 70\text{ }^\circ\text{C}$ ,  $K_I = 25\text{ MPa}\cdot\text{m}^{1/2}$ , crack length = 0.5 cm, flow velocity = 1 m/s, hydrodynamic diameter = 0.5 m,  $[Na^+] = 10\text{ ppb}$ , conductivity at  $98\text{ }^\circ\text{C} = 0.94\mu\text{S}/\text{cm}$ . Degree of Sensitization of the steel,  $EPR = 15\text{ C}/\text{cm}^2$ .

At this point, the reader might ask: “Why is this modeling work so important?” It is important for at least two reasons: (1) Much of the circuit is inaccessible to direct experimental interrogation regarding the ECP and hence the accumulation of damage, and (2) Many “what if” scenarios that cannot be explored on operating reactors, because of the safety and economic issues involved, but can be effectively investigated using sophisticated models of the type described in this review. Work to date, in this regard, has emphasized BWRs and PWRs, both fission reactors, because that is where the greatest need has been in assisting plant operators to specify the most cost-effective operating protocols. However, the ITER-related work discussed here demonstrates that electrochemical effects may determine the occurrence of certain damaging phenomena in fusion reactors and hence that this modeling strategy will be effective in that case, too. These issues include:

1. Work carried out using a variant of the model/code (PWR\_ECP) and the scoping calculations reported in [8,68,71] for PWR primary circuits indicates that under certain circumstances the ECP in the steam generators may become sufficiently negative that Alloy 600, a common steam generator tubing material, could suffer HIC (PWSCC). Thus, the work reported in [5] indicates that cracking of Alloy 600 in PWR primary circuits occurs at potentials that are more negative than a critical value of  $-835\text{ mV}_{she}$ . This critical potential is perilously close to the calculated ECP in the steam generators, particularly when using deoxygenated makeup water. The calculations of Bertuch et.al [4] and later by Kim [71] and Kim and Macdonald [68] suggest that the ECP may become more negative than  $-850\text{ mV}_{she}$ , which poses a threat to steam generator integrity. Accordingly, one of the authors (DDM) of this paper has argued for examination of a “low hydrogen” water chemistry [4], which would maintain the ECP at a value that is more positive than the critical value for HIC, but is less positive

than the critical potential for IGSCC in Alloy 600 under all operational conditions. A hydrogen concentration of about 5 cc(STP)/kg(H<sub>2</sub>O) is estimated to be sufficiently low to avoid primary side cracking of steam generator tubes and yet is sufficiently high to “suppress radiolysis” to the extent that it needs to be done [4].

2. Mass transport and the closely related activity transport phenomenon are fundamentally electrochemical in nature. Thus, to a significant extent, the movement of corrosion products around the primary circuits of both BWRs and PWRs is due to differential solubility of magnetite (Fe<sub>3</sub>O<sub>4</sub>), for example, induced by the variation in the ECP, coupled with hydrodynamic factors, as proposed in research reported in [8] and [69], among others. In the authors’ opinion, mass and activity transport phenomena in water-cooled nuclear reactors (WCNRs) can only be understood and predicted by first defining the electrochemistry of the primary heat transport circuits.
3. It is not clear, yet, that activity transport will become an issue in ITER, but the potential for this phenomenon must be recognized in choosing materials for the PHTS. Thus, it is expected that many of the elements in the structural materials in the irradiation zone will be neutron activated. Corrosion will then produce CRUD (Chalk River Unidentified Products) that may deposit on out-of-plasma zone regions of the PHTS, thereby creating  $\gamma$  radiation fields in areas of the reactor that were not designed for the presence of such fields. Together with the contributions from <sup>16</sup>N<sub>7</sub> and <sup>17</sup>N<sub>7</sub>, it is likely that significant man-REM issues will arise during the operation of ITER. Clearly, this issue must be explored, if we are to avoid the same issues that exist in fission reactors. Understanding and controlling the electrochemistry of the coolant circuit is key to managing this problem.

## 8. Summary and Conclusions

The radiolysis of water is a significant cause of various forms of corrosion damage in the primary heat transport systems (PHTSs) of water-cooled nuclear power reactors, including both fission (BWRs and PWRs) and fusion reactors (e.g., the ITER that is currently under development). In Part I of this two-part series, we reviewed the proposed mechanisms for the radiolysis of water and demonstrate that radiolysis leads to the formation of a myriad of oxidizing and reducing species. In this Part II, we review the role that radiolysis plays in the development of corrosion damage in reactor PHTSs. The principal findings are as follows:

- We demonstrate, that the radiolytic generation of oxidizing radiolysis products, such as O<sub>2</sub>, H<sub>2</sub>O<sub>2</sub>, HO<sub>2</sub><sup>-</sup>, and OH in molar excess over reducing species (H<sub>2</sub>, H, and O<sub>2</sub><sup>2-</sup>), some of which (H<sub>2</sub>) are preferentially stripped from the coolant upon boiling in a BWR PHTS, for example, renders the coolant oxidizing, thereby shifting the corrosion potential (ECP) in the positive direction to a value that is more positive than the critical potential ( $E_{crit} = -0.23 V_{she}$  at 288 °C) for Intergranular Stress Corrosion Cracking (IGSCC) in sensitized austenitic stainless steel (e.g., Type 304 SS) and other forms of corrosion (e.g., pitting and corrosion fatigue). This has led to a rash of IGSCC incidents in recirculation piping and internal components in operating BWRs over the past five decades that has exacted a great cost on the operators and electricity consumers, alike.
- In the case of PWRs, the primary circuits are pressurized with hydrogen to give a hydrogen concentration of 20 to 50 cm<sup>3</sup>/kgH<sub>2</sub>O (0.89 to 4.46 ppm), such that no sustained boiling occurs and the hydrogen suppresses the radiolysis of water, thereby inhibiting the formation of oxidizing radiolysis products of water. Thus, the ECP is dominated by the hydrogen electrode reaction (HER), although important deviations from the HER equilibrium potential have been noted. In any event, the ECP is displaced to approximately  $-0.85 V_{she}$ , which is below the critical potential for IGSCC in sensitized stainless steels, but it is more negative than the critical potential for the hydrogen-induced cracking of mill-annealed Alloy 600. This has led to extensive, primary water stress corrosion cracking (PWSCC) of steam generator tubing and other

components (e.g., control rod drive tubes) in PWRs that has also exacted a high cost on operators and power consumers.

- Although the ITER has yet to operate, the proposed chemistry protocol for the coolant places it close to a BWR operating on Normal Water Chemistry (NWC) without boiling or if hydrogen (approx. 80 ppb) is added, close to a BWR on Hydrogen Water Chemistry (HWC).
- In the current technology, the concentration of  $[H_2]$  in the Plasma Flux Area (PFA) and in the Out of Plasma Flux Area (OPFA) is specified as 80 ppb  $[0.89 \text{ cc(STP)}H_2/\text{KgH}_2\text{O}]$ . This level may be compared with 20–50 cc(STP)  $H_2/\text{KgH}_2\text{O}$  employed in a PWR primary coolant circuit and 500 ppb to 2000 ppb  $[5.5 \text{ to } 22.2 \text{ cc(STP)}H_2/\text{KgH}_2\text{O}]$  in a BWR operating on HWC. Hydrogen at the 80ppb level is predicted to reduce the ECP in the OPFA to  $-0.324 V_{\text{she}}$ , which is sufficient to suppress the CGR below the practical, maximum level of  $10^{-9} \text{ cm/s}$  (0.315 mm/a) at which SCC is not a problem in a coolant circuit but, in the PFA, the ECP is predicted to be  $0.380 V_{\text{she}}$ , which gives a calculated standard CGR of  $2.7 \times 10^{-6} \text{ cm/s}$ . This is more than three orders in magnitude greater than the desired maximum value. We recommend that the HWC issue in ITER be revisited to develop a protocol that is effective in suppressing both the ECP and the CGR in the PFA to levels that permit the operation of the IBED-PHTS in light of the experience gained in fission reactor technology.
- The key to managing the development of general and localized corrosion damage in fission and fusion reactor PHTS is exerting close control over the electrochemistry of the system to ensure that the ECP does not lie in a region where damaging corrosion processes occur.

**Funding:** This research received no external funding.

**Data Availability Statement:** Not applicable.

**Acknowledgments:** The authors gratefully acknowledge the support of this work by Andrei Petrov of the Oak Ridge National Laboratory. Andrei Petrov not only provided sterling service in reviewing the manuscript but also provided important background information on the operating conditions of the ITER.

**Conflicts of Interest:** The authors declare no conflict of interest.

## References

1. Macdonald, D.D.; Engelhardt, G.R.; Petrov, A. A Critical Review of Radiolysis Issues in Water-Cooled Fission and Fusion Reactors: Part I, Assessment of Radiolysis Models. *Corros. Mater. Degrad.* **2022**, *3*, 470–535. [[CrossRef](#)]
2. Petrov, A.; Macdonald, D.; Engelhardt, G. Assessment of Radiolysis in Tokamak Cooling Water System of ITER Fusion Reactor. In Proceedings of the 21st International Conference on Water Chemistry in Nuclear Reactor Systems, San Francisco, CA, USA, 9–14 September 2018; EPRI: Palo Alto, CA, USA, 2019; p. 3002016101.
3. Stanbury, M. Reduction Potentials Involving Inorganic Free Radicals in Aqueous Solution. *Adv. Inorg. Chem.* **1989**, *33*, 69–138.
4. Bertuch, A.; Pang, J.; Macdonald, D.D. The Argument for Low Hydrogen and Lithium Operation in PWR Primary Circuits. In Proceedings of the 7th International Symposium on Environmental Degradation of Materials in Nuclear Power Systems—Water Reactors, NACE International, Breckenridge, CO, USA, 6–10 August 1995; pp. 687–697.
5. Totsuka, N.; Szklarska-Smialowska, Z. Effect of Electrode Potential on the Hydrogen-Induced IGSCC of Alloy 600 in an Aqueous Solution at 350 °C. *Corrosion* **1987**, *43*, 734. [[CrossRef](#)]
6. Cragolino, G.; Macdonald, D.D. Intergranular Stress Corrosion Cracking of Austenitic Stainless Steel at Temperatures Below 100 °C—A Review. *Corrosion* **1982**, *38*, 406–424. [[CrossRef](#)]
7. Engelhardt, G.R.; Macdonald, D.D. Unpublished Data. 2021.
8. Macdonald, D.D.; Urquidi-Macdonald, M. The Electrochemistry of Nuclear Reactor Coolant Circuits. In *Encyclopedia of Electrochemistry*; Bard, A.J., Stratmann, M., Eds.; Electrochemical Engineering; Wiley-VCH Verlag GmbH & Co. KGaA: Weinheim, Germany, 2007; Volume 5, pp. 665–720.
9. Indig, M.E.; Nelson, J.L. Electrochemical Measurements and Modeling Predictions in Boiling Water Reactors Under Various Operating Conditions. *Corrosion* **1991**, *47*, 202–209. [[CrossRef](#)]
10. Macdonald, D.D. Viability of Hydrogen Water Chemistry for Protecting In-Vessel Components of Boiling Water Reactors. *Corrosion* **1992**, *48*, 194–205. [[CrossRef](#)]

11. Macdonald, D.D.; Hettiarachchi, S.; Lenhart, S.J. The thermodynamic viability of yttria-stabilized zirconia pH sensors for high temperature aqueous solutions. *J. Solut. Chem.* **1988**, *17*, 719–732. [[CrossRef](#)]
12. Kriksunov, L.B.; Macdonald, D.D.; Millett, P.J. Tungsten/Tungsten Oxide pH Sensing Electrode for High Temperature Aqueous Environments. *J. Electrochem. Soc.* **1994**, *141*, 3002–3005. [[CrossRef](#)]
13. Macdonald, D.D. The Point Defect Model for the Passive State. *J. Electrochem. Soc.* **1992**, *139*, 3434–3449. [[CrossRef](#)]
14. Macdonald, D.D.; Yang, J.; Fekete, B.; Balachov, I.; Spencer, B. *Development and Integration of Light Water Reactor (LWR) Materials Corrosion Degradation Codes into Grizzly*; DOE/NEUP, Award DE-NE0008541(2019); Idaho National Lab. (INL): Idaho Falls, ID, USA, 2019.
15. Lu, P.; Sharifi-Asl, S.; Kursten, B.; Macdonald, D.D. The Irreversibility of the Passive State of Carbon Steel in the Alkaline Concrete Pore Solution under Simulated Anoxic Conditions. *J. Electrochem. Soc.* **2015**, *162*, C572–C581. [[CrossRef](#)]
16. Macdonald, D.D.; Qiu, J. Re-defining the kinetics of redox reactions on passive metal surfaces. *J. Solid State Electrochem.* **2020**, *24*, 2663–2677. [[CrossRef](#)]
17. Bao, J.; Macdonald, D.D. Hydrogen Oxidation on Oxidized Platinum at Elevated Temperatures, Part I: The Tunneling Current. *J. Electroanal. Chem.* **2007**, *600*, 205–216. [[CrossRef](#)]
18. Burns, W.G.; Moore, P.B. Water radiolysis and its effect upon in-reactor zircaloy corrosion. *Radiat. Eff.* **1976**, *30*, 233–242. [[CrossRef](#)]
19. Yeh, T.K.; Macdonald, D.D.; Motta, A.T. Modeling Water Chemistry, Electrochemical Corrosion Potential and Crack Growth Rate in the Boiling Water Reactor Heat Transport Circuits-Part I: The DAMAGE-PREDICTOR Algorithm. *Nucl. Sci. Eng.* **1995**, *121*, 468–482. [[CrossRef](#)]
20. Macdonald, D.D. Unpublished Data (2021).
21. Balachov, I.; Engelhardt, G.R.; Macdonald, D.D. Deterministic Prediction of Damage in Boiling Water Reactors Due to Stress Corrosion Cracking. In *Proceedings of Symposium on Critical Factors in Localized Corrosion*; Electrochemical Society: Pennington, NJ, USA, 1999.
22. Macdonald, D.D.; Balachov, I.; Engelhardt, G. Deterministic Prediction of Localized Corrosion Damage in Power Plant Coolant Circuits. *Power Plant Chem.* **1999**, *1*, 9–16.
23. Lu, P.C.; Macdonald, D.D.; Urquidi-Macdonald, M.; Yeh, T.K. Theoretical Estimation of Crack Growth Rates in Type 304 Stainless Steel in BWR Coolant Environments. *Corrosion* **1996**, *52*, 768–785.
24. Turnbull, A.; Thomas, J.G.N. A model of crack electrochemistry for steels in the active state based on mass transport by diffusion and ion migration. *J. Electrochem. Soc.* **1982**, *129*, 1412. [[CrossRef](#)]
25. Gutman, E.M. An inconsistency in the film rupture model of stress corrosion cracking. *Corros. Sci.* **2007**, *49*, 2289–2303. [[CrossRef](#)]
26. Manahan, M.; Macdonald, D.; Peterson, A. Determination of the fate of the current in the stress corrosion cracking of sensitized type 304SS in high temperature aqueous systems. *Corros. Sci.* **1995**, *37*, 189–208. [[CrossRef](#)]
27. Ford, F.P.; Taylor, D.F.; Andresen, P.; Ballinger, R. *Corrosion-Assisted Cracking of Stainless and Low-Alloy Steels in LWR Environments*; Final Report, EPRI NP-5064M; Electric Power Research Institute: Palo Alto, CA, USA, 1987.
28. Congleton, J.; Shoji, T.; Parkins, R.N. The stress corrosion cracking of reactor pressure vessel steel in high temperature water. *Corros. Sci.* **1985**, *25*, 633. [[CrossRef](#)]
29. Peng, Q.; Kwon, J.; Shoji, T. Development of a fundamental crack tip strain rate equation and its application to quantitative prediction of stress corrosion cracking of stainless steels in high temperature oxygenated water. *J. Nucl. Mater.* **2004**, *324*, 52–61. [[CrossRef](#)]
30. Hall, M. An alternative to the Shoji crack tip strain rate equation. *Corros. Sci.* **2008**, *50*, 2902–2905. [[CrossRef](#)]
31. Gomez-Duran, M.; Macdonald, D.D. Stress corrosion cracking of sensitized Type 304 stainless steel in thiosulfate solution: I. Fate of the coupling current. *Corros. Sci.* **2003**, *45*, 1455–1471. [[CrossRef](#)]
32. Liu, S.; Macdonald, D.D. Fracture of AISI 4340 Steel in Concentrated Sodium Hydroxide Solution. *Corrosion* **2002**, *58*, 835–845. [[CrossRef](#)]
33. Macdonald, D.D. The Electrochemistry of IGSCC Mitigation in BWR Coolant Circuits. *Power Plant Chem.* **2002**, *4*, 329–335.
34. Macdonald, D.D.; Urquidi-Macdonald, M. An Advanced Coupled Environment Fracture Model for Predicting Crack Growth Rates. Chapter 4—Control, Mitigation, and Prediction of Stress Corrosion Cracking. In *Proceedings of the TMS Parkins Symposium on Fundamental Aspects of Stress Corrosion Cracking*, Cincinnati, OH, USA, 20–24 October 1991; pp. 443–455.
35. Macdonald, D.D.; Urquidi-Macdonald, M. A coupled environment model for stress corrosion cracking in sensitized type 304 stainless steel in LWR environments. *Corros. Sci.* **1991**, *32*, 51–81. [[CrossRef](#)]
36. Macdonald, D.D.; Vankeerberghen, M. Predicting Crack Growth Rate vs. Temperature-Behavior of Type 304 Stainless Steel in Dilute Sulfuric Acid Solutions. *Corros. Sci.* **2002**, *44*, 1425–1441.
37. Andresen, P.L. Effects of Temperature on Crack Growth Rate in Sensitized Type 304 Stainless Steel and Alloy 600. *Corrosion* **1993**, *49*, 714–725. [[CrossRef](#)]
38. Lin, L.F.; Cragolino, G.; Szklarska-Smialowska, Z.; Macdonald, D.D. Stress Corrosion Cracking of Sensitized Type 304 Stainless Steel in High Temperature Chloride Solutions. *Corrosion* **1981**, *37*, 616–627. [[CrossRef](#)]
39. Cragolino, G.; Macdonald, D.D.; Park, H.C. Stress Corrosion Cracking of Sensitized Type 304 SS in Borate Solutions at Elevated Temperatures. In *Proceedings of the International Conference on Environmental Degradation of Materials in Nuclear Power System-Water Reactors*, Myrtle Beach, SC, USA, 22–25 August 1983; pp. 604–622.
40. Boiling Water Reactor Systems. Reactor Concepts Manual, USNRC Technical Training Center 3-1 0400 (undated).

41. Zinkle, S.J.; Was, G.S. Materials challenges in nuclear energy. *Acta Mater.* **2013**, *61*, 735–758. [[CrossRef](#)]
42. Kenik, E. Radiation-induced segregation in irradiated Type 304 stainless steels. *J. Nucl. Mater.* **1992**, *187*, 239–246. [[CrossRef](#)]
43. Burns, W.G.; Henshaw, J.; Goodball, J.A.B. *The Radiation Chemistry of a Pressurized Water Reactor. The Effect of Added Hydrogen Based on a Simplified Modeling Approach*; AEA Technology Report AEA RS 3478; AEA Technology, Inc.: Carlsbad, CA, USA, 1994.
44. Burns, W.G.; Sims, H.E. Effect of radiation type in water radiolysis. *J. Chem. Soc. Faraday Trans. 1 Phys. Chem. Condens. Phases* **1981**, *77*, 2803–2813. [[CrossRef](#)]
45. Ruiz, C.P.; Lin, C.C.; Robinson, R.; Burns, W.G.; Curtis, A.R. Model Calculations of Water Radiolysis in BWR Primary Coolant. In Proceedings of the International conference on water chemistry of nuclear reactor systems, Bournemouth, UK, 23–27 October 1989.
46. Yeh, T.K.; Macdonald, D.D.; Motta, A.T. Modeling Water Chemistry, Electrochemical Corrosion Potential, and Crack Growth Rate in the Boiling Water Reactor Heat Transport Circuits-Part III: Effect of Reactor Power Level. *Nucl. Sci. Eng.* **1996**, *123*, 305–316. [[CrossRef](#)]
47. Yeh, T.K.; Macdonald, D.D.; Motta, A.T. Modeling Water Chemistry, Electrochemical Corrosion Potential and Crack Growth Rate in the Boiling Water Reactor Heat Transport Circuits-Part II: Simulation of Operating Reactors. *Nucl. Sci. Eng.* **1996**, *123*, 295–304. [[CrossRef](#)]
48. Yeh, T.K.; Macdonald, D.D. *Predictions of Enhancing Hydrogen Water Chemistry for Boiling Water Reactors by General Catalysis and General Inhibition*; Paper #124; Corrosion/96; NACE International: Houston, TX, USA, 1996; pp. 124/1–124/10.
49. Yeh, T.K.; Macdonald, D.D. *Effects of Power Level Change on the Development of Damage in Boiling Water Reactors under Hydrogen Water Chemistry*; Paper # 126; Corrosion/96; NACE International: Houston, TX, USA, 1996; pp. 126/1–126/12.
50. Macdonald, D.D.; Yeh, T.K. Modeling the Development of Damage in BWR Primary Coolant Circuits. In *Proceedings of the 7th International Conference on Environmental Degradation of Materials in Nuclear Power Systems-Water Reactors*; NACE International: Breckenridge, CO, USA, 1995; pp. 909–919.
51. Ullberg, M.; Gott, K.; Lejon, J.; Granath, G. Advanced ECP model for BWRs. In Proceedings of the International Conference on Environmental Degradation of Materials in Nuclear Power Systems, Whistler, BC, Canada, 19–23 August 2007.
52. Hiroki, A.; LaVerne, J.A. Decomposition of Hydrogen Peroxide at Water–Ceramic Oxide Interfaces. *J. Phys. Chem. B* **2005**, *109*, 3364–3370. [[CrossRef](#)]
53. Lin, C.C.; Smith, F.R.; Ichikawa, N.; Baba, T.; Itow, M. Decomposition of hydrogen peroxide in aqueous solutions at elevated temperatures. *Int. J. Chem. Kinet.* **1991**, *23*, 971–987. [[CrossRef](#)]
54. Hiroishi, D.; Ishigure, K. Poster 12. Homogeneous and heterogeneous decomposition of hydrogen peroxide in high-temperature water. *Proc. Water Chem. Nucl. React. Syst.* **1989**, *5*, 311–312. [[CrossRef](#)]
55. Haines, R.I.; McCracken, D.R. Decomposition of Hydrogen Peroxide under Coolant Chemistry Conditions. *Proc. Water Chem. Nucl. React. Syst.* **1989**, *5*, 309–310.
56. Lin, C.C.; Smith, F.R. *Decomposition of Hydrogen Peroxide at Elevated Temperatures*; Report NP-6733; Electric Power Research Institute: Washington, DC, USA, 1990.
57. Blakeslee, J.A. ZEBRA—A Computer Code for the Steady-State Thermal Analysis of Light Water Cooled Nuclear Power Reactor. Master’s Thesis, Department of Nuclear Engineering, The Pennsylvania State University, State College, PA, USA, 1974.
58. *TRAC-BD1/MOD 1: An Advanced Best Estimate Computer Program for Boiling Water Reactor Transient*; Idaho National Engineering Laboratory: Idaho Falls, ID, USA, 1992.
59. *TRAC-BF1/MOD1: An Advanced Best-Estimate Computer program for BWR Accident Analysis. TRAC-BD1/MOD1 User’s Manuals, Volume 1*; Idaho National Engineering Laboratory: Idaho Falls, ID, USA, 1992.
60. Balachov, I.; Macdonald, D.; Stellwag, B.; Henzel, N.; Kilian, R. Prediction of Materials Damage History From Stress Corrosion Cracking in Boiling Water Reactors. In Proceedings of the Proc. ASME/JSME Joint Press. Vess. Piping Conf., San Diego, CA, USA, 26–30 July 1998; Volume 376, pp. 101–109.
61. Balachov, I.; Macdonald, D.D.; Henzel, N.; Stellwag, B. Modeling and Prediction of Materials Integrity in Boiling Water Reactors. In Proceedings of the Eurocorr ’98, Utrecht, NL, USA, 28 September–1 October 1998.
62. Zhou, X.; Macdonald, D.D.; Balachov, I. Enhancing the Operation of Boiling Water Reactors by Deterministic Simulation. In Proceedings of the Water Chemistry ’98, 1998 JAIF international conference on water chemistry in nuclear power plants, Kashiwazaki, Japan, 13–16 October 1998.
63. Macdonald, D.D.; Balachov, I. Modeling Noble Metal Coatings for Hydrogen Water Chemistry in BWRs. In Proceedings of the 9th International Symposium on Environmental Degradation of Material in Nuclear Power System-Water Reactors, Newport Beach, La Grange, IL, USA, 1–5 August 1999.
64. Zhou, X.-Y.; Balachov, I.I.; Macdonald, D.D. The Effect of Dielectric Coatings on IGSCC in Sensitized Type 304 SS in High Temperature Dilute Sodium Sulfate Solution. *Corros. Sci.* **1998**, *40*, 1349–1362. [[CrossRef](#)]
65. Hettiarachchi, S.; Law, R.J.; Miller, W.D.; Diaz, T.P.; Cowan, R.L. *First application of NobleChem™ to an operating BWRs*; Japan Atomic Industrial Forum, Inc.: Tokyo, Japan, 1998.
66. Cohen, P. *Water Coolant Technology of Power Reactors*; Gordon and Breach Science Publishers, Inc.: New York, NY, USA, 1969.
67. Macdonald, D.; Engelhardt, G. Predictive Modeling of Corrosion. In *Shreir’s Corrosion*; Elsevier: Amsterdam, The Netherlands, 2010; Volume 2, pp. 1630–1679. [[CrossRef](#)]
68. Kim, H.-S.; Macdonald, D.D. PWSCC of Mill-annealed Alloy 600 in PWR Primary Coolant Circuits. 2021. *in preparation*.

69. Macdonald, D.D.; Mahaffy, J.H.; Pitt, J.S.; Urquidi-Macdonald, M. Electrochemical Model of Activity Transport in Pressurized Water Reactors. In Proceedings of the 13th International Conference on Nuclear Engineering, Paper ICONE13-50423, Beijing, China, 16–20 May 2005.
70. Urquidi-Macdonald, M.; Pitt, J.; Macdonald, D.D. The impact of radiolytic yield on the calculated ECP in PWR primary coolant circuits. *J. Nucl. Mater.* **2007**, *362*, 1–13. [[CrossRef](#)]
71. Kim, H.S. A Study for Modeling Electrochemistry in Light Water Reactors. Ph.D. Thesis, Department of Nuclear Engineering, Pennsylvania State University, State College, PA, USA, 2007.
72. Elliot, J.; Bartels, D.M. *The Reaction Set, Rate Constants and g-Values for the Simulation of the Radiolysis of Light Water over the Range 20 to 350 °C Based on Information Available in 2008*; AECL Report, Nuclear Platform Research and Development 153-1 271 60-450-001; Atomic Energy of Canada Limited: Mississauga, ON, Canada, 2009.
73. Garbett, K.; Henshaw, J.; Sims, H.E. Hydrogen and Oxygen Behaviour in PWR Primary Coolant. *Proc. Water Chem. Nucl. React. Syst.* **2000**, *8*, 85–92.
74. Takiguchi, H.; Ullberg, M.; Uchida, A.S. Optimization of Dissolved Hydrogen Concentration for Control of Primary Coolant Radiolysis in Pressurized Water Reactors. *J. Nucl. Sci. Tech.* **2004**, *41*, 601–609. [[CrossRef](#)]
75. Cristensen, H. Remodeling of the Oxidant Species During Radiolysis of High-temperature Water in a Pressurized Water Reactor. *Nucl. Tech.* **1995**, *109*, 373. [[CrossRef](#)]
76. Pastina, B.; Isabey, J.; Hickel, B. The influence of water chemistry on the radiolysis of the primary coolant water in pressurized water reactors. *J. Nucl. Mater.* **1999**, *264*, 309–318. [[CrossRef](#)]
77. Salter-Williams, M. Mass Transport of Magnetite in Pressurized Water Reactor Primary Circuits. Master's Thesis, Department of Nuclear Eng., Pennsylvania State University, State College, PA, USA, 2000.
78. Shi, J.; Fekete, B.; Wang, J.; Macdonald, D.D. Customization of the coupled environment fracture model for predicting stress corrosion cracking in Alloy 600 in PWR environment. *Corros. Sci.* **2018**, *139*, 58–67. [[CrossRef](#)]
79. MacDonald, P.E.; Shah, V.N.; Ward, L.W.; Ellison, P.G. *Steam Generator Tube Failures*; NUREG/CR-6365 (INEL-95/0383); U.S. Nuclear Regulatory Commission: Washington, DC, USA, 1996.
80. Peter, J.; Paine, N.; Ulla, E. Volume 1, The Steam Generator Owners Groups I and II. In *Gustafsson, Editors, Steam Generator Reference Book*; Revision 1; The Steam Generator Reliability Project and Electric Power Research Institute: Palo Alto, CA, USA, 1994.
81. Wikman, S.; Molander, A.; Öjierholm, J.; Eskhult, J.; Törnblom, O. Recent Development and Qualification of Materials for the European Contribution to ITER. ITR/P1-53. In Proceedings of the 23rd IAEA Fusion Energy Conference, Daejeon, Korea, 11–16 October 2010.
82. Saji, G. Scientific Bases of Corrosion Control for Water-Cooled Fusion Reactors Such as ITER. In Proceedings of the 2012 20th International Conference on Nuclear Engineering Collocated with the ASME 2012 Power Conference ICONE20-POWER2012, Anaheim, CA, USA, 30 July–3 August 2012.